CZECH TECHNICAL UNIVERSITY
Faculty Of Mechanical Engineering

Department of Technical Mathematics

Numerical Simulation
of non-Newtonian Fluids Flows
with Applications in Hemodynamics

THESIS

author : Luboš Pirkl

advisor : Mgr. Ing. Tomáš Bodnár PhD.

supervisor : Prof. RNDr. Karel Kozel, DrSc.

Abstract

This work deals with problems of Computational Fluid Dynamics (CFD). This branch is dynamically developing thanks to the strong computer technology, that considerably increased its productivity during past decades. Together with experiment, the CFD analysis is necessary part of many industrial projects all over the world. The work itself deals with numerical simulation of the viscous, incompressible fluid flow. Each fluid may be viewed as a Newtonian fluid or non-Newtonian fluid (Or, more precisely, non-Newtonian liquid. None non-Newtonian behavior has been observed for gases). The work is generally aimed on non-Newtonian fluid flow. Non-Newtonian fluid is a fluid for which the shear stress can't be described by Newton law for fluids. Non-Newtonian fluid is a general term for large group of fluids, for which the stress tensor is described by another relation than Newton law for fluids. Non-Newtonian fluid may be a fluid with variable viscosity, viscoelastic fluid or chemically reacting fluid. All these three non-Newtonian effects are assumed in this work. The introduced models are tested on ten selected test cases. Three test cases deal with validation of the method. Four test cases deal with shear-thinning generalized Newtonian models. Two test cases deal with viscoelasticity. The last test case deals with blood coagulation. All the described methods are general enough. Special emphasis was put on application of methods in hemodynamics.

Souhrn

Tato práce se zabývá počítačovou mechanikou tekutin (CFD). Tato věda se dynamicky vyvíjí díky silné počítačové technice, která prošla obrovským vývojem v posledních desítkách let. Společně s experimentem tvoří CFD analýza nezbytnou součást mnoha projektů v průmyslu po celém světě. Práce samotná se zabývá numerickou simulací proudění vazkých nestlačitelných kapalin. Každá tekutina je newtonská, nebo nenewtonská (nenewtonské jsou pouze kapaliny, nenewtonské vlastnosti plynů dosud nebyly pozorovány). Práce je zaměřená především na proudění nenewtonských tekutin. Nenewtonská tekutina je taková tekutina, pro kterou tensor napětí není popsán Newtonovým zákonem pro tekutiny. Nenewtonská tekutina je pouze obecný výraz pro velkou skupinu tekutin, pro které tensor napětí je vyjádřen pomocí jiného vztahu, než Newtonovým zákonem pro tekutiny. Nenewtonská tekutina může být například tekutina s proměnnou vazkostí, viskoelastická tekutina, nebo chemicky reagující tekutina. Všechny tyto tři zmíněné nenewtonské vlastnosti tekutin jsou dikutovány v této práci. V práci představené modely jsou testovány na deseti vybraných testovacích úlohách. Tři testovací úlohy jsou zaměřeny na validaci metod. Čtyři testovací úlohy jsou zaměřeny na zobecněné newtonské tekutiny. Dvě testovací úlohy jsou zaměřeny na viskoelasticitu. Poslední testovací úloha se zabývá modelováním krevní srážlivosti. Všechny popisované metody mají obecnou platnost. Speciální důraz byl kladen na použití těchto metod pro proudění krve.

Acknowledgements

Here, I would like to thank to Prof. RNDr. Karel Kozel, DrSc. for experienced supervision. Thanks to Karel Tůma and Daniel LaCroix for technical cooperation. Thanks to my wife Klára for a lot of patience.

Special thanks belongs to Mgr. Ing. Tomáš Bodnár PhD. for his brilliant advising me and support during my studies at Czech Technical University.

Contents

List of symbols

Latin symbols

c_f	skin friction coefficient
c_p	specific heat capacity
d	diffusion coefficient
g	gravity force
h	internal energy
$\vec{n}$	surface normal
p	pressure
q	heat flux
s	source term
t	time in general
Δt	time time step
u	velocity components
$\mathbf{u}$	velocity vector
$\mathbf{u}_\tau$	friction velocity
v	velocity components
w	velocity components
x	space coordinates
$\Delta\mathsf{x}$	space step
$\mathbf{x}$	vector of space coordinates
y	space coordinates
z	space coordinates
A	general variable
C	general constant
C	concentration
$\mathfrak{C}$	test case number
D	diameter
D	cell volume
$\mathbf{D}$	rate-of-deformation tensor
De	Deborah number
F	vector of viscous fluxes
G	vector of viscous fluxes
G	spring constant
H	vector of viscous fluxes
L	characteristic length
$\mathbf{L}$	velocity gradient
P_e	Péclet number
R	characteristic radius
R	vector of viscous fluxes
Re	Reynolds number
S	vector of viscous fluxes
T	physical time
T	vector of viscous fluxes
$\mathbf{T}$	stress tensor
U	mean velocity
W	vector of unknowns
$\mathbf{W}$	anti-symmetrical part of velocity gradient
We	Weissenberg number

Greek symbols

$\dot{\gamma}$	shear-rate
τ	shear stress component
μ	dynamic viscosity
$\bar{\mu}$	relative dynamic viscosity
ν	kinematic viscosity
ν_T	turbulent kinematic eddy viscosity
ρ	density
β	artificial compressibility coefficient
κ	heat conductivity
δ	Kronecker delta
ϕ	general vector of unknowns
α	real constant
λ	retardation time
τ	stress tensor component
ϵ	positive constant
ω	weight function
Ω	computational domain
Γ	computational domain boundary

Superscripts

a^n	time level
a'	fluctuation
$\bar{a}$	mean value
$\vec{a}$	vector
a^T	transposition

Subscripts

a_x, a_y, a_z, a_t	partial derivative with respect to axis directions and time
a_w	at the wall
a_∞	asymptotic quantity
a_T	turbulent
a_i, a_j, a_k	reference directions
a_1, a_2, a_3	related to x,y,z-axis direction
a_0	reference value
a_p	related to pressure
a_m	related to momentum equations
a_s	solvent part
a_e	extra stress part

Part I

Introduction

Chapter 1

The Work Motivation

Contents

1.1 Computational Fluid Dynamics

Computational fluid dynamics (CFD) is one of the branches of fluid mechanics that uses numerical methods and algorithms to solve and analyze problems that involve fluid flows. Computers are used to perform calculations required to simulate the interaction of liquids and gases with surfaces defined by boundary conditions.

1.2 Motivation

This work deals with problems of Computational Fluid Dynamics (CFD). This branch is dynamically developing thanks to the strong computer technology, that considerably increased its productivity during past decades. Together with experiment, the CFD analysis is necessary part of many industrial projects all over the world.

The work itself deals with numerical simulation of the incompressible fluid flow. Fluids are classified as Newtonian fluids or non-Newtonian fluids (Or, more precisely, non-Newtonian liquid. None important non-Newtonian behavior has been observed for gases). The work is generally aimed on non-Newtonian fluid flow. Non-Newtonian fluid is a fluid for which the shear stress can't be described by Newton law for fluids. Non-Newtonian fluid is a general term for very large group of fluids, for which the stress tensor is described by another relation than Newton law for fluids. Non-Newtonian fluid may be a fluid with variable viscosity, elastic fluid or chemically reacting fluid. All these three non-Newtonian effects are assumed in this work.

The phenomenon of variable viscosity is in this work represented by a class of shear-thinning Generalized Newtonian fluids[1] (blood, milk, ...). For the Generalized Newtonian fluids the fluid viscosity changes with the shear rate (a norm of velocity gradient).

The phenomenon of fluid viscoelasticity[2] is in this work represented by a group of Johnson-Segalman model (Oldroyd B variant). Viscoelasticity can be observed e.g. in flowing blood, some polymers, etc. For the viscoelastic fluids the fluid stress tensor changes as a function of velocity gradient and other physical properties of the fluid.

---

[1]sometimes called shear-thinning non-Newtonian fluids
[2]fluid is alway viscous and may be also elastic

The phenomenon of blood coagulation is extremely complicated. The blood coagulation model deals with problem, what happens immediately after damaging the blood vessel wall. We introduce the state of art model focused on estimation of growth, rise and lysis of the clot (blood thrombus). The flowing blood model described by Navier-Stokes equations is completed by 28 differential equations for real chemical reactants in human blood. These 28 chemicals represented by their concentrations react each other to form a clot (certain level of fibrin concentration).

All the introduced models can be directly applied in hemodynamics. Hemodynamics[3], meaning literally "blood movement" is the study of blood flow or the circulation. Nevertheless, the work was written with effort to be general enough to keep a wide range of usability of introduced methods. There were selected ten test cases on which is shown the methods' and models' performance. Three test cases are aimed on validation of the method. Four test cases are aimed on testing models for Generalized Newtonian fluids. Two test cases are aimed on testing viscoelastic models. The last test case is aimed on testing blood coagulation model.

In order to keep consistency in the scope of the work, we decided the work to be focused on internal aerodynamics. It means that we have been exploring the flow in various channels and ducts. There was one exception made, that is the flat plate, falling to external aerodynamics. The flat plate test case as one of the most common test cases in CFD. Anyway, from computational point of view, the difference between internal and external aerodynamics is only a question of boundary conditions.

1.3   The State of the Art

In this section we mention the most important works to form this work. Each important chapter of this work has it's own state-of-art section.

The first known attempts to study the blood flow properties were made by *Young* and *Poiseuille* in the seventeen century, who estimated the resistance to blood flow by means of flow experiments in tubes. Although Poiseuille knew that some deviations from others fluids exists, they considered blood to be a Newtonian fluid. Later in twentieth century *Denning & Watson* and *Fahraeus & Lindqvist* [34] observed the anomalous flow property of blood that viscosity appear to depend upon the diameter to the tube used for the measurement.

The development of rotational viscometers in the middle of twentieth century facilitated rigorous experimentations towards the study of the abnormal flow properties of blood. The investigations essentially showed that the blood is shear-thinning generalized Newtonian fluid, see e.g. *Chien* [27], *Dintenfass* [32] and *Caro* [22].

Other research discovered the microstructure of blood can store the mechanical energy (due to the red blood cell properties) and found out the whole blood is viscoelastic fliud, see e.g. *Chien* [28], *Chmiel* [29], *Lowe* [60], Oldroyd [64].

The numerical modeling of blood flow made huge progress together with developing computer power at the end of the twentieth century. At the beginning of computational fluid dynamics the blood was modeled as a Newtonian fluid. Later the shear-thinning variable viscosity models were introduced to imitate the blood flow, see e.g. *Cho & Kensey* [30], *Gijsen* [40], *Berger & Jou* [10], *Leuprecht & Perktold* [58].

More complex blood flow models taking into account both variable viscosity and viscoelasticity were introduced e.g. by *Yeleswarapu* [86] and *Anand & Rajagopal.* [58]

The first attempts to model the blood coagulation process were e.g. [8], [20], [54], [61]. The very complex blood coagulation model was recently introduced by *Anand at al.* [3], reviewed version [15]. The Anand's model was later successfully tested by *Bodnár* [15] in three dimensions. The blood coagulation modeling still remains a big challenge.

The numerical solution of Navier-Stokes equations is well described e.g. in *Kozel & Dvořák* [53], *Bodnár* [15] and *Fürst* [12].

---

[3]following [101]

1.4   Objectives

The main objective of this work is to contribute to CFD modeling in hemodynamics. To do so, the work has following goals:

1. To show the possible way how to solve Navier-Stokes equations using Finite Volume Method

2. To summarize and implement models for viscoelastic and generalized Newtonian fluid flows

3. To implement the state-of-art blood coagulation model

4. To create original solver which can solve viscoelastic and generalized Newtonian fluid flow

5. To compare results with other relevant methods or solvers

6. To investigate the differences and curiosities in Newtonian, generalized Newtonian and viscoelastic type of flow

1.5   The Work Structure

The first part is *Introduction* and gives the general information about this work. The part defines the field o interest, motivation and objectives. The work itself is divided into three main parts:

    I. Mathematical models
        └ Basic System of Balance Laws
        └ Concept of Viscosity of Materials
        └ Viscoelastic Fluid Model
        └ Blood Coagulation Model
    II. Numerical methods
        └ Finite Volume Method
        └ Solvers
    III. Numerical experiments
        └ Validation of Numerical Methods
        └ Tests of Generalized Newtonian Models
        └ Tests of Viscoelastic Models
        └ Application to Blood Coagulation Model

Each part consists of a few chapters. Chapters are divided into sections. The part *Mathematical models* describes the physical background of the problem from mathematical point if view. Starting from basic conservation laws for Newtonian fluid we continue with extending the problem for Generalized Newtonian fluid. Further in this work we introduce models for viscoelastic fluids. Finally, the governing system based on Navier-Stokes equations is modified for viscoelastic Generalized Newtonian fluid. In addition the state of art blood coagulation models is presented.

The part *Numerical methods* introduces numerical method used to solve the equations. The Finite Volume Method which was used in this work and the numerical scheme (MacCormack) are described in detail. The introduced numerical method is steady state using artificial compressibility method, central scheme and structured cell-centered grid.

The part *Numerical experiments* show selected test cases with results from numerical simulations that were performed using described models. All the ten test cases are marked with symbols $\mathfrak{C}_i$. Three test cases are aimed on validation of the method. Four test cases are aimed on testing models for Generalized Newtonian fluid. Two test cases are aimed on testing viscoelastic models. The last test case is aimed on testing blood coagulation model.

Chapter 2

Specific Properties of Blood

Contents

2.1   Blood micostructure

Blood[1] is undeniably the most important bodily fluid. It performs the essential function of providing nutrition and gas exchange for all tissues, maintaining chemical and thermal equilibrium of the body and defending against infection trough the action of antibodies. The blood circulation in the human body depends not only on the driving force of the heart and the mechanical properties of the vascular system, but also on the rheology of blood itself.

Blood is a suspension of large number of formed elements (*cells*) in an aqueous polymer solution (*plasma*). There are three kinds of cells: Red blood cells (RBC) , white blood cells (WBC) and platelets. RBC has biconcave shape with diameter of about $7 \cdot 10^{-6} m$. The blood cells are present in a ratio of approximately 45% cells and 55% plasma.

Plasma contains water (approximately 90-92% by weight), mineral ions such as K^+, Na^-, Cl^-, HCO_3^-, HPO_4^-, (approximately 1-2%) and the reminder (7%) are various proteins. Following figure illustrates bloodstream and the basic members that can be find in it:

---

[1]following [73] and [101]
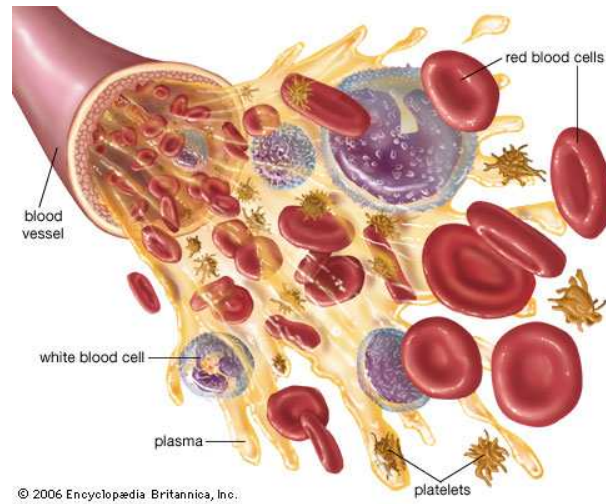
Figure 2.1: The micro-structure of the blood (image reprinted from [104])

2.2   Aggregation and deformability of red blood cells

The red blood cells have a tendency to attach themselves side by side to form what are described as rouleaux, resembling a stack of coins. The phenomena to form rouleaux is called *aggregation*. The attraction is attributed to charged groups on the surface of cells. The process is reversible and also depends on the presence fibrinogen and globulins.

The red blood cells also can *deform* into a infinite variety of shapes without changing volume or surface area as is shown in following figure:
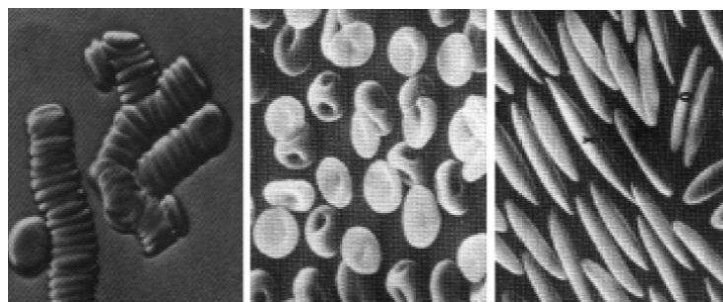
Figure 2.2: Rouleaux, normal cells and deformed cells under microscope (image reprinted from [73])

At high shear rates RBCs exist as an individual particles (like if layers of fluid cut rouleaux) and take a thinner shape. At lower shear rates they aggregate, forming rouleaux resulting in an increase of viscosity. Aggregation and deformability of red blood cells just cause the blood non-Newtonian behavior.
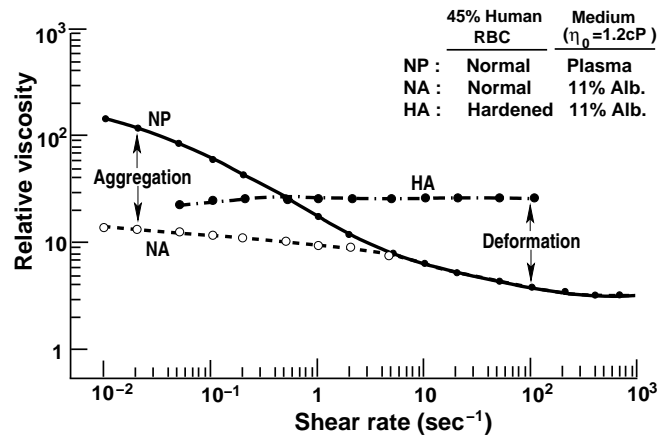
Figure 2.3: Viscosity influenced by aggregation and deformability of red blood cells (image reprinted from [73])

2.3 Blood coagulation

Coagulation[2] is a complex process by which blood forms clots. It is an important part of hemostasis, the cessation of blood loss from a damaged vessel, wherein a damaged blood vessel wall is covered by a platelet and fibrin-containing clot to stop bleeding and begin repair of the damaged vessel. Disorders of coagulation can lead to an increased risk of bleeding (hemorrhage) or obstructive clotting (thrombosis).

Coagulation is highly conserved throughout biology; in all mammals, coagulation involves both a cellular (platelet) and a protein (coagulation factor) component. The system in humans has been the most extensively researched and is therefore the best understood. Figure 2.4 shows an illustration of interaction of chemical reactions.
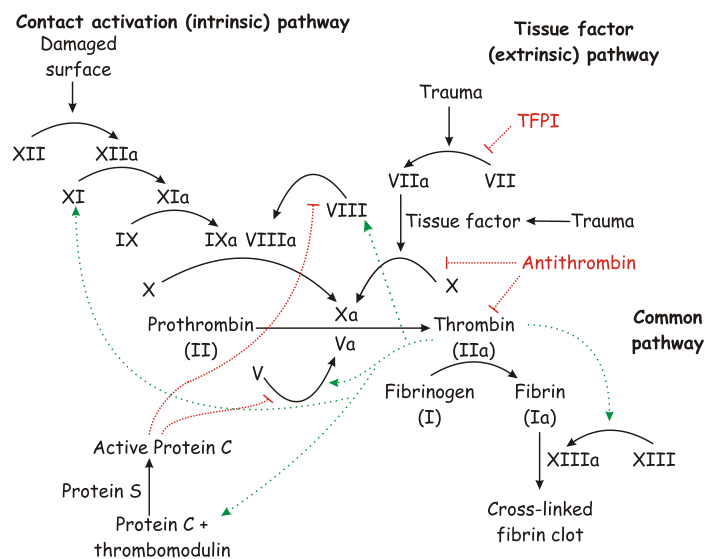
Figure 2.4: Simple illustration of coagulation chemical interactions (image reprinted from [101])

[2]following [106] and [4])

Coagulation begins almost instantly after an injury to the blood vessel has damaged the endothelium lining the vessel. Exposure of the blood to proteins such as tissue factor initiates changes to blood platelets and the plasma protein fibrinogen, a clotting factor. Platelets immediately form a plug at the site of injury; this is called primary hemostasis. Secondary hemostasis occurs simultaneously: Proteins in the blood plasma, called coagulation factors or clotting factors, respond in a complex cascade to form fibrin strands, which strengthen the platelet plug.

A thrombus, sometimes called *blood clot* or simply clot, is the final product of the blood coagulation step in hemostasis. It is achieved via the aggregation of platelets that form a platelet plug, and the activation of the coagulation system (i.e. clotting factors). A clot is normal in cases of injury, but pathologic in instances of thrombosis. In this study we perform a numerical simulation in injured vessel watching the clot growth and clot lysis due to the blood chemical reactions.

(a) Simple illustration of clotting process

(b) Clotting blood under microscope
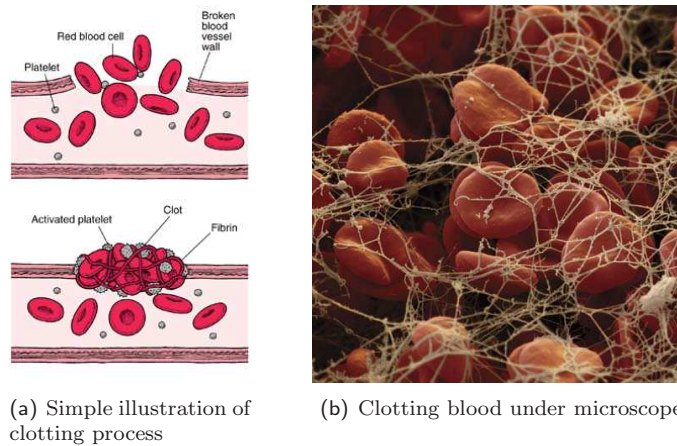
Figure 2.5: Simple illustration of blood clotting process (images reprinted from [107] and [108])

2.3.1 Clot Formation, Growth and & Lysis

In this work the following case is considered: A blood vessel is challenging to a surface injury, exposing the subendothelial layer (which is rich on membrane-bound tissue factor TF) to a quiescent pool of plasma. There are two interacting processes that matter: platelet activation followed by aggregation and tissue-factor-initiated coagulation. This interaction leads to formation, growth and lysis of the clot.

Tissue-factor-initiated blood coagulation process has three stages: initiation, propagation and termination. All these stages are reaction of the system on the vessel injury. The formation, growth and lysis of the clot is governed by boundary conditions, namely the surface concentration TF_VIIa. The clot is the region where fibrin concentration equals or exceeds a specific concentration $C_{critical}^{Ia}$. Fibrinolysis[3] is defined to occur in the regions where fibrin concentration drops below $C_{critical}^{Ia}$ after previously equaling or exceeding it. Many details about blood coagulation process can be found e.g. in [4], [15] or [55].

2.4 Resulting blood flow properties

Particularly, the red blood cells deformability and aggregation determine the blood behavior. Assuming all above mentioned blood properties, the blood flow has following attributes[4]:

- Blood is *shear thinning* fluid, due to the aggregation of red blood cells, these are forming rouleaux structures. At high shear-rates the viscosity goes thin (like if layers of fluid cut the rouleaux structures). At low shear-rates the red blood cells aggregate and the viscosity remains relatively high.

---

[3]or simply clot lysis
[4]following [73], [4], [19].

- Blood is *viscoelastic* fluid due to the deformability of red blood cells. The biconcave shape and the cellular elastic wall make the red blood cell elastic. Therefore the whole blood stream is both viscous and elastic.

- Blood shows *time-dependent* rheology. The blood reaction on outer impulses or inner changes is not immediate. There always exists some delay between action and reaction.

- Blood is also proved to be a *thixotropic* fluid. A thixotropic fluid shows a decrease in viscosity over time at a constant shear rate.

- Blood *coagulates* forming clots with significant influence on local velocity changes, due to the changed geometry and blood viscosity.

Part II

Mathematical Models

Chapter 3

Basic System of Balance Laws

Contents

3.1   Some preliminary ideas & simplifications

The usual way how to describe a fluid flow is by means of the expression for the flow velocity $\mathbf{u}$ at any point $\mathbf{x}$ at any time t:

$$\mathbf{u} = \mathbf{u}(\mathbf{x}, t) \tag{3.1}$$

The velocity field provides the information what all elements of the fluid are "doing" at given time. Finding equation (3.1) is usually the main task. In general the equation (3.1) is convenient shortcut for:

$$\mathbf{u} = (u, v, w)^T, \quad \mathbf{x} = [x, y, z] \tag{3.2}$$

and:

$$u = u(x, y, z, t), \quad v = v(x, y, z, t), \quad w = w(x, y, z, t). \tag{3.3}$$

Generally, we must expect this task to be quite difficult. In this work we assume the following simplifications:

- *Incompressibility* of fluid ($\rho = const$):

$$\operatorname{div} \mathbf{u} = 0, \tag{3.4}$$

  As incompressible fluids are commonly assumed liquids. As incompressible fluids may be also assumed gasses in which the density varies up to 5%, that corresponds to velocities up to ≈ 100 m/s in the atmosphere.

- *Isothermal* flow:
  temperature is considered to be constant in space and time.

- *Volume forces:*
  (Coriolis force, Gravity, ...) are considered to be zero.

- For selected test cases we assume *two-dimensional* (2D) flow:

$$\mathbf{u} = (u(x,y,t), v(x,y,t), 0)^T, \tag{3.5}$$

  in such a case velocity $\mathbf{u}$ is independent on one spatial coordinate (often selected to be z) and has no component in that direction.

- For selected test cases we assume *Steady* flow:

$$\frac{\partial \mathbf{u}}{\partial t} = 0 \tag{3.6}$$

  in such a case $\mathbf{u}$ depends on $\mathbf{x}$ only. At any fixed point in space speed and direction of flow are both constant.

- The fluid flow is assumed to be *laminar* all over this work. Most of applications of introduced models are of Reynolds number ($Re < 200$).

3.2 Balance equations in fluid dynamics

In this section[1] we will take a closer look to basic differential equations of fluid dynamics. The flow of an incompressible viscous fluid is governed by conservation of mass (continuity equation), conservation of momentum (Navier-Stokes equation).

3.3 System of incompressible Navier-Stokes equations

$$\operatorname{div} \mathbf{u} = 0 \tag{3.7}$$

$$\rho \frac{\mathrm{d}\mathbf{u}}{\mathrm{d}t} = \operatorname{div}\mathbf{T} - \nabla p \tag{3.8}$$

where p is pressure, ρ is fluid density[2], $\mathbf{T}$ is fluid shear stress.

The velocity gradient may be rewritten:

$$\mathbf{L} = \nabla \mathbf{u} = \begin{pmatrix} \frac{\partial u_1}{\partial x_1} & \frac{\partial u_1}{\partial x_2} & \frac{\partial u_1}{\partial x_3} \\ \frac{\partial u_2}{\partial x_1} & \frac{\partial u_2}{\partial x_2} & \frac{\partial u_2}{\partial x_3} \\ \frac{\partial u_3}{\partial x_1} & \frac{\partial u_3}{\partial x_2} & \frac{\partial u_3}{\partial x_3} \end{pmatrix} = \begin{pmatrix} u_x & u_y & u_z \\ v_x & v_y & v_z \\ w_x & w_y & w_z \end{pmatrix} = \mathbf{D} + \mathbf{W} \tag{3.9}$$

where $\mathbf{D}$ is rate of deformation tensor (symmetric part of velocity gradient):

---

[1]following e.g. [53], [16]
[2]density is assumed to be a constant all over this work

$$\mathbf{D} = \frac{1}{2}\left(\nabla\mathbf{u} + \nabla\mathbf{u}^T\right) = \frac{1}{2}\begin{pmatrix} 2u_x & u_y + v_x & u_z + w_x \\ v_x + u_y & 2v_y & v_z + w_y \\ w_x + u_z & w_y + v_z & 2w_z \end{pmatrix} \tag{3.10}$$

$\mathbf{W}$ is skew-symmetric part of velocity gradient:

$$\mathbf{W} = \frac{1}{2}\left(\nabla\mathbf{u} - \nabla\mathbf{u}^T\right) = \frac{1}{2}\begin{pmatrix} 0 & u_y - v_x & u_z - w_x \\ v_x - u_y & 0 & v_z - w_y \\ w_x - u_z & w_y - v_z & 0 \end{pmatrix} \tag{3.11}$$

Equations 3.7 can be rewritten for incompressible, viscous, Newtonian fluid:

$$\frac{\partial u}{\partial x} + \frac{\partial v}{\partial y} + \frac{\partial w}{\partial z} = 0 \tag{3.12}$$

$$\rho\left(\frac{\partial u}{\partial t} + u\frac{\partial u}{\partial x} + v\frac{\partial u}{\partial y} + w\frac{\partial u}{\partial z}\right) = -\frac{\partial p}{\partial x} + \frac{\partial}{\partial x}\left(\mu\frac{\partial u}{\partial x}\right) + \frac{\partial}{\partial y}\left(\mu\frac{\partial u}{\partial y}\right) + \frac{\partial}{\partial z}\left(\mu\frac{\partial u}{\partial z}\right) \tag{3.13}$$

$$\rho\left(\frac{\partial v}{\partial t} + u\frac{\partial v}{\partial x} + v\frac{\partial v}{\partial y} + w\frac{\partial v}{\partial z}\right) = -\frac{\partial p}{\partial y} + \frac{\partial}{\partial x}\left(\mu\frac{\partial v}{\partial x}\right) + \frac{\partial}{\partial y}\left(\mu\frac{\partial v}{\partial y}\right) + \frac{\partial}{\partial z}\left(\mu\frac{\partial v}{\partial z}\right) \tag{3.14}$$

$$\rho\left(\frac{\partial w}{\partial t} + u\frac{\partial w}{\partial x} + v\frac{\partial w}{\partial y} + w\frac{\partial w}{\partial z}\right) = -\frac{\partial p}{\partial z} + \frac{\partial}{\partial x}\left(\mu\frac{\partial w}{\partial x}\right) + \frac{\partial}{\partial y}\left(\mu\frac{\partial w}{\partial y}\right) + \frac{\partial}{\partial z}\left(\mu\frac{\partial w}{\partial z}\right) \tag{3.15}$$

3.4 System of Navier-Stokes equations in vector form

Sometimes it is useful to use vector form of equations. Let us rewrite governing equations (3.12) in following form[3]:

$$P\mathbf{W}_t + \mathbf{F}_x + \mathbf{G}_y + \mathbf{H}_z = \mathbf{R}_x + \mathbf{S}_y + \mathbf{T}_z \tag{3.16}$$

where: $\mathbf{W}$ denotes the vector of unknowns, $\mathbf{F},\mathbf{G}$ and $\mathbf{H}$ are the vectors of inviscid (convective) fluxes, $\mathbf{R},\mathbf{S}$ and $\mathbf{T}$ are the vectors of viscous (diffuse) fluxes, P is an additional matrix, that will be discussed.

Before using *artificial compressibility method*[4] let us consider the vectors in the above equation have the following meaning:

$$\begin{aligned} P &= diag(0,1,1) \\ \mathbf{W} &= (p,u,v,w)^T \\ \mathbf{F} &= (u, u^2 + p, uv, uw)^T \\ \mathbf{G} &= (v, vu, v^2 + p, vw)^T \\ \mathbf{H} &= (w, wu, wv, w^2 + p)^T \\ \mathbf{R} &= (0, \mu u_x, \mu v_x, \mu w_x)^T \\ \mathbf{S} &= (0, \mu u_y, \mu v_y, \mu w_y)^T \\ \mathbf{T} &= (0, \mu u_z, \mu v_z, \mu w_z)^T \end{aligned}$$

3.5 System of governing equations in dimensionless form

Lets rewrite the system (3.16) into the following form:

---

[3]subscripts x, y, z, t denotes partial derivatives with respect to time and x, y, z coordinates
[4]see section 7.8

$$P W_t^* + F_x^* + G_y^* + H_z^* = R_x^* + S_y^* + T_z^* \tag{3.17}$$
$$P = diag(0, 1, 1, 1)$$
$$W^* = (p^*, u^*, v^*, w^*)^T$$
$$F^* = (u^*, u^{*2} + p^*, u^*v^*, u^*w^*)^T$$
$$G^* = (v^*, v^*u^*, v^{*2} + p^*, v^*w^*)^T$$
$$H^* = (w^*, w^*u^*, w^*v^*, w^{*2} + p^*)^T$$
$$R^* = (0, \mu u_x^*, \mu v_x^*, \mu w_x^*)^T$$
$$S^* = (0, \mu u_y^*, \mu v_y^*, \mu w_y^*)^T$$
$$T^* = (0, \mu u_z^*, \mu v_z^*, \mu w_z^*)^T$$

where $(^*)$ denotes dimensional values. Equations (3.17) can be transferred to the dimensionless form by following way. Each variable will be divided by its characteristic value of the same dimension.

$$v = \frac{v^*}{v_\infty} \tag{3.18}$$

Typical characteristic values are: velocity of free-stream U_∞ and some characteristic distance,e.g. diameter of channel D_∞. All of the rest variables can be extended with using combination of them:

$$x = \frac{x^*}{D_\infty}, u = \frac{u^*}{U_\infty}, p = \frac{p^*}{U_\infty^2} \tag{3.19}$$

After having used these relations and (3.17), the system of governing equations can be written in dimensionless form. Following equations describe flow of incompressible fluid:

$$P W_t + F_x + G_y + H_z = R_x + S_y + T_z \tag{3.20}$$

where:

$$P = diag(0, 1, 1, 1)$$
$$W = (p, u, v, w)^T$$
$$F = (u, u^2 + p, uv, uw)^T$$
$$G = (v, vu, v^2 + p, vw)^T$$
$$H = (w, wu, wv, w^2 + p)^T$$
$$R = \frac{1}{Re}(0, u_x, v_x, w_x)^T$$
$$S = \frac{1}{Re}(0, u_y, v_y, w_y)^T$$
$$T = \frac{1}{Re}(0, u_z, v_z, w_z)^T$$

where Re is called **Reynolds number**. Reynolds number is very important dimensionless variable, providing information of flow regime of fluid. It is a ratio of inertial and viscous forces. Up to certain (critical) value of Re a flow is laminar while for higher values the flow becomes turbulent. Reynolds number Re is defined:

$$Re = \frac{u_\infty D_\infty}{\nu} = \frac{u_\infty D_\infty \rho}{\mu} \tag{3.21}$$

The flow regime is laminar (the layers of the fluid don't mix together), until the Reynolds number (3.21) reaches its critical value. The governing system (3.20) is ready to solve laminar type of flow. There are not too many real cases of laminar flows. On the other hand, solution of this flow cases provides

valuable information on fluid flow behavior. Laminar cases[5] are for example the flows through tubes or capillaries (Poiseuille flows), or the low speed flow over flat plate, or between two parallel flat plates (Couette flows).

---

[5]only up to critical Reynolds number

Chapter 4

Concept of Viscosity of Materials

Contents

4.1 Rheological constitutive relations

Let us take closer look at some terms, that have to be clarified for better orientation in this work. Here we will describe basic information, specific details will be discussed in following chapters, if needed.

4.1.1 Shear stress (Stress tensor) for Newtonian Fluid

Isaac Newton was the first to express the basic law of rheology describing the flow behavior of an ideal fluid:

$$\mathbf{T} = 2\mu\mathbf{D} \quad [Pa] \tag{4.1}$$

where $\mathbf{T}$ is fluid shear stress, see equation (3.7), μ is dynamic viscosity of fluid and $\mathbf{D}$ is *rate-of-deformation tensor*, see equation (3.10).

4.1.2 Viscosity

Viscosity could be interpreted as a parameter describing the tendency of a fluid to resist to flow as a result of internal friction. There are two commonly used types of viscosity.

Dynamic viscosity

is a material (fluid) property. The typical symbol used to denote dynamic viscosity is μ $[Pa.s] = [kg.m^{-1}.s^{-1}]$.

Kinematic viscosity

is given by:

$$\nu = \frac{\mu}{\rho} \ \ [m^2.s^{-1}] \tag{4.2}$$

Here is an example of same typical materials' dynamic viscosity[1]:

Substance ≈	μ [Pa.s]
Air	$1.0 \cdot 10^{-5}$
Petrol	$6.5 \cdot 10^{-4}$
Water	$1.0 \cdot 10^{-3}$
Mercury	$1.5 \cdot 10^{-3}$
Grape juice	$2.0 \div 5.0 \cdot 10^{-3}$
Blood [at 37^oC]	$4.0 \div 25.0 \cdot 10^{-3}$
Olive oil	$1.0 \cdot 10^{-1}$
Honey	$1.0 \cdot 10^{1}$
Bitumen	$1.0 \cdot 10^{5}$
Glass	$1.0 \cdot 10^{20}$

Viscosity is often considered to be constant, but in general it is function[2] of flow parameters.

$$\mu = \mathcal{F}\left(S, T, \dot{\gamma}, p, t, E\right) \tag{4.3}$$

- S- denotes the *physical-chemical nature* of a substance being the primary influence on viscosity.

- $\dot{\gamma}$- *shear rate* is important factor influencing viscosity of many fluids, the viscosity can either decrease or increase with shear rate, this dependency will be discussed in detail.

- T- is linked to the *temperature* of substance. Experience shows that viscosity is heavily influenced by changes of temperature. In general holds for liquids: the viscosity decreases when temperature increases, and for gases: the viscosity increases when temperature increases.

- p- *pressure* is not experienced as often as previous parameters. Pressure compresses fluids and increases intermolecular resistance. Viscosity can increase.

- t- *time* denotes the phenomenon that the viscosity of some substances, usually dispersions, depends on previous shear history.

- E - parameter *electrical field* is related to a family of suspensions characterized by the phenomenon that their flow behavior is strongly influenced by the magnitude of electrical field acting upon them. These suspensions are called "electro-viscous fluids".

4.2   Non-Newtonian fluids

4.2.1   Basic types of fluids

As already mentioned, viscosity could be interpreted as a tendency of fluid to resist to flow as a result of internal friction. Non-Newtonian fluid is a fluid, which can not be described using Newton's law for fluids (4.1). A typical non-Newtonian fluid is a fluid with variable viscosity. Fluids with variable viscosity are called generalized Newtonian and form a specific subclass of non-Newtonian fluids.

---

[1]Schramm [76]
[2]Schramm [76]

Although the concept of viscosity is commonly used to characterize a material, it can be inadequate to describe the mechanical behavior of a substance, particularly non-Newtonian fluids. Let us take a closer look at the basic types of fluids behavior.
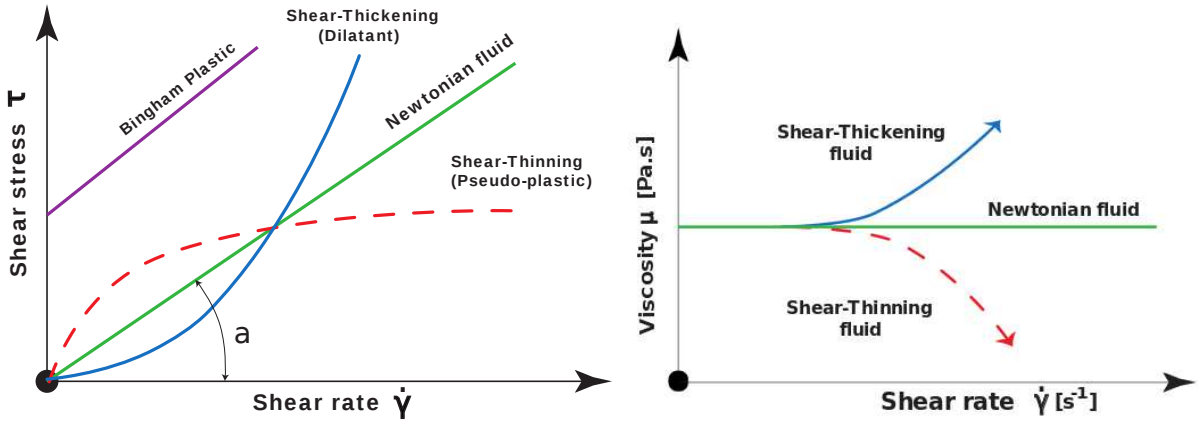
Figure 4.1: Behavior of basic types of fluids

Figure 4.1 shows[3] the behavior of basic types of fluids. For ideal fluid flow, "Newtonian fluid behavior", the graphical equivalent of shear stress is straight line, starting from the origin. The value of the viscosity can also be defined as a slope of shear stress (tangent of the angle a): $\mu = \tan a$. This means, that for Newtonian fluids, μ is not affected by changes in the shear rate.

Bingham plastic fluid shows linear relationship between shear stress and shear rate, if once threshold shear stress is exceeded. As a Bingham plastic fluids are considered for example paste or mud.

For *shear-thickening* (dilatant) fluids the viscosity increases with shear rate. This type of behavior is not so common, As a shear-thickening fluids are considered for example sugar in water or suspension of corn starch.

The most common non-Newtonian fluid behavior in the nature is *shear-thinning* (pseudo-plastic), when the viscosity decreases with shear rate (dashed lines in figure 4.1). As a shear-thinning fluids are considered for example milk or blood.

4.2.2 Shear thinning fluid viscosity

Viscosity of this group of fluids decreases when the shear rate increases. Figure 4.2 shows[4] more details of shear-thinning fluid behavior:

---

[3]e.g. Schramm [76]
[4]Schramm [76]
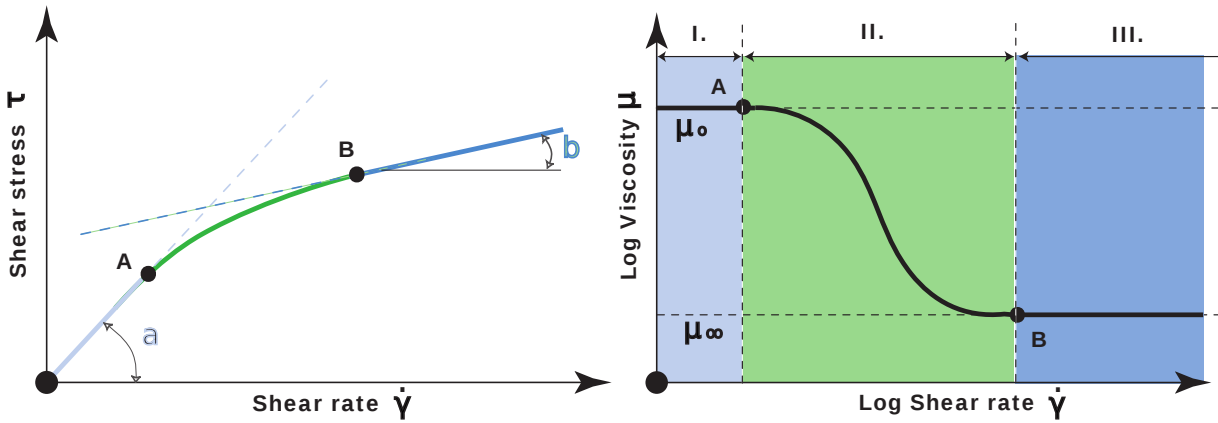
Figure 4.2: Shear-thinning viscosity

For low shear rates ($\mu_0 = \tan a$) and for high shear rates ($\mu_\infty = \tan b$) the fluid shows Newtonian behavior. The problem is to catch the transition of viscosity between the points A and B, where the viscosity decreases from μ_0 to μ_∞. The viscosity drop can be divided into three parts. The first part ($I.$), where the viscosity μ_0 is independent of shear rate and is called *zero shear viscosity* is called *First Newtonian range*. In the second part ($II.$) the viscosity μ drops as a result of fluid micro-structure changes. This part between points A and B has to be approximated. The third part ($III.$), where the viscosity μ_∞ is independent of further increase of shear rate and is called *infinity shear viscosity* is called *Second Newtonian range*.

4.3 Viscosity of Generalized Newtonian fluids

4.3.1 Shear rate

For incompressible Newtonian fluids, the shear stress is proportional to the rate-of-deformation tensor $\mathbf{D}$ (equivalent of Newton's law (4.1)) and can be expressed:

$$\mathbf{T} = 2\mu\mathbf{D} \tag{4.4}$$

where the rate-of-deformation tensor $\mathbf{D}$ is also defined by:

$$\mathbf{D} = \frac{1}{2}\Big(\frac{\partial \mathbf{u}_i}{\partial x_j} + \frac{\partial \mathbf{u}_j}{\partial x_i}\Big) \tag{4.5}$$

and μ[5] is viscosity, which is independent on $\mathbf{D}$. For generalized Newtonian fluids, the shear stress can similarly be written in terms of a generalized Newtonian apparent viscosity μ[6] :

$$\mathbf{T} = 2\mu(\mathbf{D})\mathbf{D} \tag{4.6}$$

In general, μ is a function of all three invariants of the rate of deformation tensor $\mathbf{D}$. But for incompressible fluids, μ is considered to be function of the *shear rate* $\dot\gamma$ only[7]. $\dot\gamma$ is related to the second invariant of $\mathbf{D}$ and is defined as :

$$\dot\gamma = \frac{1}{2}\sqrt{\mathbf{D}:\mathbf{D}} = \frac{1}{2}\sqrt{\sum_{i,j} d_{i,j}^2} \tag{4.7}$$

As a result of the above assumptions apparent viscosity μ is function of shear rate $\dot\gamma$ and shear stress can be expressed:

---

[5]constant
[6]function
[7]e.g. Šesták J. & Rieger F. [77]

$$\mathbf{T} = 2\mu(\dot{\gamma})\mathbf{D} \tag{4.8}$$

4.3.2   Generalized Newtonian viscosity function

Apparent viscosity[8] is computed from simple algebraic model, which is determined by numerical fitting of experimental data. We have tested eight viscosity models, set for human blood. The table 4.1 shows eight generalized Newtonian shear-thinning viscosity models. The model coefficients are calibrated for human blood adopted from *Cho & Kensey* [30].

---

[8]sometimes called effective viscosity

Model name	Model equation	Model coefficients
Modified Cross	$\mu(\dot{\gamma}) = \mu_\infty + (\mu_0 - \mu_\infty)\left[\frac{1}{[1+(\lambda\dot{\gamma})^m]^a}\right]$	μ_0=0.056 Pa.s, μ_∞=0.00345 Pa.s, λ = 3.736 s, m=2.406, a=0.254
Powell-Eyring	$\mu(\dot{\gamma}) = \mu_\infty + (\mu_0 - \mu_\infty)\left[\frac{sinh^{-1}\lambda\dot{\gamma}}{\lambda\dot{\gamma}}\right]$	μ_0=0.056 Pa.s, μ_∞=0.00345 Pa.s, λ=5.383 s
Modified Powell-Eyring	$\mu(\dot{\gamma}) = \mu_\infty + (\mu_0 - \mu_\infty)\left[\frac{ln(\lambda\dot{\gamma}+1)}{[\lambda\dot{\gamma}]^m}\right]$	μ_0=0.056 Pa.s, μ_∞=0.00345 Pa.s, λ = 2.415 s, m=1.089
Cross	$\mu(\dot{\gamma}) = \mu_\infty + (\mu_0 - \mu_\infty)\left[\frac{1}{1+[\lambda\dot{\gamma}]^m}\right]$	μ_0=0.056 Pa.s, μ_∞=0.00345 Pa.s, λ = 1.007 s, m=1.028
Simplified Cross	$\mu(\dot{\gamma}) = \mu_\infty + (\mu_0 - \mu_\infty)\left[\frac{1}{1+\lambda\dot{\gamma}}\right]$	μ_0=0.13 Pa.s, μ_∞=0.005 Pa.s, λ = 8.0 s
Carreau	$\mu(\dot{\gamma}) = \mu_\infty + (\mu_0 - \mu_\infty)\left[1 + (\lambda\dot{\gamma})^2\right]^{\frac{n-1}{2}}$	μ_0=0.056 Pa.s, μ_∞=0.00345 Pa.s, λ = 3.313 s, n=0.3568
Carreau-Yasuda	$\mu(\dot{\gamma}) = \mu_\infty + (\mu_0 - \mu_\infty)\left[1 + (\lambda\dot{\gamma})^a\right]^{\frac{n-1}{a}}$	μ_0=0.056 Pa.s, μ_∞=0.00345 Pa.s, λ =1.902 s, n=0.22,a=1.25
Power-Law	$\mu(\dot{\gamma}) = m\dot{\gamma}^{n-1}$	μ_{min}=0.00345 Pa.s, μ_{max}=0.056 Pa.s, n=0.60,m=0.35

Table 4.1: Generalized Newtonian viscosity models, adopted from *Cho & Kensey* [30].

Chapter 5

Viscoelastic Fluid Model

Contents

5.1   Fluid Viscoelasticity Phenomena

Every real fluid is viscous. Not every fluid is elastic. Viscoelasticity may be viewed as a property of material that shows both viscous and elastic behavior as a reaction on deformation. Viscous materials resist the flow with rate-of-deformation tensor. Elastic materials strain instantaneously when stretched and just as quickly return to their original state once the stress is removed. Viscoelastic materials have elements of both of these properties. Whereas elasticity is usually the result of bond stretching along crystallographic planes in an ordered solid, viscosity is the result of the diffusion of atoms or molecules inside an amorphous material[1]. As viscoelastic fluids are considered for example blood, various polymers and gels.

5.1.1   Stokes Model (Newtonian Fluid)

Viscoelastic models can be interpreted as a set of a dash-pot and a spring. System of 'classical' Navier-Stokes equations (3.7) is using pure viscous Stokes model, which can be interpreted as a single dash-pot (a constant viscosity[2] simply resists the flow, no elasticity is presented).
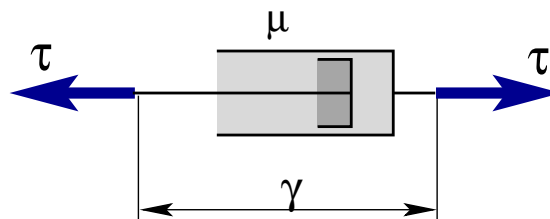
Figure 5.1: Stokes model (image reprinted from [19])

---

[1]following [62]
[2]often called solvent viscosity

Using Stokes model the shear stress can be expressed:

$$\mathbf{T} = 2\mu\mathbf{D} \tag{5.1}$$

5.1.2 Maxwell Model (Viscoelastic Fluid)

The Maxwell model can be represented by a dash-pot and a spring connected in series as shown on following figure:
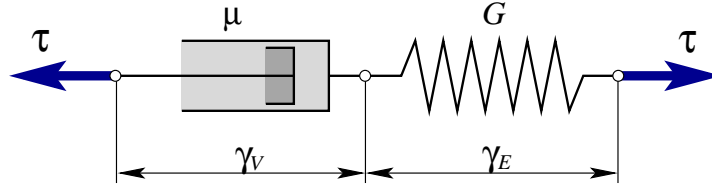
Figure 5.2: Maxwell model (image reprinted from [19])

Using Maxwell model the shear stress can be expressed:

$$\mathbf{T} + \lambda_1 \frac{\delta\mathbf{T}}{\delta t} = 2\mu\mathbf{D} \tag{5.2}$$

where $\frac{\delta\mathbf{T}}{\delta t}$ is *convected derivative*[3] of stress tensor $\mathbf{T}$ and λ_1 is relaxation time.

5.1.3 Oldroyd Type Model (Viscoelastic Fluid)

Oldroyd type model effectively combines the Maxwell model and a Stokes model in parallel. A viscous material is modeled as a spring and a dash-pot in series with each other, both of which are in parallel with a single spring.
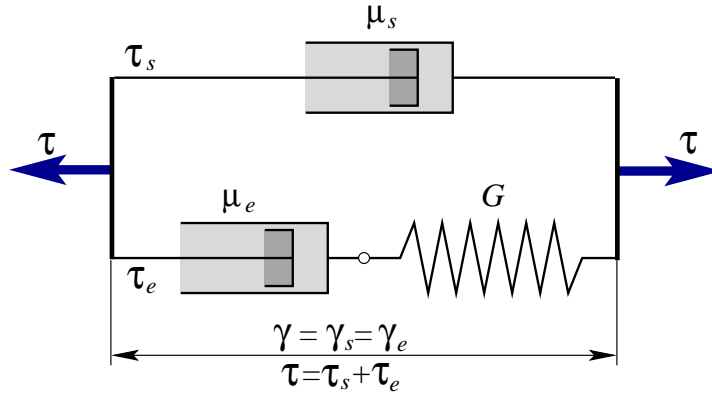
Figure 5.3: Oldroyd model (image reprinted from [19])

Using Oldroyd type model the shear stress can be expressed:

$$\mathbf{T} + \lambda_1 \frac{\delta\mathbf{T}}{\delta t} = 2\mu\left(\mathbf{D} + \lambda_2 \frac{\delta\mathbf{D}}{\delta t}\right) \tag{5.3}$$

where $\frac{\delta\mathbf{T}}{\delta t}$ is convected derivative of stress tensor $\mathbf{T}$, λ_1 is relaxation time and λ_2 is retardation time.

---

[3]see section 5.1.4

5.1.4 Convected derivative

Convected derivative[4] of general tensor **A** may be expressed:[5]

$$\left(\frac{\delta \mathbf{A}}{\delta t}\right)_a = \frac{\partial \mathbf{A}}{\partial t} + \left(\mathbf{u} \cdot \nabla\right)\mathbf{A} - \left(\mathbf{WA} - \mathbf{AW}\right) + a(\mathbf{DA} + \mathbf{AD}) \tag{5.4}$$

where scalar parameter $a = \langle -1, 1 \rangle$. The derivative is sometimes called *Gordon-Schowalter derivative* with parameter $a = \xi - 1$ where ξ called *slip parameter*. The choice of parameter a determines the derivative class.

For choice of $a = 1$ the derivative is called *lower-convected*:

$$\left(\frac{\delta \mathbf{A}}{\delta t}\right)_{a=1} = \overset{\triangle}{\mathbf{A}} = \frac{\partial \mathbf{A}}{\partial t} + \left(\mathbf{u} \cdot \nabla\right)\mathbf{A} - \left(\mathbf{WA} - \mathbf{AW}\right) + (\mathbf{DA} + \mathbf{AD}) \tag{5.5}$$

For choice of $a = -1$ the derivative is called *upper-convected*:

$$\left(\frac{\delta \mathbf{A}}{\delta t}\right)_{a=-1} = \overset{\triangledown}{\mathbf{A}} = \frac{\partial \mathbf{A}}{\partial t} + \left(\mathbf{u} \cdot \nabla\right)\mathbf{A} - \left(\mathbf{WA} - \mathbf{AW}\right) - (\mathbf{DA} + \mathbf{AD}) \tag{5.6}$$

For choice of $a = 0$ the derivative is called *Co-rotational* or *Jaumann*:

$$\left(\frac{\delta \mathbf{A}}{\delta t}\right)_{a=0} = \overset{\circ}{\mathbf{A}} = \frac{\partial \mathbf{A}}{\partial t} + \left(\mathbf{u} \cdot \nabla\right)\mathbf{A} - \left(\mathbf{WA} - \mathbf{AW}\right) \tag{5.7}$$

Notice, the co-rotational model has no physical background because one misses complete information about velocity gradient.

5.2 Viscoelasticity Modeling

The governing system of equations is based on Navier-Stokes equations using Oldroyd type model for stress tensor. Mathematical model is based on incompressible Navier-Stokes equations which are generalized to take into account viscoelasticity and shear-thinning properties of blood flow. The system of equations can be written in the following general form:

$$\text{div } \mathbf{u} = 0 \tag{5.8}$$

$$\rho \frac{d\mathbf{u}}{dt} = \text{div}\mathbf{T} - \nabla p \tag{5.9}$$

$$\mathbf{T} + \lambda_1 \frac{\delta \mathbf{T}}{\delta t} = 2\mu\left(\mathbf{D} + \lambda_2 \frac{\delta \mathbf{D}}{\delta t}\right) \tag{5.10}$$

The stress tensor is generally:

$$\mathbf{T} = \begin{pmatrix} \tau_1 & \tau_2 & \tau_3 \\ \tau_2 & \tau_4 & \tau_5 \\ \tau_3 & \tau_5 & \tau_6 \end{pmatrix} \tag{5.11}$$

where **T** is the stress tensor, **D** is symmetric part of the velocity gradient. It can be shown the parameters λ_1, λ_2 and μ can be rewritten:

$$\lambda_1 = \frac{\mu_e}{G} \tag{5.12}$$

$$\lambda_2 = \lambda_1 \frac{\mu_s}{\mu_s + \mu_e} \tag{5.13}$$

$$\mu = \mu_s + \mu_e \tag{5.14}$$

where G is elasticity modulus, μ_e is extra stress viscosity, μ_s is solvent viscosity.

Stress tensor **T** can be split into two parts:

---

[4]with scalar parameter a

[5]see e.g.[64]

$$\mathbf{T} \quad = \quad \mathbf{T}_s + \mathbf{T}_e \tag{5.15}$$

$$\mathbf{T}_s \quad = \quad 2\mu_s \mathbf{D} \tag{5.16}$$

$$\mathbf{T}_e + \lambda \frac{\delta \mathbf{T}}{\delta t} \quad = \quad 2\mu_e \mathbf{D} \tag{5.17}$$

Where $\mathbf{T}_s$ is solvent part of stress tensor that corresponds to Stokes law for Newtonian fluid. $\mathbf{T}_e$ is viscoelastic (extra stress) part of stress tensor. Both parts can be solved separately. Viscoelastic part of stress tensor $\mathbf{T}_e$ is a symmetric tensor of second order (as well as $\mathbf{T}$ and $\mathbf{T}_s$) therefore six components (in three dimensions) must be computed. Extra stress tensor can be evaluated from the following equation[6]:

$$\frac{\partial \mathbf{T}_e}{\partial t} + (\mathbf{u} \cdot \nabla)\mathbf{T}_e = \frac{2\mu_e}{\lambda}\mathbf{D} - \frac{1}{\lambda}\mathbf{T}_e + (\mathbf{W}\mathbf{T}_e - \mathbf{T}_e\mathbf{W}) - a(\mathbf{D}\mathbf{T}_e + \mathbf{T}_e\mathbf{D}) \tag{5.18}$$

For choice parameter $a = 1$ the model is called _Oldroyd A model_. For choice parameter $a = -1$ the model is called _Oldroyd B model_. For choice parameter $a = 0$ the model is called _Co-rotational model_. More details about extra stress equation can be found e.g. in [7], [72], [64] and [13].

Weissenberg number

An important dimensionless number is Weissenberg number. The Weissenberg number is a dimensionless number used in the study of viscoelastic flows. The dimensionless number is the ratio of the relaxation time of the fluid and a specific process time. For instance, in simple steady shear, the Weissenberg number, is defined as the shear rate times the relaxation time.

$$We = \dot{\gamma}\lambda \tag{5.19}$$

where $\dot{\gamma}$ is shear-rate, λ is relaxation time. Relaxation time may be viewed as a proportion of time, that is required to fluid forgetting the elastic stress (in other words, it is a time of fluid's remembering elastic stress). For flow in pipes Weissenberg number is commonly reduced to:

$$We = \frac{\lambda U}{D} = \frac{\lambda}{\frac{D}{U}} \tag{5.20}$$

where D is characteristic length, typically the channel diameter. U is characteristic velocity.

Deborah number

Another important dimensionless number is Deborah number. The Deborah number is a dimensionless number, often used in rheology to characterize the fluidity of materials under specific flow conditions.

The Deborah number is defined as the ratio of the relaxation time, and the characteristic time scale of an experiment[7], typically the time in which a particle travels from point A to point B.

$$De = \frac{\lambda U}{L} = \frac{\lambda}{\frac{L}{U}} = \frac{\lambda}{T^{char}} \tag{5.21}$$

where L is characteristic length, typically the channel length, U is characteristic velocity and T^{char} is characteristic time.

---

[6]following [13]

[7]an observation time

Chapter 6

Blood Coagulation Model

Contents

6.1 Initial discussion

Physical details about blood properties and rheology are already mentioned in chapter 2. Many details about clot coagulation modeling can be found e.g. in [4], [15] or [55].

The original study of the blood coagulation model was published in [4]. Model was successfully tested on three dimensional model [15]. Later the model was extended to 28 advection reaction-diffusion equations to simulate the biochemical changes and transport of various reactants involved in blood coagulation, see [55]. The formation, growth and lysis of the clot is imitated by boundary conditions, namely the surface concentration TF_VIIa.

In this model the following is considered: A blood vessel is challenging a surface injury, exposing the subendothelial layer (which is rich on membrane-bound tissue factor TF) to a quiescent pool of plasma. There are two interacting processes that matter: platelet activation followed by aggregation and tissue-factor-initiated coagulation. This interaction leads to formation, growth and lysis of the clot.

Tissue-factor-initiated blood coagulation process has three stages: initiation, propagation and termination. All these stages are reaction of the system on the vessel injury. The formation, growth and lysis of the clot is governed by boundary conditions, namely the surface concentration TF_VIIa. The clot is the region where fibrin concentration equals or exceeds a specific concentration $\mathsf{C}^{Ia}_{critical}$. Fibrinolysis[1] is defined to occur in the regions where fibrin concentration drops below $\mathsf{C}^{Ia}_{critical}$ after previously equaling or exceeding it.

6.2 Blood coagulation model description

It is assumed the blood flow is laminar. Whole blood coagulation process is described using system of 28 constituents[2]. The time evolution of all 28 constituents is described by following advection-diffusion equations:

$$\frac{\mathrm{d}\mathsf{C}_i}{\mathrm{d}t} \;\; = \;\; \mathrm{div}\left(\mathsf{d}_i \nabla \mathsf{C}_i\right) + \mathsf{s}_i \qquad i = 1..28 \tag{6.1}$$

Where s_i are source terms specific for all of 28 constituents, d_i are diffusion coefficients.

---

[1]or simply lysis
[2]chemical concentration in moles

6.2.1   Clot formation, growth and lysis

The clot formation, growth and lysis is modeled by a local viscosity changes. The blood viscosity can locally increase due to fibrin production to simulate the clot. The viscosity increase mimics the increase in fibrin concentration.

$$\mu_{local} = \frac{\mathsf{C}_{fibrin}}{\mathsf{C}^0_{fibrin}} \mu \tag{6.2}$$

There is a limiter applied on viscosity growth, the viscosity can increase only to certain saturation level e.g.:

$$\mu_{local} = min(\mu_{local}, 100 \cdot \mu) \tag{6.3}$$

High viscosity at the places with high fibrin concentrations simulates the clot (clot is, where the fibrin concentration is high elevated).

6.2.2   Clotting surface

Clotting surface is an area on the vessel boundary which is being damaged (simulating injury). At the clotting surface non-Homogeneous Neumann boundary conditions for five selected constituents are used:

$$\frac{\partial IXa}{\partial x} = -\frac{k_{7,9} \cdot IX \cdot TF\_VIIa}{K_{7,9M} + IX} \frac{L}{D_{IXa}} \tag{6.4}$$

$$\frac{\partial IX}{\partial x} = \frac{k_{7,9} \cdot IX \cdot TF\_VIIa}{K_{7,9M} + IX} \frac{L}{D_{IX}} \tag{6.5}$$

$$\frac{\partial Xa}{\partial x} = -\frac{k_{7,10} \cdot X \cdot TF\_VIIa}{K_{7,9M} + X} \frac{L}{D_{Xa}} \tag{6.6}$$

$$\frac{\partial X}{\partial x} = \frac{k_{7,9} \cdot X \cdot TF\_VIIa}{K_{7,9M} + X} \frac{L}{D_X} \tag{6.7}$$

$$\frac{\partial tPA}{\partial x} = -(k_{CtPA} + k_{IIatPA} \cdot e^{-134.8 \cdot (t-T_0)} \cdot IIa + k_{IatPA} \cdot Ia) \cdot ENDO \cdot \frac{L}{D_{tPA}} \tag{6.8}$$

where L is characteristic length, surface concentration $ENDO = 2.0 \cdot 10^9 \ cells/m^2$, Time evolution of the surface concentration TF_VIIa is based on an experimental data approximation, see [4]. Concentration TF_VIIa is modeled using following formula:

$$TF\_VIIa = (k_{TF7a} \cdot 10^{-15}) \cdot (93.93 \cdot e^{(-((t-465.8)/123.4)^2)} + 58.66 \cdot e^{(-((t-765.5)/352.2)^2)}) \tag{6.9}$$

Figure 6.1 shows time evolution of the surface concentration TF_VIIa. Table 13.3 in Appendix B shows reaction terms for all 28 advection-diffusion equations. Table 13.2 shows diffusion terms and initial values for all 28 advection-diffusion equations. Tables 13.4 and 13.1 show model parameters. The expression $SIunit$ displays the dimension of the term[3], e.g. [1 -3 0 0 0 0 0] corresponds to $kg \cdot m^{-3}$.

---

[3][kg m s K mol A cd]
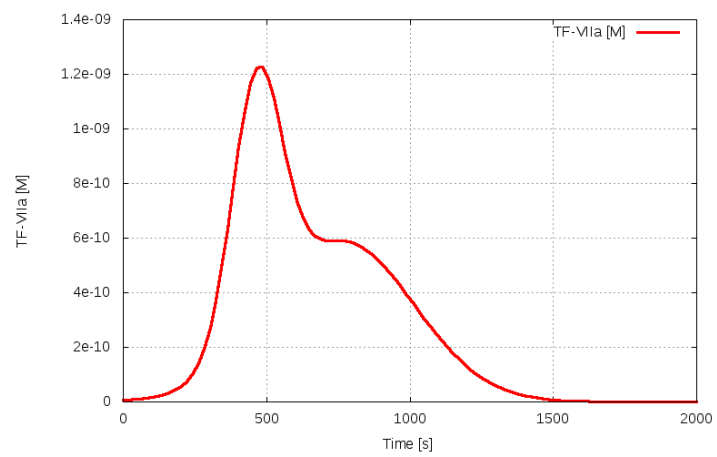
Figure 6.1: Surface concentration of TF_VIIa

Part III

Numerical Methods

Chapter 7

Finite Volume Method

Contents

7.1 Finite volume method

Finite volume method[1] (FVM) is developed for cases of general (nonorthogonal) meshes. Let us consider the closed area Ω with finite number of disjoint cells $D_{i,j}$. Figure 7.1 shows two most common types of meshes for FVM in two dimensions. The first one is made of triangles and the second one is made of quadrilaterals. The advantage of the first one (so-called: unstructured triangular mesh) is that it is easier to generate for complex types of geometry. On the other hand the structured mesh consisting of quadrilateral cells allows very efficient storage of data in fields and it is possible to easily extend 1D schemes to multiple dimensions.

7.2 Finite volume discretization

One can rewrite the equation (3.20) into the following vector form[2]:

$$W_t + (F - R)_x + (G - S)_y + (H - T)_z = 0 \tag{7.1}$$

After the space integration we get:

---

[1]following Fořt et al. [38]
[2]Bodnár [12]

(a) Unstructured mesh   (b) Structured mesh
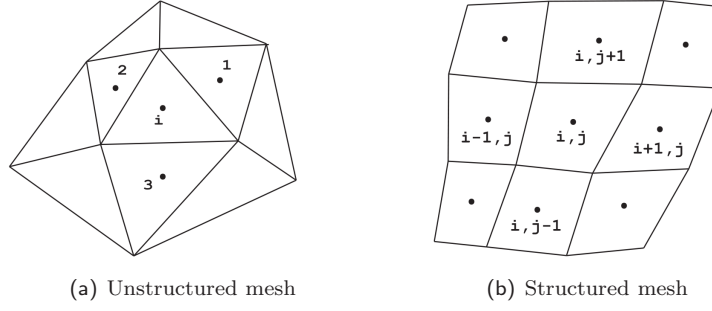
Figure 7.1: Basic types of meshes (two dimensional)

$$\int_{\mathsf{D}_{i,j}} \mathsf{W}_t dV + \int_{\mathsf{D}_{i,j}} \Big[(\mathsf{F} - \mathsf{R})_x + (\mathsf{G} - \mathsf{S})_y + (\mathsf{H} - \mathsf{T})_z \Big] dV = 0 \tag{7.2}$$

Applying Gauss's theorem ($\int_V \nabla \cdot A \, dV = \oint_{\partial V} A\vec{n} \, dS$) one obtain:

$$\int_{\mathsf{D}_{i,j}} \mathsf{W}_t dV + \oint_{\partial \mathsf{D}} \Big[(\mathsf{F} - \mathsf{R})\vec{n}^x + (\mathsf{G} - \mathsf{S})\vec{n}^y + (\mathsf{H} - \mathsf{T})\vec{n}^z \Big] dS = 0 \tag{7.3}$$

Now one can substitute, $\mathsf{W}_{i,j} = \frac{1}{|\mathsf{D}|} \int_{\mathsf{D}} \mathsf{W} dS$, the cell average of W over the cell $\mathsf{D}_{i,j}$ and the system becomes system ordinary differential equations for each cell ($\mathsf{D}_{i,j}$) average:

$$\frac{\partial \mathsf{W}_{i,j}}{\partial t} + \frac{1}{|\mathsf{D}|} \oint_{\partial \mathsf{D}} \Big[(\mathsf{F} - \mathsf{R})\vec{n}^x + (\mathsf{G} - \mathsf{S})\vec{n}^y + (\mathsf{H} - \mathsf{T})\vec{n}^z \Big] dS = 0 \tag{7.4}$$

7.3   Lax-Wendroff scheme

The numerical scheme (*MacCormack scheme*), which is used in this project, is a member of family of central schemes and is based on Lax-Wendroff scheme. Lax-Wendroff scheme follows the idea of Taylor expansions of the "new value" in time and substituting time derivatives by space derivatives[3].

Consider scalar advection equation:

$$\mathsf{W}_t + A\mathsf{W}_x = 0 \tag{7.5}$$

where A is the advection velocity.

The unknown variable W is computed in discrete points $\mathsf{W}(x_i, t_n) = \mathsf{W}_i^{n+1}$, where $x_i = x_0 + i\Delta x$ and $t_n = t_0 + n\Delta t$. We are looking for solution W_i^{n+1}:

$$\mathsf{W}_i^{n+1} = \mathsf{W}(x_i, t_{n+1}) = \mathsf{W}(x_i, t_n + \Delta t) \tag{7.6}$$

Taylor expansions up to the second order at point $\mathsf{W}(x_i, t_n)$ is:

$$\mathsf{W}_i^{n+1} = \mathsf{W}_i^n + \mathsf{W}_t \Delta t + \mathsf{W}_{tt} \Delta t^2 + \mathcal{O}(\Delta t^3) \tag{7.7}$$

now, we replace time derivatives using 7.5:

$$\mathsf{W}_t = -A\mathsf{W}_x, \tag{7.8}$$
$$\mathsf{W}_{tt} = -A\mathsf{W}_{xt}, \tag{7.9}$$
$$\mathsf{W}_{tx} = -A\mathsf{W}_{xx}, \tag{7.10}$$
$$\mathsf{W}_{tx} = \mathsf{W}_{xt}, \tag{7.11}$$
$$\mathsf{W}_{tt} = A^2\mathsf{W}_{xx} \tag{7.12}$$

---

[3]e.g. LeVeque [59]

then:

$$\mathsf{W}_i^{n+1} = \mathsf{W}_i^n - A\mathsf{W}_x \Delta t + A^2 \mathsf{W}_{xx} \Delta t^2 \tag{7.13}$$

now, we discretize the space derivatives using central difference approximation:

$$\mathsf{W}_i^{n+1} = \mathsf{W}_i^n - \frac{A\Delta t}{2\Delta x}(\mathsf{W}_{i+1}^n - \mathsf{W}_{i-1}^n) + \frac{A^2 \Delta t^2}{2\Delta x^2}(\mathsf{W}_{i+1}^n - 2\mathsf{W}_i^n + \mathsf{W}_{i-1}^n) \tag{7.14}$$

It is possible to show that Lax-Wendroff scheme is of second order accuracy:

$$\frac{T}{\Delta t} \mathcal{O}(\Delta t^3) \approx \mathcal{O}(\Delta t^2) \tag{7.15}$$

7.3.1   Modified equation for Lax-Wendroff scheme

All second-order three-point central schemes of the Lax-Wendroff family generate oscillations around sharp discontinuities[4]. Let us take a closer look at this problem. We start with constructing *modified equation* for Lax-Wendroff scheme. It can be find by substituting terms of Lax-Wendroff scheme (7.14) by its' Taylor expansions at $\mathsf{W}(x_i, t_n)$.

The third-order Taylor expansions of individual terms of Lax-Wendroff scheme (7.14) are:

$$\mathsf{W}_i^{n+1} = \mathsf{W}(x_i, t_{n+1}) = \mathsf{W}(x_i, t_n) + \Delta t \mathsf{W}_t(x_i, t_n) + \frac{\Delta t^2}{2}\mathsf{W}_{tt}(x_i, t_n) + \frac{\Delta t^3}{6}\mathsf{W}_{ttt}(x_i, t_n) + \mathcal{O}(\Delta t^4)$$

$$\mathsf{W}_{i+1}^n = \mathsf{W}(x_{i+1}, t_n) = \mathsf{W}(x_i, t_n) + \Delta x \mathsf{W}_x(x_i, t_n) + \frac{\Delta x^2}{2}\mathsf{W}_{xx}(x_i, t_n) + \frac{\Delta x^3}{6}\mathsf{W}_{xxx}(x_i, t_n) + \mathcal{O}(\Delta x^4)$$

$$\mathsf{W}_{i-1}^n = \mathsf{W}(x_{i-1}, t_n) = \mathsf{W}(x_i, t_n) - \Delta x \mathsf{W}_x(x_i, t_n) + \frac{\Delta x^2}{2}\mathsf{W}_{xx}(x_i, t_n) - \frac{\Delta x^3}{6}\mathsf{W}_{xxx}(x_i, t_n) + \mathcal{O}(\Delta x^4)$$

Now, we substitute these relations into the Lax-Wendroff scheme (7.14):

$$\mathsf{W}(x_i, t_n) + \Delta t \mathsf{W}_t(x_i, t_n) + \frac{\Delta t^2}{2}\mathsf{W}_{tt}(x_i, t_n) + \frac{\Delta t^3}{6}\mathsf{W}_{ttt}(x_i, t_n) =$$
$$\mathsf{W}(x_i, t_n) - \frac{A\Delta t}{2\Delta x}\Big(2\Delta x \mathsf{W}_x(x_i, t_n) + \frac{\Delta x^3}{3}\mathsf{W}_{xxx}(x_i, t_n)\Big)$$
$$+ \frac{A^2 \Delta t^2}{2\Delta x^2}\Big(\Delta x^2 \mathsf{W}_{xx}(x_i, t_n)\Big) + \mathcal{O}(\Delta t^4, \Delta x^4) \tag{7.16}$$

that simplifies in:

$$\mathsf{W}_t(x_i, t_n) + A\mathsf{W}_x(x_i, t_n) =$$
$$-\frac{\Delta t}{2}\mathsf{W}_{tt}(x_i, t_n) - \frac{\Delta t^2}{6}\mathsf{W}_{ttt}(x_i, t_n) - \frac{A\Delta x^2}{6}\mathsf{W}_{xxx}(x_i, t_n)$$
$$+ \frac{A^2 \Delta t}{2}\mathsf{W}_{xx}(x_i, t_n) + \mathcal{O}(\Delta t^3, \Delta x^3) \tag{7.17}$$

Using the same ideas as in section (7.3) we can continue:

$$\mathsf{W}_t(x_i, t_n) + A\mathsf{W}_x(x_i, t_n) =$$
$$-\frac{\Delta t^2}{6}\mathsf{W}_{ttt}(x_i, t_n) - \frac{A\Delta x^2}{6}\mathsf{W}_{xxx}(x_i, t_n) + \mathcal{O}(\Delta t^3, \Delta x^3) =$$
$$\frac{A^3 \Delta t^2}{6}\mathsf{W}_{xxx}(x_i, t_n) - \frac{A\Delta x^2}{6}\mathsf{W}_{xxx}(x_i, t_n) + \mathcal{O}(\Delta x^3) =$$
$$-\frac{\Delta x^2}{6}\Big(A - \frac{\Delta t^2}{\Delta x^2}A^3\Big)\mathsf{W}_{xxx}(x_i, t_n) + \mathcal{O}(\Delta x^3) \tag{7.18}$$

---

[4]see e.g. Hirsh [41]

modified equation for Lax-Wendroff scheme:

$$W_t + AW_x = -\frac{\Delta x^2}{6}\left(A - \frac{\Delta t^2}{\Delta x^2}A^3\right)W_{xxx} \tag{7.19}$$

One can see that modified equation of Lax-Wendroff scheme does not contain the numerical viscosity of the second order. The term on the right hand side has dispersive character[5]. Hence, it is necessary to damp non-physical oscillations. One method to do so is using *additional artificial viscosity* (denoted by DW). The additional artificial viscosity can be constructed in following way (Lax-Wendroff scheme):

$$W_i^{n+1} = W_i^n - \frac{A\Delta t}{2\Delta x}(W_{i+1} - W_{i-1}) + \frac{A^2\Delta t^2}{2\Delta x^2}(W_{i+1} - 2W_i + W_{i-1}) + \underbrace{\Delta x^2\epsilon(\Delta x^a)(W_{i+1} - 2W_i + W_{i-1})}_{DW \,=\, \text{additional artificial viscosity term}}$$

$$\tag{7.20}$$

where $\epsilon > 0$ is coefficient of additional artificial viscosity.

Modified equation is then:

$$W_t + AW_x = \Delta x^2\epsilon(\Delta x^a)W_{xx} - \frac{\Delta x^2}{6}\left(A - \frac{\Delta t^2}{\Delta x^2}A^3\right)W_{xxx} \tag{7.21}$$

Now, the modified equation contains the term with second derivative, that damps oscillations and helps to preserve the stability of the method.

7.4   MacCormack scheme

MacCormack scheme is a two-step scheme. This is a formulation of Lax-Wendroff scheme in the form *predictor-corrector*. Both schemes become identical in case of linear problem solution. It is an iteration method, that works in three steps. The predictor step (7.22) is computed at first. These "new values" from predictor step are used in the corrector step (7.23). In the third step additional artificial viscosity (artificial dissipation) is added. The next iteration follows, until the solution is sufficiently converged.

Inviscid and viscous fluxes are evaluated[6] in a different way, according to sections 7.4.1 and 7.4.2 and figures 7.3 and 7.4.
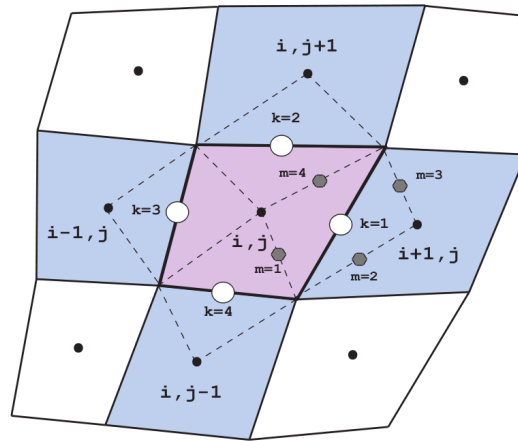
Figure 7.2: Computational stencil for Finite Volume Method

---

[5]see e.g. [38]
[6]following Bodnár [12]

Predictor

$$W_{i,j}^{n+\frac{1}{2}} = W_{i,j}^n - \frac{\Delta t}{|D_{i,j}|} \sum_{k=1}^{4} \{(F_k^n - R_k^n)\vec{n}^x + (G_k^n - S_k^n)\vec{n}^y + (H_k^n - T_k^n)\vec{n}^z\} \tag{7.22}$$

Corrector (+ Predictor)

$$\left(W_{i,j}^{n+1}\right) = \frac{1}{2}\left(W_{i,j}^n + W_{i,j}^{n+\frac{1}{2}} - \frac{\Delta t}{|D_{i,j}|} \sum_{k=1}^{4}\{(F_k^{n+\frac{1}{2}} - R_k^{n+\frac{1}{2}})\vec{n}^x + (G_k^{n+\frac{1}{2}} - S_k^{n+\frac{1}{2}})\vec{n}^y + (H_k^{n+\frac{1}{2}} - T_k^{n+\frac{1}{2}})\vec{n}^z\}\right) \tag{7.23}$$

Corrector (+ Predictor) + Artificial viscosity

$$W_{i,j}^{n+1} = \left(W_{i,j}^{n+1}\right) + DW_{i,j}^n \tag{7.24}$$

7.4.1 Discretization of inviscid fluxes

Predictor $F_1 = F_2 = F_{i,j}, F_3 = F_{i-1,j}, F_4 = F_{i,j-1}$

- also applies to G and H.

Corrector $F_1 = F_{i+1,j}, F_2 = F_{i,j+1}, F_3 = F_4 = F_{i,j}$

- also applies to G and H.

(a) Predictor - backward step   (b) Corrector - forward step

(c) Predictor + Corrector

Figure 7.3: Computational Stencil for inviscid fluxes computation

7.4.2 Discretization of viscous fluxes

Derivatives for viscous fluxes can be obtained by integration over dual cell boundary equation (7.25), figure 7.4. Integral is replaced by discrete sum over dual cell faces:

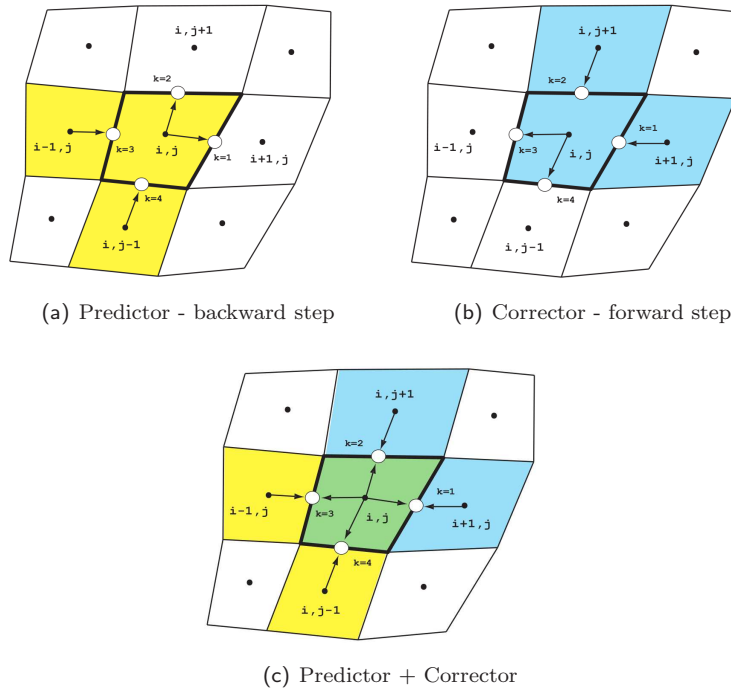$$\mathsf{W}_x \approx \frac{1}{\mathsf{D}_k} \oint_{\partial \mathsf{D}} \mathsf{W}\ \vec{n}^x dx dy \approx \frac{1}{\mathsf{D}_k} \sum_{m=1}^{4} u_m n_m^x l_m \tag{7.25}$$

where: W is unknown variable in the center of the m-th face, n_m^x is outer normal of the face in point m, l_m is length of the m-th face, D_k is volume of a dual cell. Values of variables in the middle of dual faces are computed as an average of values of its neighbor cells. The member $\mathsf{DW}_{i,j}^n$ is artificial viscosity and is added to corrector in order to damp numerical oscillations. We will discuss details in section (7.5).
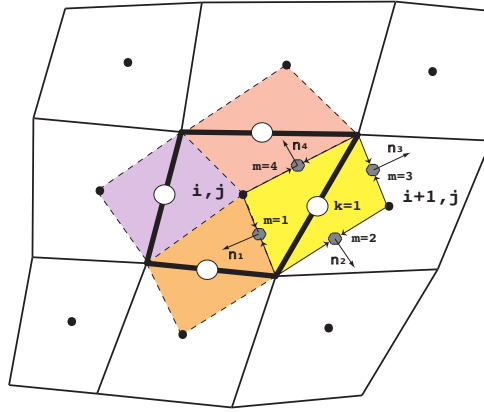
Figure 7.4: Computational stencil for viscous fluxes computation (dual cells)

7.5 Artificial viscosity

We have used two different types of artificial viscosity. The first one is Von Neumann - Richtmayer (Von Neumann & Richtmayer, 1950) artificial viscosity, that is traditional and well tested artificial viscosity. The second one is artificial viscosity with TVD property[7]. Using this artificial viscosity the whole scheme is often referred as the TVD MacCormack scheme.

7.5.1 Von Neumann - Richtmayer artificial viscosity

It was used in form[8] (1D case for simplicity):

$$\mathsf{DW}_i^n = \epsilon_2 \Delta x^3 \frac{d}{dx} |\mathsf{W}_x| \mathsf{W}_x \Big|_i^n + \epsilon_4 \Delta x^4 \mathsf{W}_{xxxx} \Big|_i^n \tag{7.26}$$

After replacing derivatives we obtain:

$$\mathsf{DW}_i^n = \epsilon_2 \big[|\mathsf{W}_{i+1}^n - \mathsf{W}_i^n| (\mathsf{W}_{i+1}^n - \mathsf{W}_i^n) - |\mathsf{W}_i^n - \mathsf{W}_{i-1}^n| (\mathsf{W}_i^n - \mathsf{W}_{i-1}^n) \big] + \epsilon_4 (\mathsf{W}_{i-2}^n - 4\mathsf{W}_{i-1}^n + 6\mathsf{W}_i^n - 4\mathsf{W}_{i+1}^n + \mathsf{W}_{i+2}^n) \tag{7.27}$$

where $\epsilon_2, \epsilon_4 \in \mathbb{R}$ are constants, that have to be carefully chosen.

---

[7]e.g. Fürst [36]
[8]Hirsh [41]

7.5.2   Modified Causon's TVD MacCormack scheme

We mention 1D case[9], for simplicity. Two dimensional artificial viscosity is analogical and the second direction varies in indices only:

$$\text{DW}_i^n = \left[\bar{G}^+(\bar{r}_i^+) + \bar{G}^-(\bar{r}_{i+1}^-)\right]\left(\text{W}_{i+1}^n - \text{W}_i^n\right) - \left[\bar{G}^+(\bar{r}_{i-1}^+) + \bar{G}^-(\bar{r}_i^-)\right]\left(\text{W}_i^n - \text{W}_{i-1}^n\right) \tag{7.28}$$

where:

$$\bar{r}_i^+ = \frac{< \text{W}_i^n - \text{W}_{i-1}^n, \text{W}_{i+1}^n - \text{W}_i^n >}{< \text{W}_{i+1}^n - \text{W}_i^n, \text{W}_{i+1}^n - \text{W}_i^n >} \tag{7.29}$$

$$\bar{r}_i^- = \frac{< \text{W}_i^n - \text{W}_{i-1}^n, \text{W}_{i+1}^n - \text{W}_i^n >}{< \text{W}_i^n - \text{W}_{i-1}^n, \text{W}_i^n - \text{W}_{i-1}^n >} \tag{7.30}$$

Here $< \cdot, \cdot >$ denotes the standard inner scalar product.

$$\bar{G}^+(\bar{r}_i^+) = \frac{1}{2}C(\bar{\nu}_i)[1 - \Phi(\bar{r}^+)] \tag{7.31}$$

$$\bar{G}^+(\bar{r}_i^-) = \frac{1}{2}C(\bar{\nu}_i)[1 - \Phi(\bar{r}^-)] \tag{7.32}$$

$$\Phi(\bar{r}^\pm) = \max(0, \min(2\bar{r}^\pm, 1)) \tag{7.33}$$

$$C(\bar{\nu}_i) = \begin{cases} \bar{\nu}_i(1 - \bar{\nu}_i) & \text{for } \bar{\nu}_i \leq 0.5 \\ 0.25 & \text{for } \bar{\nu}_i > 0.5 \end{cases} \tag{7.34}$$

$$\bar{\nu}_i = \Psi(a_i)\frac{\Delta t}{\Delta x} \tag{7.35}$$

$$a_i = \min \begin{cases} un_x + vn_y \\ un_x + vn_y + \sqrt{u^2n_x^2 + 2un_xvn_y + v^2n_y^2 + n_x^2 + n_y^2} \\ un_x + vn_y - \sqrt{u^2n_x^2 + 2un_xvn_y + v^2n_y^2 + n_x^2 + n_y^2} \end{cases} \tag{7.36}$$

$$\Psi(a_i) = \begin{cases} |a_i| & \text{for } |a_i| > \epsilon_e \\ \frac{a_i^2 + \epsilon_e^2}{2\epsilon_e} & \text{for } |a_i| \leq \epsilon_e \end{cases} \tag{7.37}$$

where a_i is minimal absolute value of eigenvalues of the Jacobi matrix A_i at the point W_i. $\Psi(a_i)$ is called entropy correction with $\epsilon_e = 10^{-3}$

7.6   Time step restrictions

To keep stability of the method, it is important to use correct time step for the method. Time step is usually computed for each iteration. For cartesian 3D mesh time step can be computed from the following relation:

$$\Delta t = \min\frac{CFL}{\frac{\rho_a}{\Delta x} + \frac{\rho_b}{\Delta y} + \frac{\rho_c}{\Delta z} + \left(\frac{1}{Re}\right)\left(\frac{1}{\Delta x^2} + \frac{1}{\Delta y^2} + \frac{1}{\Delta z^2}\right)} \tag{7.38}$$

where Re is Reynolds number, $CFL \leq 1$ is called $Courant - Friedrichs - Lewy$ number, ρ_a , ρ_b and ρ_c are spectral radii of Jacobian of inviscid fluxes F, G and H:

$$\rho_a = |u| + \sqrt{u^2 + \beta^2}, \quad \rho_b = |v| + \sqrt{v^2 + \beta^2}, \quad \rho_c = |w| + \sqrt{w^2 + \beta^2} \tag{7.39}$$

---

[9]e.g. Fürst [36]

In most cases especially for steady state simulations it is useful to use *Local Time Stepping* method. It is acceleration method, based on the idea that different time step is used for each cell separately ($\Delta t \to \Delta t_{i,j}$). As a result, each cell has its own iteration time, but it does not harm the final solution, because of its steady character. This technique can shorten iteration time even to one half. But one should keep on mind taking risk of some possibility of lost of consistency leading to breaking up stability.

7.7 Monitoring of convergence

For monitoring of convergence of unknowns we have used[10] global $L_2 - norm$ of steady residual. Consider $Rez \sim \|Rez(W)\|_{L_2}$ which in ideal case should come close to zero.

$$Rez = \sqrt{\sum_{i,j} \frac{1}{M \cdot N} \Big(\frac{\mathsf{W}_{i,j}^{n+1} - \mathsf{W}_{i,j}^{n}}{\Delta t} \Big)^2} \tag{7.40}$$

7.8 Artificial Compressibility Method

To compute incompressible, steady flow, it is necessary to solve the problem with absence of pressure in vector of unknowns $P\mathsf{W}$ in continuity equation. Artificial compressibility method[11] is elegant method fixing this problem. We can add time derivative of pressure to the continuity equation, which vanishes, when the solution converges to the steady solution:

$$\frac{1}{\beta^2} \frac{\partial p}{\partial \tau} + \frac{\partial u}{\partial x} + \frac{\partial v}{\partial y} + \frac{\partial w}{\partial z} = 0 \tag{7.41}$$

where β is artificial compressibility coefficient and represents local speed of sound of transformed system. The system (3.20) changes into:

$$\tilde{P}\mathsf{W}_t + \mathsf{F}_x + \mathsf{G}_y + \mathsf{H}_z = \mathsf{R}_x + \mathsf{S}_y + \mathsf{T}_z \tag{7.42}$$

where the only difference is:

$$\tilde{P} = \begin{pmatrix} \frac{1}{\beta^2} & 0 & 0 \\ 0 & 1 & 0 \\ 0 & 0 & 1 \end{pmatrix}$$

We choose $\beta = 1$, then $\tilde{P} = I = diag(1, 1, 1)$ and our system of governing equations is independent on additional matrix $\tilde{P}$.

---

[10]e.g. Kozel & Dvořák [53]
[11]e.g. Bodnár [12]

Chapter 8

Solvers

For testing of the above described methods there were used two different solvers. The *in-house code* and the *open-source code*. For test cases $\mathfrak{C}_1$ - $\mathfrak{C}_8$ (described later) was used the in-house code. For test cases $\mathfrak{C}_9$ and $\mathfrak{C}_{10}$ was used the open-source code. Both codes are based on Finite Volume Method.

In test cases $\mathfrak{C}_3$ and $\mathfrak{C}_9$ we also compare results of our Finite Volume solvers with another solver based on Finite Element Method. The Finite Element solver was developed by another group at Charles University in Prague. The numerical simulations using this FEM code were performed by Karel Tůma. The details of Finite Element solver are described in Appendix A.

8.1 In-house code

The name of our in-house code is krysa+. Author of this work is also author of the code/solver krysa+. The code is written in programming language C/C++. The code uses most of the methods described on previous pages. krysa+ solver is not very efficient code and can not be used for real three-dimensional applications. For this reason all the models were implemented also to OpenFOAM, an open-source CFD Toolbox.

krysa+ solver main features:

- Finite Volume Method
- Steady state solver
- Artificial compressibility method
- Three dimensional (3D)
- Structured grid
- Cell centered grid
- Explicit method

- Central scheme, second order
- MacCormack scheme, artificial viscosity (von Neumann, TVD MacCormack)
- Newtonian, shear-thinning and viscoelasticity models
- Local time stepping
- OpenMP

Such a in-house code has strong and weak sides. Strong sides are obvious. For example the author has an absolute freedom in the way of implementation of methods and organizing code structure etc. Another big benefit can be easy code adaptivity to some special problem. As a last but not least benefit we can mention an exclusive experience that author gains writing his own code. Many authors confirm the full understanding of the problem comes after its implementation in some code.

Of course, there are also weak sides of in-house codes. There is seldom good documentation of in-house codes, which make troubles in involving other people to the project. Team development may often be a problem. Another problem may be a robustness (importing and exporting various data, switching models, ...). In-house codes have often problem with a performance, especially in parallel computing.

8.2   Open-source code

The code is based on freely available code OpenFOAM that is written in programming language C++. The name of the solver is krysaFOAM, which is modified solver *pisoFoam* under *OpenFOAM*[1], an open-source CFD Toolbox. Solver pisoFoam uses the *PISO* algorithm to solve incompressible Navier-Stokes equations for newtonian fliud. The PISO (Pressure Implicit with Splitting of Operators) algorithm is an efficient method to solve incompressible Navier-Stokes equations in unsteady problems. We have implemented all the described models into solver pisoFoam. The new solver krysaFOAM can solve generalized Newtonian flow, viscoelastic flow and coagulating blood flow.

krysaFOAM solver main features:

- Finite Volume Method

- Unsteady solver

- PISO algorithm

- Three dimensional (3D)

- Unstructured grid

- Cell centered grid

- Implicit method

- Central scheme, second order, Upwind scheme

- Segregated linear system solver

- method: PBiCG
  Preconditioned Bi-Conjugate Gradient

- preconditioner: DILU
  Diagonal Incomplete LU

- Newtonian, generalized Newtonian, viscoelasticity and blood coagulation model

- MPI

OpenFOAM has many strong sides. The code is distributed under GPL (General Public License). The code is open, which means the source code is available to anyone and can be copied and modified by any user. The code is stable and has wide community of contributors. Nowadays, not only many universities use OpenFOAM, it is being used by many industrial companies. OpenFOAM has also a good parallel efficiency, it is commonly used for computations on many processors (128 cores, or even more). OpenFOAM documentation and many details of the code can be found e.g.: [65], [66], [105].

---

[1]www.openfoam.com

Part IV

Numerical Experiments

Chapter 9

Validation of Numerical Methods

Contents

9.1 $\mathfrak{C}_1$: Flow in Gap Between Two Plates

9.1.1   The aim of the test case

The aim of this test case is to compare the results of methods introduced in chapter 7 with analytical solution. This validation test case aimed on internal aerodynamics, with low Reynolds number. We will find an analytical solution of velocity distribution in the gap between two endless plates (figure 9.1), Poiseuille flow. The analytically computed velocity distribution will be compared to the developed velocity profile obtained from numerical simulation. This test case is simplified to two dimensions. Figure 9.1 shows a general sketch of a gap between two plates.

We assume Navier-Stokes equations for incompressible, viscous, Newtonian fluid:

$$\frac{\partial u}{\partial x} + \frac{\partial v}{\partial y} + \frac{\partial w}{\partial z} = 0 \tag{9.1}$$

$$\rho\Big(\frac{\partial u}{\partial t} + u\frac{\partial u}{\partial x} + v\frac{\partial u}{\partial y} + w\frac{\partial u}{\partial z}\Big) = -\frac{\partial p}{\partial x} + \mu\Big(\frac{\partial^2 u}{\partial x^2} + \frac{\partial^2 u}{\partial y^2} + \frac{\partial^2 u}{\partial z^2}\Big) \tag{9.2}$$

$$\rho\Big(\frac{\partial v}{\partial t} + u\frac{\partial v}{\partial x} + v\frac{\partial v}{\partial y} + w\frac{\partial v}{\partial z}\Big) = -\frac{\partial p}{\partial y} + \mu\Big(\frac{\partial^2 v}{\partial x^2} + \frac{\partial^2 v}{\partial y^2} + \frac{\partial^2 v}{\partial z^2}\Big) \tag{9.3}$$

$$\rho\Big(\frac{\partial w}{\partial t} + u\frac{\partial w}{\partial x} + v\frac{\partial w}{\partial y} + w\frac{\partial w}{\partial z}\Big) = -\frac{\partial p}{\partial z} + \mu\Big(\frac{\partial^2 w}{\partial x^2} + \frac{\partial^2 w}{\partial y^2} + \frac{\partial^2 w}{\partial z^2}\Big) \tag{9.4}$$
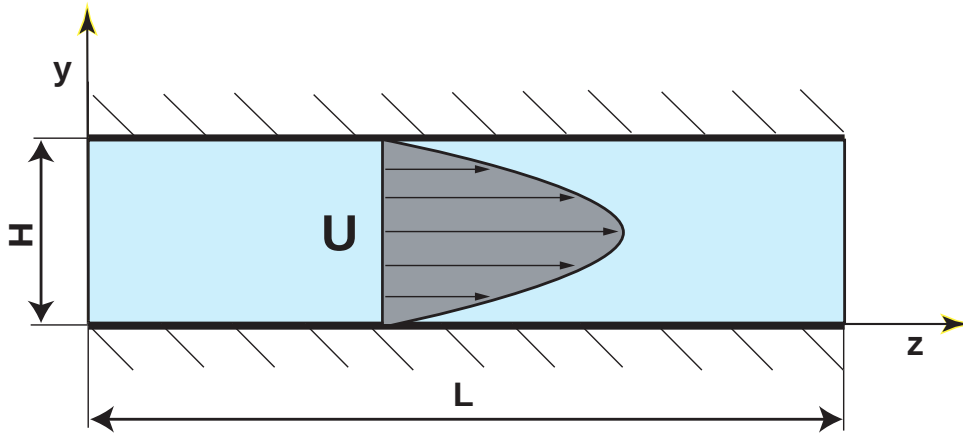
Figure 9.1: Velocity profile in the gap between two plates

We assume the fluid to flow in direction z , $(u = v = 0)$. Continuity equation (9.1) is then:

$$\frac{\partial w}{\partial z} = 0 \tag{9.5}$$

Momentum equations(9.2),(9.3) and (9.4) become:

$$\rho w \frac{\partial w}{\partial z} = -\frac{\partial p}{\partial z} + \mu \Big(\frac{\partial^2 w}{\partial x^2} + \frac{\partial^2 w}{\partial y^2} + \frac{\partial^2 w}{\partial z^2}\Big) \tag{9.6}$$

We know, the term $\partial w/\partial x$ is zero for this case of endless plates. Using equation (9.5), the equation (9.6) can be simplified:

$$\mu \frac{\partial^2 w}{\partial y^2} = \frac{\partial p}{\partial z} \tag{9.7}$$

where the pressure gradient can be substituted by the ratio of pressure difference Δp and distance L:

$$\frac{\partial^2 w}{\partial y^2} = \frac{1}{\mu} \frac{\Delta p}{L} \tag{9.8}$$

To get the velocity profile w, we integrate equation 9.8:

$$w = \frac{1}{\mu} \frac{\Delta p}{L} \frac{y^2}{2} + C_1 y + C_2 \tag{9.9}$$

Now we can add boundary conditions to get the integration constants:

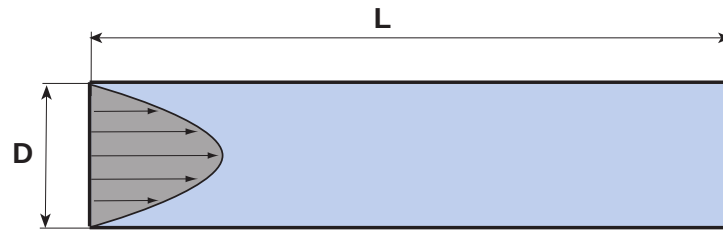$$w = 0, \quad \textbf{for} \quad y = 0 \tag{9.10}$$

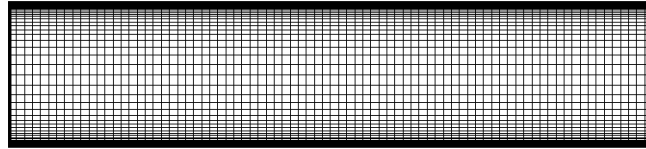$$w = 0, \quad \textbf{for} \quad y = H \tag{9.11}$$

then:

$$C_1 = 0, \quad C_2 = -\frac{1}{\mu} \frac{\Delta p}{L} \frac{H}{2} \tag{9.12}$$

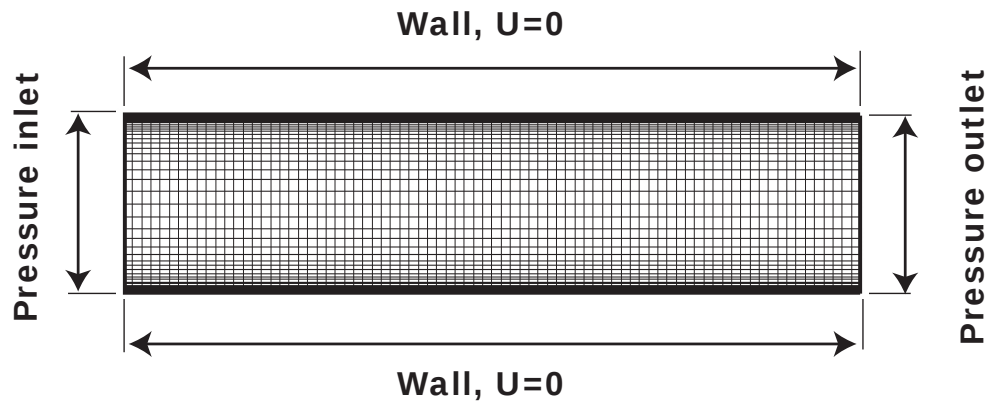Now, we have the analytical equation for velocity distribution in the gap between two plates:

$$w = \frac{1}{2\mu} \frac{\Delta p}{L} (y^2 - Hy) \tag{9.13}$$

(a) The geometry of the gap between two flat plates

(b) Mesh: 80x50 cells

Figure 9.2: Gap between two flat plates

Figure 9.3: Test case computational domain and boundary conditions

9.1.2 Test case set up

The introduced numerical steady state method[1], based on structured grid and explicit scheme with artificial viscosity, was applied on the following test case. The fluid is Newtonian. The test case is assumed to be laminar. Used geometry is the straight channel introduced in figure 9.2.

We want to compare the numerical solution (fully developed velocity profile) with the analytical solution given by equation (9.13). The test case parameters are: $L = 4.5$, $H = 1.0$, $\Delta p = 1.0$, $\mu = 0.01$, $\rho = 1$. The boundary conditions are following: At the walls of the channel the velocity components are zero and pressure is extrapolated. At the inlet is kept constant pressure ($p = 1.0$) and velocity components were extrapolated. At the outlet is kept constant pressure ($p = 0.0$) and velocity components were extrapolated. The computational mesh is of 80 x 50 x 1 cells.
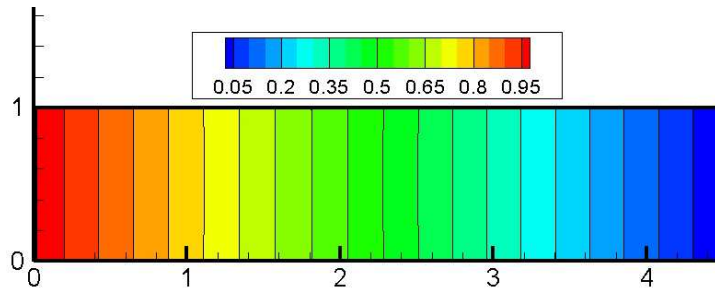
---

[1]solver: $k$rysa+
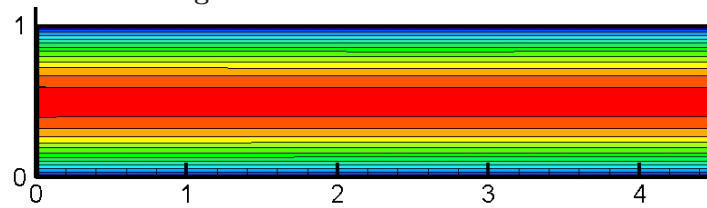
Figure 9.4: Pressure distribution
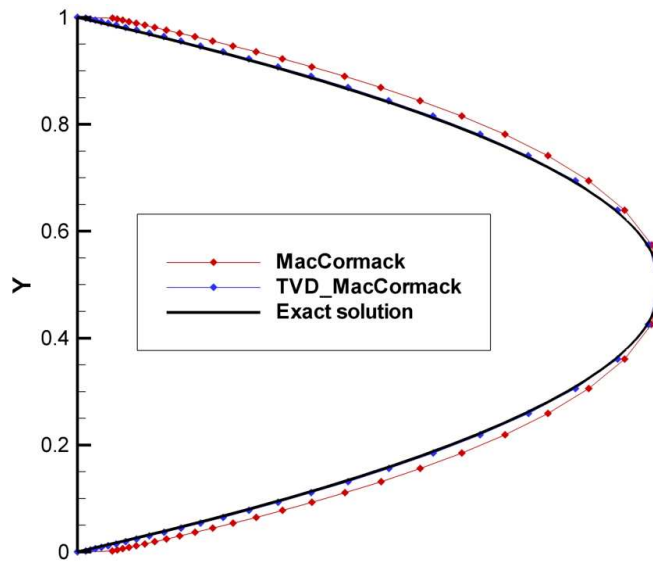

Figure 9.5: Velocity magnitude

Figure 9.6: Comparison of velocity profiles
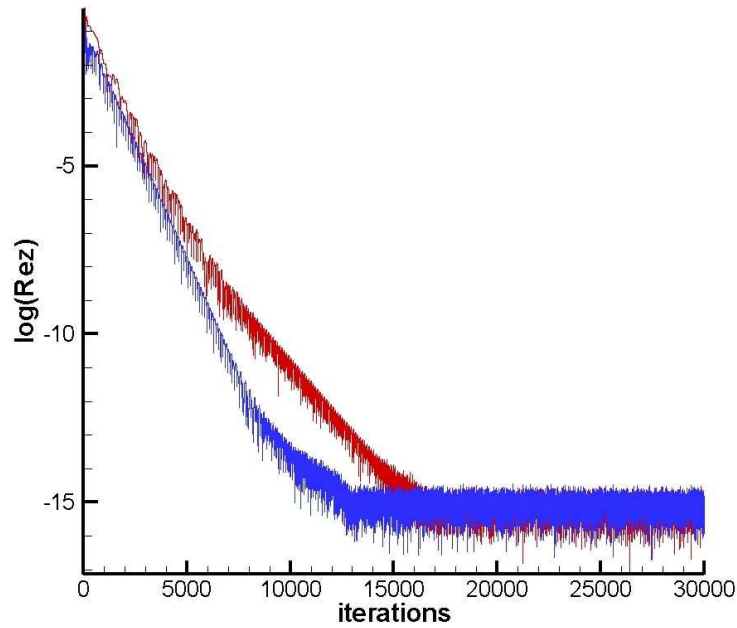
Figure 9.7: u-component residual history of iteration process, blue color is TVD MacCormack scheme, the red color is original MacCormack scheme

9.1.3   Test case conclusion

Pressure magnitude (figure 9.4) is, as expected, linearly decays from the inlet to the outlet. Velocity magnitude (figure 9.5) is of the same parabolic profile in all the computational domain. Figure 9.6 shows final comparison of analytical solution and two computed schemes, the first one is MacCormack scheme with von Neumann artificial viscosity introduced in Section 7.5.1 and the second one is TVD MacCormack scheme introduced in Section 7.5.2. Figure 9.7 shows residual history of iteration process for u-component of velocity. The blue color belongs to TVD MacCormack scheme and the red color belongs to the MacCormack scheme.

The first numerical method (MacCormack with von Neumann artificial viscosity) appears to be very sensitive to the choice of artificial viscosity coefficients. The second numerical method (Modified Causon's TVD MacCormack scheme) is a little bit more time consuming, but appears to be closer to analytical solution. The convergence of both numerical methods is very good thanks to the low Reynolds number. After all, both introduced numerical methods show good agreement with derived analytical solution of Navier-Stokes equations in the channel.

9.2 $\mathfrak{C}_2$: Flat Plate Test Case

9.2.1   The aim of the test case

The aim of this test case is to compare the results of methods introduced in chapter 7 with empirical data. This validation test case aimed on external aerodynamics, with high Reynolds number. The following test case is simplified to two dimensions. An important validation of the method, for viscous fluid flow, is a performance of skin friction coefficient c_f. It is in general the ratio of the inertial forces of an object being moved along a surface and of the force that maintains contact between the object and the surface. It can be expressed:

$$c_f = \frac{2\tau_w}{\rho U^2} \tag{9.14}$$

where ρ is a reference density and U is a reference velocity, τ_w is wall shear stress and for Newtonian fluid can be expressed:

$$\tau_w = \mu\left(\frac{\partial u}{\partial y}\right)_{y=0} \tag{9.15}$$

For this test case (infinite flat plate) the friction coefficient c_f is following (correlation between experimental measurements and DNS simulations):

$$\text{Laminar case:} \quad c_f = \frac{0.664}{Re_x^{\frac{1}{2}}}, \quad \text{Turbulent case:} \quad c_f = \frac{0.445}{\ln^2(0.06 \cdot Re_x)} \tag{9.16}$$

where:

$$Re_x = \frac{\rho \cdot U \cdot x}{\mu} \tag{9.17}$$

9.2.2   Test case set up

Reynolds number of the case is $Re = 2.0 \cdot 10^5$. The test case is assumed to be laminar[2]. The fluid is Newtonian. We have performed numerical simulation[3] on the flat plate. The governing equations are the same as in previous test case (standard Navier-Stokes equations for viscous, incompressible, Newtonian fluid). Figure 9.8 shows the computational domain of the test case. Flat plate begins at the origin and ends at the point [1,0]. The computational mesh has 100 x 41 x 1 cells and is displayed in the figure 9.9.

---

[2]the transition to turbulence is approximately for $Re = 500000$
[3]solver: krysa+
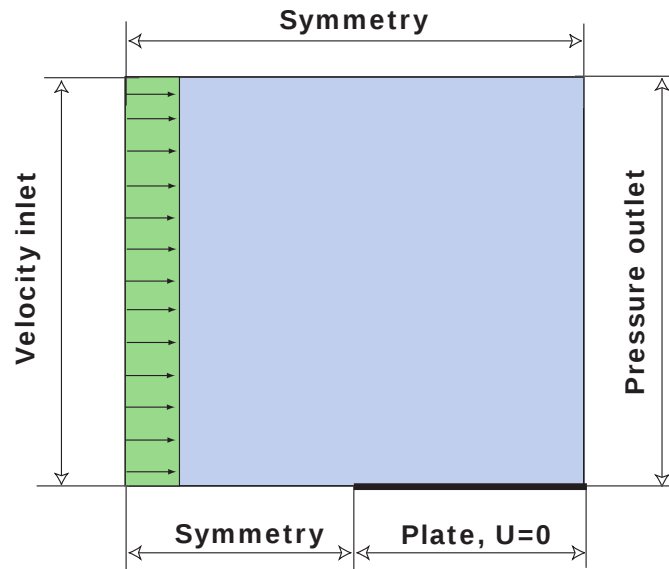
Figure 9.8: Flat plate computational domain and boundary conditions
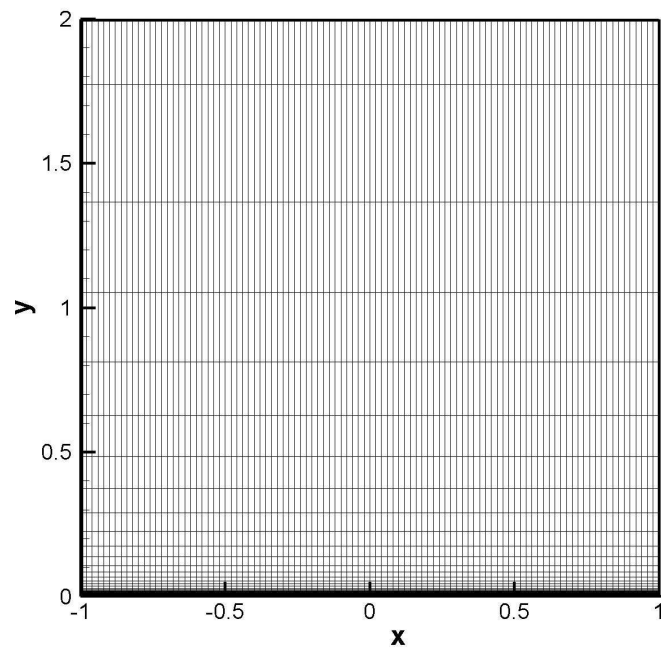
Figure 9.9: The flat plate mesh, 100x41x1 cells

(a) Comparison of friction coefficient c_f

(b) Comparison of velocity profiles
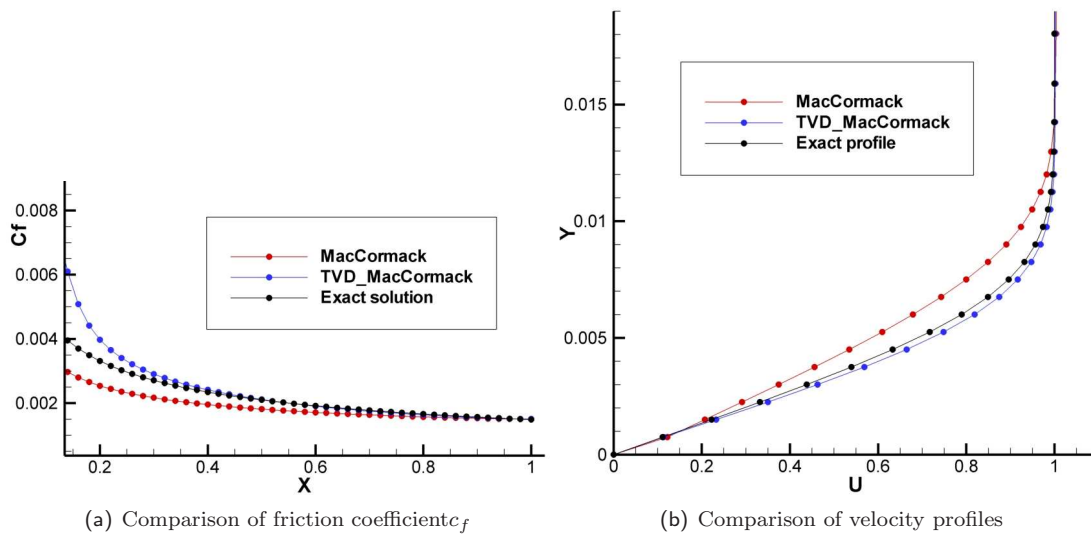
Figure 9.10: Endless flat plate results

9.2.3   Test case conclusion

Figure 9.10 shows the final comparison of the experimental solution and both computed schemes. The first numerical method (MacCormack with von Neumann artificial viscosity (7.5.1)) confirms to be very sensitive on choice of artificial viscosity coefficients. The second numerical method (Modified Causon's TVD MacCormack scheme (7.5.2)) is a little bit more time consuming, but appears to be closer to experimental solution. Figure 9.10 shows comparison of c_f obtained profiles with experimental solution. Figure 9.10 shows comparison of obtained velocity profiles in the developed boundary layer ($x = 0.9$) with the experimental solution. Both introduced numerical methods show good agreement with experimental solution.

9.3 $\mathfrak{C}_3$: Newtonian Flow in Stenosed Vessel, Comparison of Solvers

9.3.1 The aim of the test case

The aim of the following test case is to compare both solvers introduced in chapter 8. This test case is simplified to two dimensions. The identical test case was solved using Finite Element solver by another group at Charles University in Prague[4]. The details of Finite Element solver[5] are enclosed in Appendix A. All together there are three solvers to compare in this case. Both geometry and flow conditions are set to best imitate real human blood flow in the stenosed vessel. The test case computational domain is the contracted channel. Its narrowing and widening parts are of cosine shape. The widening part of the channel is of twice length than the narrowing part. Such a channel may simulate an idealized body vessel (vessel stenosis). The same test case was computed by *Leuprecht A. & K. Perktold* [58] and *Bodnár T. & A. Sequeira* [16].

9.3.2 Test case set up

The diameter of the channel is $D = 2R = 6.2$ mm. The mean inlet velocity is $U = 6.15\ cm.s^{-1}$ of parabolic profile derived in case $\mathfrak{C}_1$. The fluid density is $\rho = 1000\ kg/m^3$. Reynolds number of the case is $Re = 100$. The test case is assumed to be laminar. The fluid is Newtonian. The computational mesh has 200 x 46 x 1 cells, exactly the same for all three solvers.
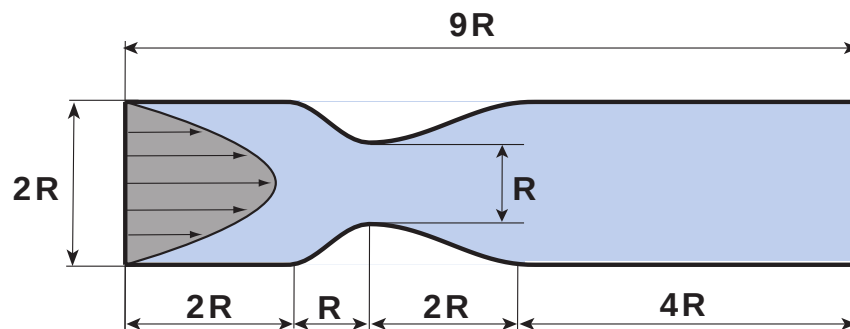
Figure 9.11: Contracting channel geometry

9.3.3 Test case conclusion

Set of figures 9.12 shows comparison of pressure distribution for all three solvers. Set of figures 9.13 shows comparison of pressure distribution for all three solvers. Set of figures 9.14 shows comparison of pressure and velocity distribution along centerline of the channel and the velocity profiles (in the narrowest section of the channel and in the end of the channel). Solver krysaFOAM (Finite Volume Method, modified OpenFOAM solver) and solver FEM (Finite Element Method solver, Charles University) have fantastic agreement. Both pressure and velocity field are almost identical. Solver krysa+ (Finite Volume Method) shows a slide difference. After all, all introduced solvers show good agreement each other solving Navier-Stokes for incompressible, viscous, Newtonian fluid.

---

[4]Karel Tůma
[5]solver FEM

(b) Solver: krysaFOAM

(c) Solver: krysa+

(d) Solver: FEM
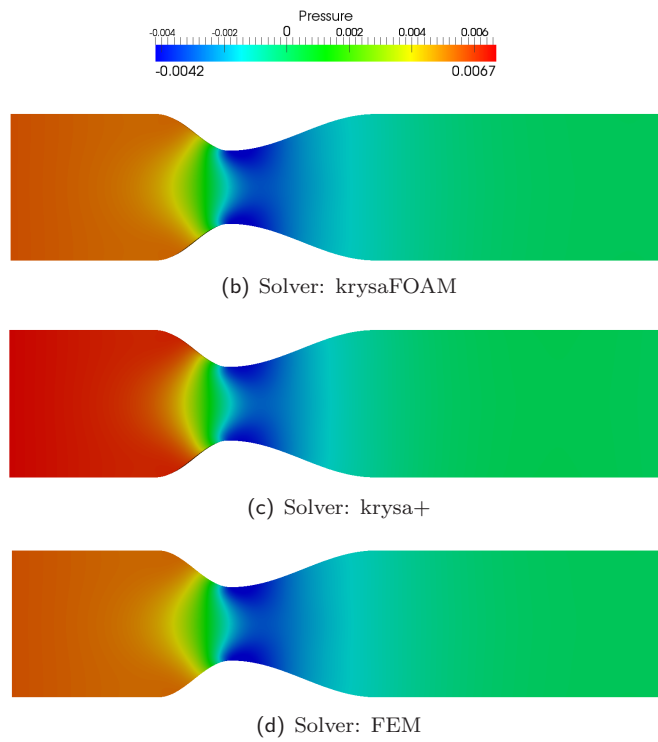
Figure 9.12: Comparison of solvers, pressure distribution

(b) Solver: krysaFOAM

(c) Solver: krysa+

(d) Solver: FEM
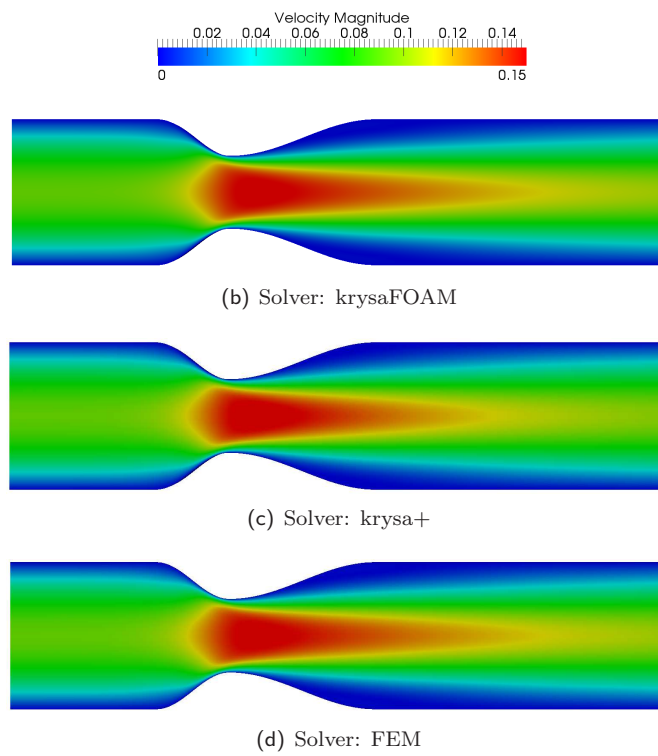
Figure 9.13: Comparison of solvers, velocity magnitude
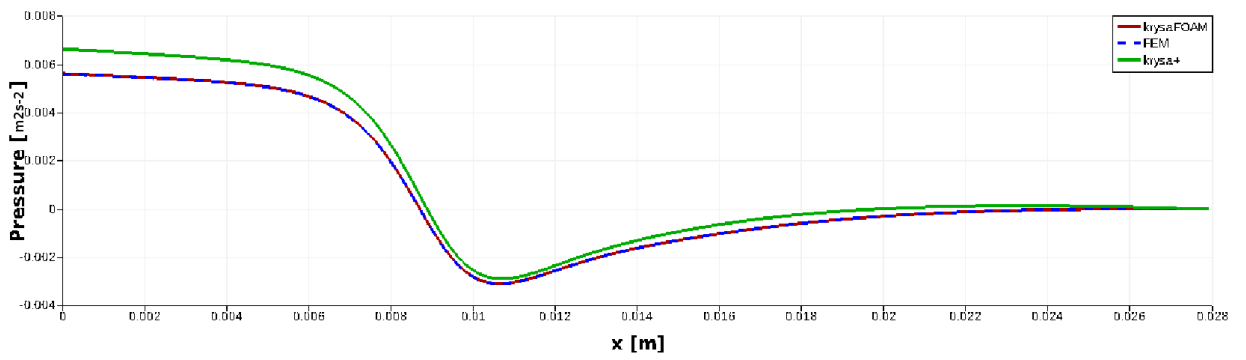
(a) Pressure along centerline
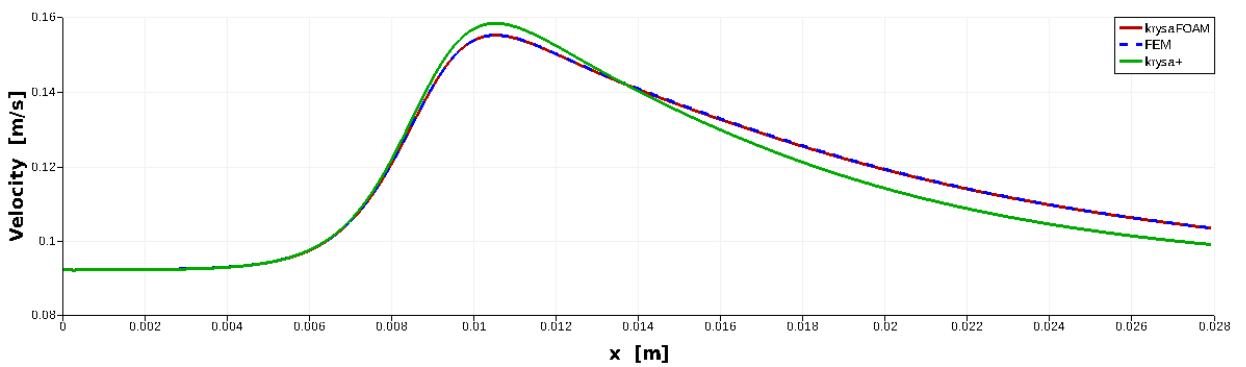
(b) Velocity along centerline
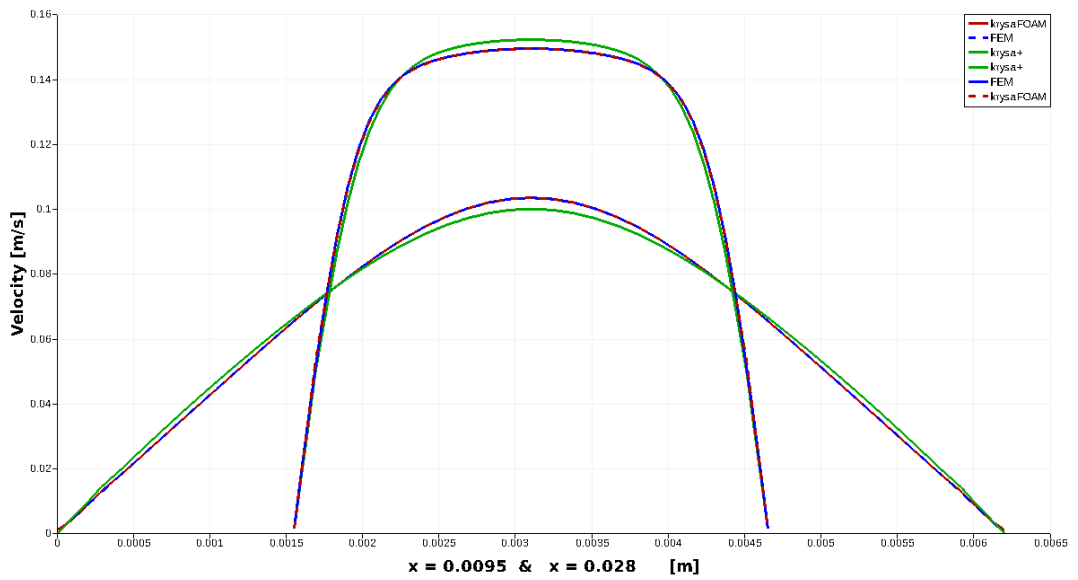
(c) Velocity profiles at the narrowest section and in the end of channel

Figure 9.14: Comparison of solvers

Chapter 10

Tests of Generalized Newtonian Models

Contents

10.1 $\mathfrak{C}_4$: Fully Developed Flow of Generalized Newtonian Fluid in a Pipe

10.1.1   The aim of the test case

The aim of the following test case is to demonstrate the differences in the developed velocity profiles in a straight channel. As already mentioned, there are significant differences between Newtonian and generalized Newtonian flows described in chapter 4. This test case is simplified to two dimensions. The developed velocity profiles for Newtonian fluid flow and for generalized Newtonian shear-thinning fluid flow are not equal because of different magnitude of shear-rate $\dot{\gamma}$ (shear rate is not linear for shear thinning fluid flow). The following schematic picture shows theoretical differences in developed velocity profiles for Newtonian fluid flow and for generalized Newtonian shear-thinning fluid flow:

Newtonian Flow   **Non-Newtonian Flow**
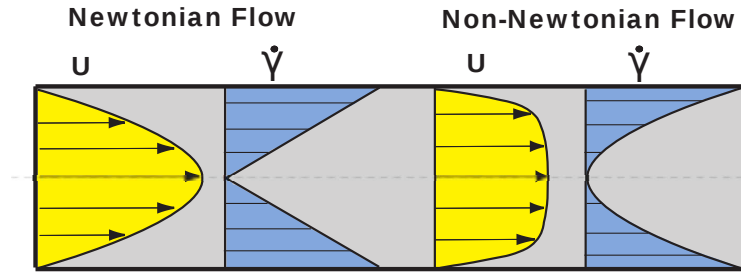
Figure 10.1: Example of developed velocity profiles and corresponding shear rates

10.1.2   Test case set up

Two tests were solved: Newtonian and generalized Newtonian (shear-thinning). The test case set up[1] is the same as $\mathfrak{C}_1$, now comparing developed velocity profiles having Newtonian and generalized Newtonian shear-thinning flows. The diameter of the channel is $D = 2R = 6.2$ mm. At the inlet is prescribed parabolic velocity profile, mean value $U = 6.15$ $cm.s^{-1}$, using equation (9.13). The computational mesh has 80 x 50 x 1 cells. Reference viscosity for Newtonian case is infinity shear viscosity ($\mu = \mu_\infty = 0.00345$ Pa.s). The fluid density is $\rho = 1000$ kg/m^3. Reynolds number of the case is $Re = 111$. The test case is assumed to be laminar. For generalized Newtonian case is used Modified Cross model[2]:

$$\mu(\dot\gamma) = \mu_\infty + (\mu_0 - \mu_\infty)\left[\frac{1}{[1 + (\alpha\dot\gamma)^m]^a}\right] \tag{10.1}$$

where $\mu_0 = 0.056$ $Pa \cdot s$, $\mu_\infty = 0.00345$ $Pa \cdot s$, $\alpha = 3.736$ s, $m = 2.406$, $a = 0.254$. The viscosity dependence on the shear-rate, which is generated by the Modified Cross model is shown in the figure 10.2.
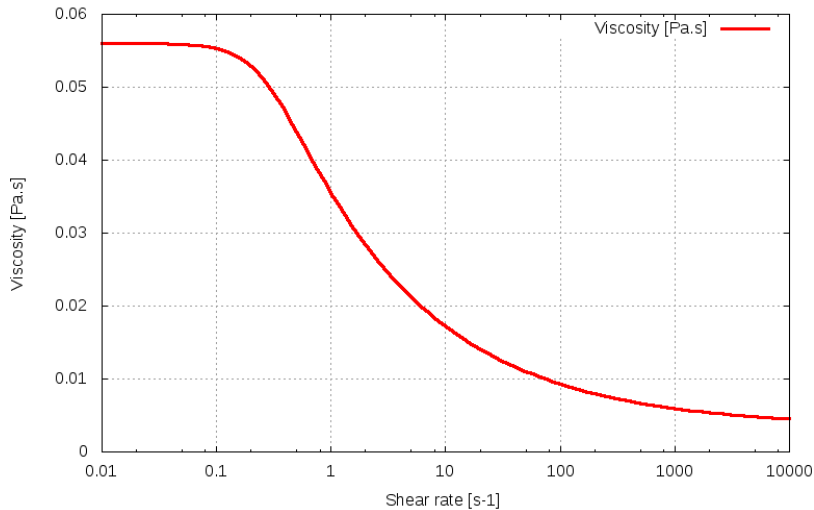
Figure 10.2: Viscosity generated by Modified Cross model

---

[1]solver: krysa+
[2]described in the table 4.1

(a) Newtonian flow, velocity magnitude   (b) generalized Newtonian flow, velocity magnitude
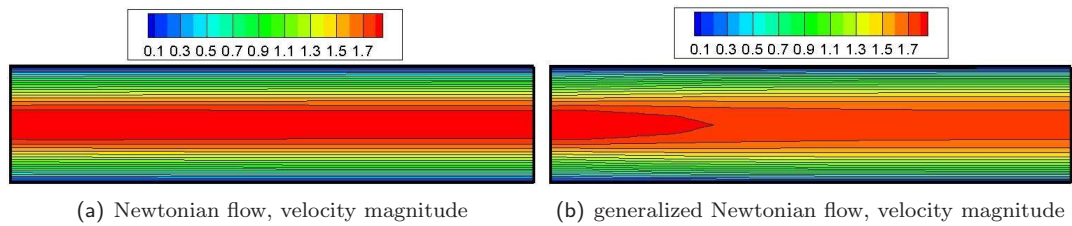
Figure 10.3: Comparison of velocity magnitude for Newtonian fluid flow and shear-thinning flow

(a) Velocity profiles
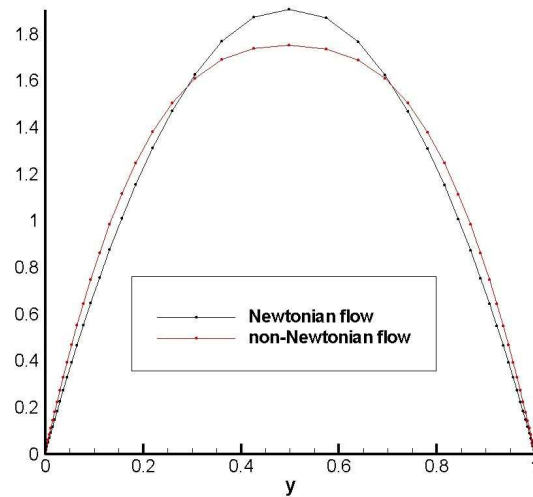
Figure 10.4: Comparison of developed velocity profiles for Newtonian fluid flow and shear-thinning flow

10.1.3 Test case conclusion

Figure 10.3 shows velocity magnitude for Newtonian fluid flow and generalized Newtonian shear-thinning fluid flow. Figure 10.3 shows developed velocity profiles for Newtonian fluid flow and generalized Newtonian shear-thinning fluid flow. The numerical results shoved significant differences between above mentioned types of flow. One can see that generalized Newtonian shear-thinning flow is slower in the center of the channel because of the local increase of viscosity, generalized Newtonian shear-thinning flow is faster in regions with large velocity gradients (typically near the walls), where the viscosity model gives lower effective viscosity than Newtonian fluid's viscosity. (It is consistent with generalized Newtonian shear-thinning fluid flow properties, e.g. blood micro-structure could be interpreted to be cut by the layers of fluid, such an effect locally decreases viscosity.).

10.2 $\mathfrak{C}_5$: Comparison of Generalized Newtonian Shear-Thinning Viscosity Models in Contracting Channel

10.2.1   The aim of the test case

The aim of the following test case is to compare eight viscosity models for generalized Newtonian fluid introduced in the table 4.1. All the viscosity models are set to imitate the viscosity of human blood. The asymptotic viscosities are the same for all viscosity models ($\mu_0 = 0.056\ Pa \cdot s$, $\mu_\infty = 0.00345\ Pa \cdot s$). The only difference among models is the model function, that is fitted to empirical data. The model coefficients are calibrated for human blood adopted from *Cho & Kensey* [30].

To compare these models' performances we have set up the following test case. The geometry of the computational domain is contracting channel introduced in test case $\mathfrak{C}_3$.

10.2.2   Test case set up

All together nine tests were computed. One for Newtonian fluid, eight for generalized Newtonian shear-thinning fluid to test eight viscosity models from the table 4.1. The flow conditions of the test case are set to simulate the human blood behavior[3]. The computational mesh is of 100 x 40 x 1 cells. The diameter of the channel is $D = 2R = 6.2$ mm. At the inlet is prescribed parabolic velocity profile of mean value $U = 6.15\ cm.s^{-1}$, using equation (9.13). The computational mesh is of 80 x 50 x 1 cells. Reference viscosity for Newtonian case is infinity shear viscosity ($\mu = \mu_\infty = 0.00345$ Pa.s). The fluid density is $\rho = 1000\ kg/m^3$. Reynolds number of the case is $Re = 111$. The test case is assumed to be laminar. For generalized Newtonian case is used Modified Cross model[4]:

$$\mu(\dot{\gamma}) = \mu_\infty + (\mu_0 - \mu_\infty)\left[\frac{1}{[1 + (\alpha\dot{\gamma})^m]^a}\right] \tag{10.2}$$

where $\mu_0 = 0.056\ Pa \cdot s$, $\mu_\infty = 0.00345\ Pa \cdot s$, $\alpha = 3.736\ s$, $m = 2.406$, $a = 0.254$. The viscosity dependence on the shear-rate, which is generated by the Modified Cross model is shown in the figure 10.2.

10.2.3   Test case conclusion

Figure 10.5 shows comparison of results obtained using generalized Newtonian viscosity models from Table (4.1). The left column is velocity magnitude, the right column is viscosity magnitude. We can observe characteristic trend for all viscosity models: In the regions with large velocity gradients, the viscosity is low. For regions with small velocity gradients all the models give high viscosity. All the generalized Newtonian shear-thinning viscosity models give similar velocity magnitude for this test case. One can see, that there are some differences in models' viscosity magnitude. After all, the trends are the same for all eight tested models.

---

[3]solver: krysa+
[4]described in the table 4.1

(a) Newtonian, velocity magnitude

(b) Newtonian, viscosity magnitude

(c) Power Law Model, velocity magnitude

(d) Power Law Model, viscosity magnitude

(e) Modified Cross Model, velocity magnitude

(f) Modified Cross Model, viscosity magnitude

(g) Powel-Eyring model, velocity magnitude

(h) Powel-Eyring model, viscosity magnitude

(i) Modified Powel-Eyring model, velocity magnitude

(j) Modified Powel-Eyring model, viscosity magnitude

(k) Cross Model, velocity magnitude

(l) Cross Model, viscosity magnitude

(m) Simplified Cross Model, velocity magnitude

(n) Simplified Cross Model, viscosity magnitude

(o) Carreau Model, velocity magnitude

(p) Carreau Model, viscosity magnitude

(q) Carreau-Yasuda Model, velocity magnitude

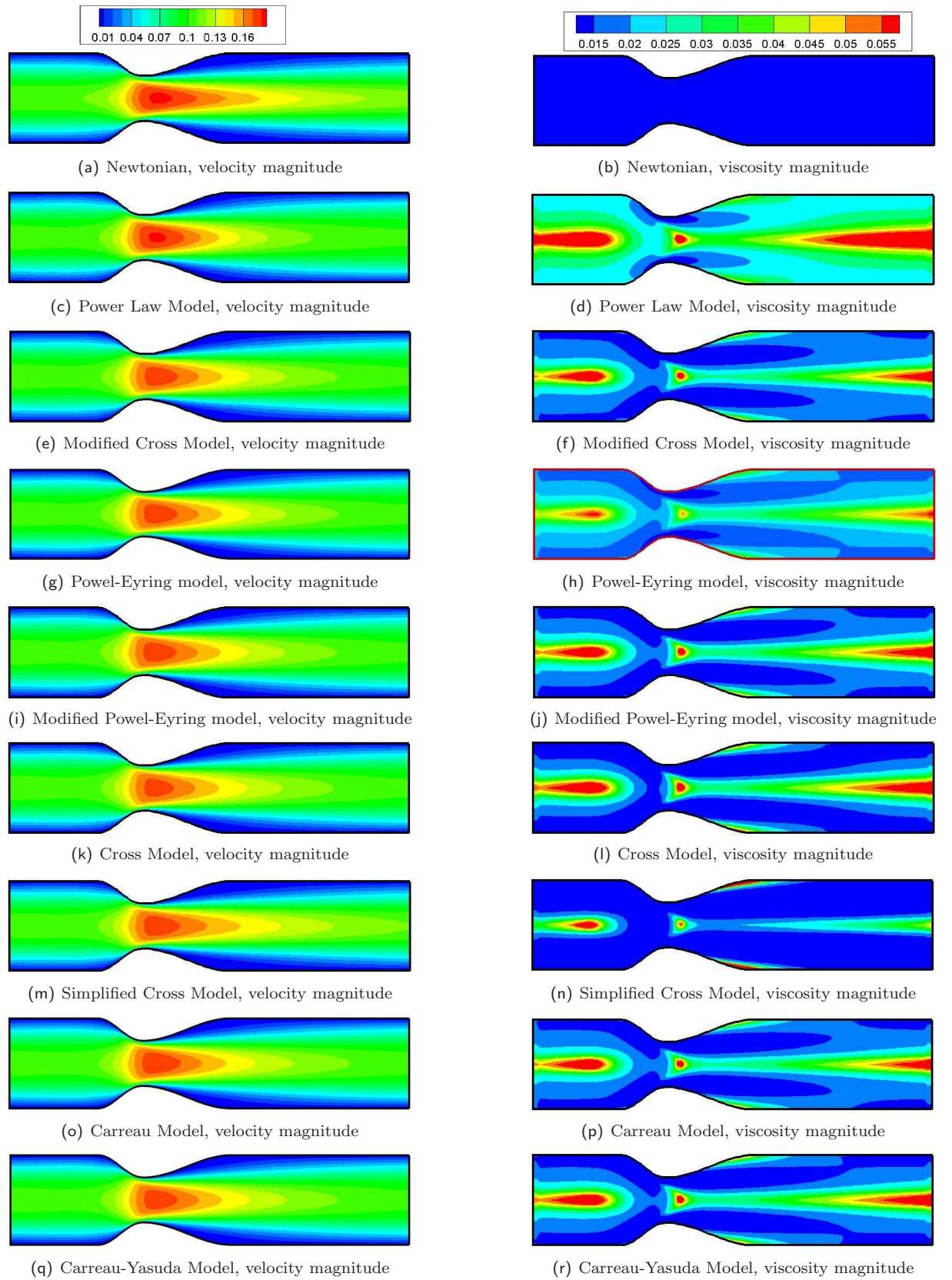(r) Carreau-Yasuda Model, viscosity magnitude

Figure 10.5: Comparison of generalized Newtonian shear-thinning viscosity models

10.3　$\mathfrak{C}_6$: Estimation of Reference Viscosity

10.3.1　The aim of the test case

The following test case deals with a simple question. If a generalized Newtonian shear thinning fluid flow should be represented by Newtonian fluid flow, what should be its viscosity[5]? Or, in other words, what viscosity of Newtonian fluid flow best fits the generalized Newtonian fluid flow.

　　This test case is simplified to two dimensions. We want to find the reference viscosity, which best describes the blood flow. We have constructed and tested six different hypothesis of definition of reference blood viscosity μ_i^{ref}. We start with simple hypothesis and then gradually come to the more sophisticated ones. The first two hypotheses try to find viscosity directly. Another two hypotheses try to find the correct shear-rate $\dot{\gamma}_{ref}$ and then determine the reference blood viscosity from viscosity model formula. The remaining two hypothesis use the numerical solution approach. As a reference model for generalized Newtonian fluid is used Modified Cross model:

$$\mu(\dot{\gamma}) = \mu_\infty + (\mu_0 - \mu_\infty)\left[\frac{1}{[1 + (\alpha\dot{\gamma})^m]^a}\right] \tag{10.3}$$

　　where $\mu_0 = 0.056\ Pa \cdot s$, $\mu_\infty = 0.00345\ Pa \cdot s$, $\alpha = 3.736\ s$, $m = 2.406$, $a = 0.254$. The viscosity dependence on the shear-rate, which is generated by the Modified Cross model is shown in the figure 10.2.

10.3.2　Six hypothesis for constructing reference viscosity

1. The *first hypothesis* is simple and considers μ_1^{ref} to be equal μ_∞ for Modified Cross model.

$$\mu_1^{ref} = \mu_\infty = 0.00345\quad Pa \cdot s \tag{10.4}$$

2. The *second hypothesis* considers μ_2^{ref} to be an average value of μ_0 and μ_∞:

$$\mu_2^{ref} = \frac{\mu_0 + \mu_\infty}{2} = \frac{0.0560 + 0.00345}{2} = 0.029725\quad Pa \cdot s \tag{10.5}$$

3. In the *third hypothesis* we assume the average shear rate $\bar{\dot{\gamma}}_{anl}$ that corresponds to the Newtonian fluid flow. An average shear rate $\bar{\dot{\gamma}}_{anl}$ we can determine from Newtonian velocity profile and then evaluate the viscosity from the equation (10.11).

$$\mu_3^{ref} = 0.005767\quad Pa \cdot s \tag{10.6}$$

4. In the *fourth hypothesis* we assume an maximal shear rate $\dot{\gamma}_{max}$ that corresponds to the Newtonian flow and then evaluate the viscosity from following idea. Let us construct the curve of the formula defining Modified Cross viscosity model, see figure 10.7. The viscosity μ_4^{ref} can be found as a mean value of viscosity up to the maximal shear rate $\dot{\gamma}_{max}$.

$$\mu_4^{ref} = \frac{\int_0^{\dot{\gamma}_{max}} \mu(\dot{\gamma})d\dot{\gamma}}{\dot{\gamma}_{max}} = 0.00707\quad Pa \cdot s \tag{10.7}$$

5. In the *fifth hypothesis* we start with simple numerical simulation. The simulation of generalized Newtonian fluid flow in the simple straight channel[6] is performed in the first step. Modified Cross model is used for generalized Newtonian viscosity computation. From developed velocity profile (non-Newtonian) we can obtain the mean value of shear rate $\bar{\dot{\gamma}}_{sim}$. Having this value we can easily evaluate μ_5^{ref} from Modified Cross model.

$$\mu_5^{ref} = 0.005600\quad Pa \cdot s \tag{10.8}$$

---

[5]solvent viscosity, a constant
[6]exactly the same geometry as in the case $\mathfrak{C}_6$
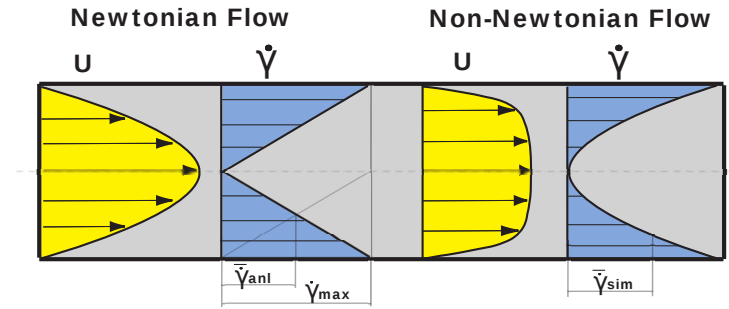
Figure 10.6: Reference shear-rate illustration

6. In the *sixth hypothesis* we start with numerical simulation again. The simulation of generalized Newtonian fluid flow in the straight channel is made. Modified Cross model is used for generalized Newtonian viscosity computation. The viscosity μ_6^{ref} is evaluated as an average of generalized Newtonian viscosity, that is generated by the model, in the outlet cross-section of the channel.

$$\mu_6^{ref} = 0.006103 \quad Pa \cdot s \tag{10.9}$$
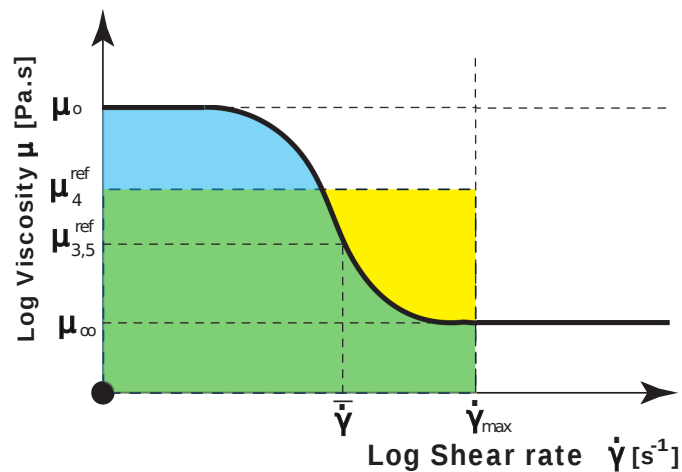
Figure 10.7: Reference viscosity illustration

10.3.3   Test case set up

All together seven cases were solved. One for generalized Newtonian shear-thinning fluid and six for Newtonian fluid to test six reference viscosity hypothesis. The flow conditions of the test case are set to simulate the human blood behavior[7]. The computational mesh has 100 x 40 x 1 cells. The diameter of the channel is $D = 2R = 6.2$ mm. At the inlet is prescribed parabolic velocity profile of mean value $U = 6.15$ $cm.s^{-1}$, using equation (9.13). The fluid density is $\rho = 1000 \ kg/m^3$. Reynolds number of the case is $Re = 111$. The test case is assumed to be laminar. To compare the tested hypothesis we have computed the generalized Newtonian shear-thinning fluid flow to serve as a reference data. For computation of variable viscosity we have used *Modified Cross Model* see table 4.1.

---

[7]solver: krysa+

10.3.4   Results

Reference generalized Newtonian case

The set of figures 10.8 shows the reference test case results (generalized Newtonian shear-thinning fluid flow).

(a) Velocity magnitude

(b) Flow streamtraces

(c) Pressure magnitude

(d) Viscosity magnitude
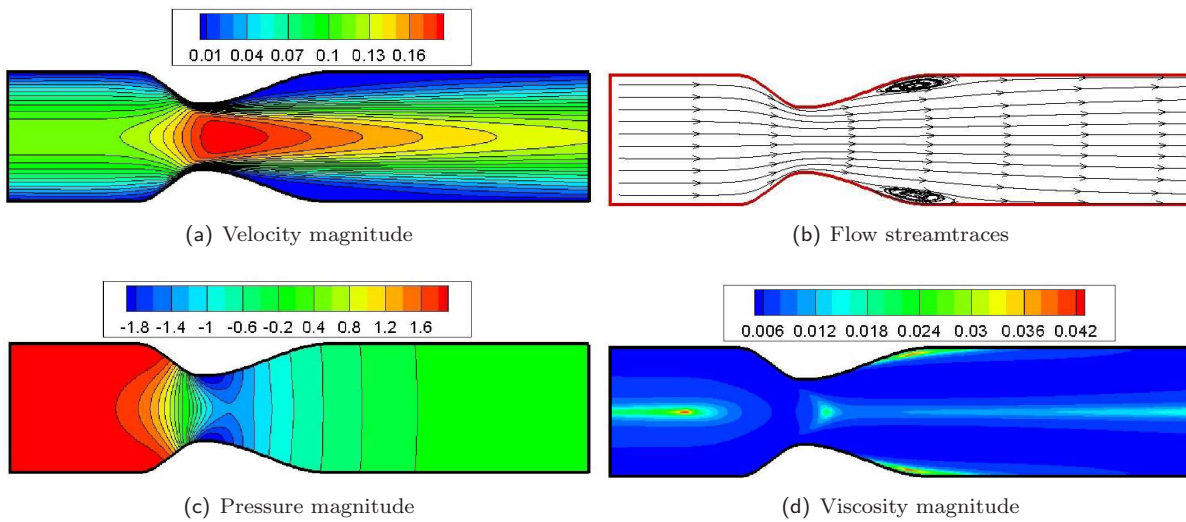
Figure 10.8: generalized Newtonian (reference) test case

All the six hypothesis' cases were solved and compared to the reference case (generalized Newtonian). Three test outputs were compared (the first one is pressure distribution along the centerline of the channel, the second one is position of the reattachment point, the third one is wall shear stress). All the test cases' results are symmetric along the centerline of the channel. To evaluate all the hypothesis' results were assigned grades (0 - the worst, 5- the best) and evaluated at the end of the section.

Pressure distribution along the centerline of the channel

The first comparison is based on the pressure distribution along the centerline (axis of symmetry) of the channel. The figure 10.9 shows the pressure distribution along the centerline of the channel. We can see that hypotheses number two totally failed, other hypothesis give comparable results. The table 10.1 shows numerical comparison, where the percentage deviation is considered to be a sum of all the differences from the reference case divided by an average value of the reference pressure. The best results in this criteria were achieved by hypothesis 4 and 5.

(a) Centerline pressure distribution

(b) Wall shear stress comparison
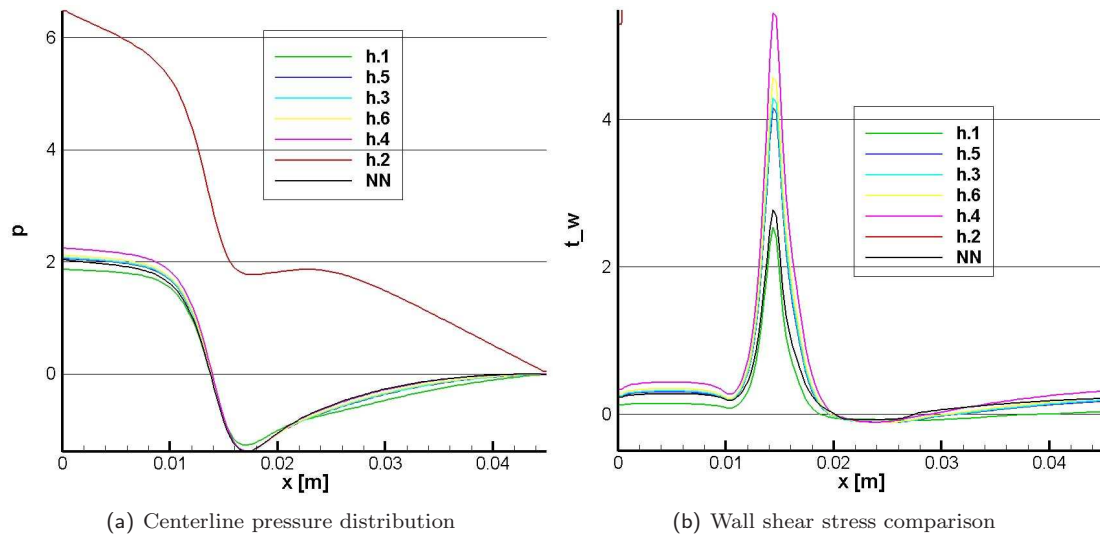
Figure 10.9: Comparison of pressure and wall shear stress distribution

Hypothesis No.	NN	1	2	3	4	5	6
Relative deviation	**0.000**	13.071	298.773	6.500	9.240	6.375	7.134
Success points	-	1	0	4	2	5	3

Table 10.1: Comparison of centerline pressure distribution

Reattachment point position

The second comparison method is based on the length of recirculation zones that appear in the expanding part of the channel. We have followed the reattachment point of recirculation zones measured from the beginning of the computational domain as it is sketched in figure 10.10. The best hypotheses appears to be number 4. Hypothesis number 1 and 2 showed unsatisfactory prediction, hypotheses number 2 doesn't even show any recirculation zone at all!
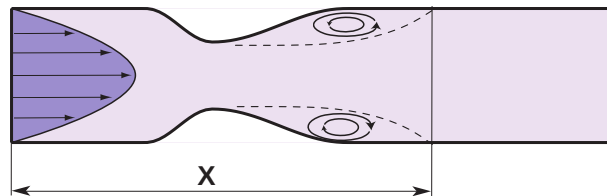
Figure 10.10: Reattachment point position

The table below shows the lengths (in diameters of channel) of the recirculation zones according to the figure 10.10.

Hypothesis No.	NN	1	2	3	4	5	6
X	**2.7398**	3.8972	0.00000	3.1025	2.8821	3.1404	3.0402
Success points	-	1	0	3	5	2	4

Table 10.2: Reattachment point position comparison

Wall shear stress

The third comparison method is shear stress distribution at the wall. The shear stress distribution at the wall is shown in the figure 10.9.

The table below shows comparison of shear stress at the (lower) wall. The relative deviation was evaluated in the same way as in already mentioned pressure comparison. Here, hypothesis number 5 shows the best agreement while number 2 totally failed again.

Hypothesis No.	NN	1	2	3	4	5	6
Percentage deviation	**0.000**	42.031	7680.780	43.520	77.246	40.591	49.690
Success points	-	4	0	3	1	5	2

Table 10.3: Wall shear stress comparison

10.3.5 Test case conclusion

The table below (Table 10.4) shows final comparison of all six tested hypotheses (Usability means grades, A is the best, F is the worst). The best performance showed hypothesis number 5. Hypotheses 3, 4 and 6 appear usable as well. On the other hand, hypothesis 1 (μ_1^{ref} to be equal μ_∞) and hypothesis 2 (μ_2^{ref} to be an average value of μ_0 and μ_∞) appear to be wrong and their usage can't be recommended.

Hypothesis No.	1	2	3	4	5	6
Total success points	6	0	10	8	12	9
Usability	E	F	B	D	A	C

Table 10.4: Final comparison of tested hypothesis

It has turned out that the best hypothesis showed up to be hypothesis number five. Let's repeat the hypothesis: The simulation of generalized Newtonian fluid flow in the simple straight channel[8] is performed in the first step. Here, was used Modified Cross model for generalized Newtonian viscosity computation. From developed velocity profile we can obtain the mean value of shear rate $\bar{\dot{\gamma}}_{sim}$. Having this value we can easily evaluate μ_5^{ref} from Modified Cross model.

Thus, for selected geometry and flow conditions the viscosity that best describe blood flow is:

$$\mu_{blood}^{ref} = 0.005600 \quad Pa \cdot s \tag{10.10}$$

---

[8]exactly the same geometry as in the case $\mathfrak{C}_6$

10.4 $\mathfrak{C}_7$: Flow Rate Dependence Test Case

10.4.1 The aim of the test case

The aim of the following test case is to demonstrate the dependence of the viscosity (described by the generalized Newtonian shear-thinning viscosity model) on the flow-rate. A high flow-rate generates high velocity gradients[9] (and thus shear-rates $\dot{\gamma}$), which may have serious influence on the variable viscosity. This test case is simplified to two dimensions.
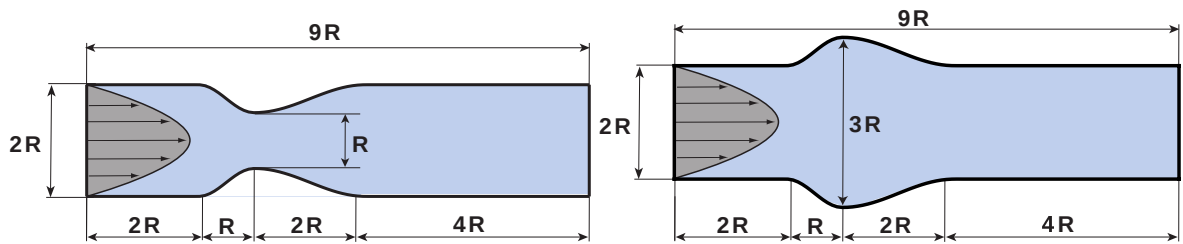
10.4.2 Test case set up

Figure 10.11: Test case geometries contracting and widening channels

All together 24 tests test simulations were performed. The fluid is generalized Newtonian shear-thinning fluid. The flow conditions of the test case are set to simulate the human blood behavior. The computational mesh has 100 x 40 x 1 cells. The diameter of the channel is $D = 2R = 6.2$ mm. At the inlet is prescribed parabolic velocity profile with mean value $U = 6.15 \ cm.s^{-1}$, using equation (9.13). The fluid density is $\rho = 1000 \ kg/m^3$. The test case is assumed to be laminar. For generalized Newtonian case is used Modified Cross model[10]:

$$\mu(\dot{\gamma}) = \mu_\infty + (\mu_0 - \mu_\infty)\left[\frac{1}{[1 + (\alpha\dot{\gamma})^m]^a}\right] \tag{10.11}$$

where $\mu_0 = 0.056 \ Pa \cdot s$, $\mu_\infty = 0.00345 \ Pa \cdot s$, $\alpha = 3.736 \ s$, $m = 2.406$, $a = 0.254$. The viscosity dependence on the shear-rate, which is generated by the Modified Cross model is shown in the figure 10.2.

There were performed twelve computations[11] for each geometry for decreasing flow rates: $Q/Q_0 = \frac{16}{1}$, $\frac{8}{1}$, $\frac{4}{1}$, $\frac{2}{1}$, $\frac{1}{1}$, $\frac{1}{2}$, $\frac{1}{4}$, $\frac{1}{8}$, $\frac{1}{16}$, $\frac{1}{32}$, $\frac{1}{64}$, $\frac{1}{128}$, where $Q_0 = 2cm^2/s$. For transparent interpretation of the viscosity magnitude, lets introduce relative viscosity:

$$\bar{\mu} = \frac{\mu(\dot{\gamma}) - \mu_\infty}{\mu_\infty} \tag{10.12}$$

$\bar{\mu}$ can be viewed as a measure of viscosity changes. One can define three viscosity regions with different characteristics. For $0 \le \bar{\mu} < 1$ (blue area in Figure 10.13), the viscosity is close to μ_∞ and doesn't change much. This is Low-viscosity region, showing "pseudo-Newtonian" behavior. For $1 \le \bar{\mu} < 10$ (green area in Figure 10.13), one can see highly generalized Newtonian region, where the viscosity strongly varies with shear rate. For $10 \le \bar{\mu}$ (red area in Figure 10.13), there is High-viscosity region, where the viscosity is high due to the low shear rate.

---

[9] high velocity gradients produce high shear-rate
[10] described in the table 4.1
[11] solver: krysa+
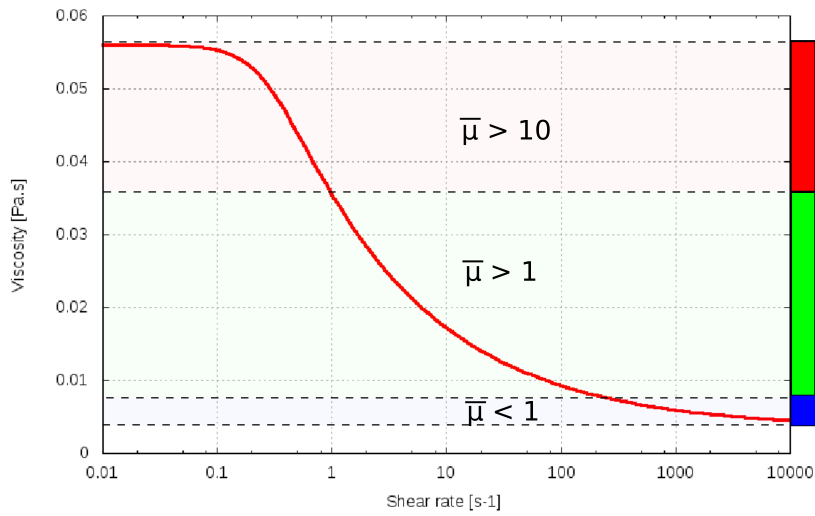
Figure 10.12: Viscosity generated by Modified Cross model with indicated relative viscosity scale

10.4.3   Test case conclusion

In the set of figures 10.14 and 10.13, one can see the relative viscosity magnitude contours for selected flow rates. Figure 10.12 shows the viscosity values generated by Modified Cross model. One can see that the generalized Newtonian shear-thinning fluid flow behavior of blood, viscosity magnitude strongly depends on the flow rate (having constant diameter of the channel).

For smaller flow rates the viscosity is high due to the lower shear-rate (small velocity gradient). At low shear-rates red blood cells create complicated structures, roulax, which cause high viscosity. Typical regions with smaller shear-rates are near the center of the channel.

For higher flow rates the viscosity is low due to the higher shear-rate (large velocity gradient). Typical regions with higher shear-rates are near the walls of the channel, where large velocity gradients appear.

Decreasing the flow rate the viscosity increases, in the other hand increasing flow rate the viscosity decreases. It is consistent with generalized Newtonian shear-thinning fluid flow properties. Blood structures could be interpreted to be cut by the layers of fluid, such an effect locally decreases viscosity.

(a) $Q/Q_0 = 16$

(b) $Q/Q_0 = 8$

(c) $Q/Q_0 = 4$

(d) $Q/Q_0 = 2$

(e) $Q/Q_0 = 1$

(f) $Q/Q_0 = 1/2$

(g) $Q/Q_0 = 1/4$

(h) $Q/Q_0 = 1/8$

(i) $Q/Q_0 = 1/16$

(j) $Q/Q_0 = 1/32$

(k) $Q/Q_0 = 1/64$

(l) $Q/Q_0 = 1/128$

Figure 10.13: Relative viscosity magnitude for various flow rates, $\bar{\mu} = (\mu(\dot{\gamma}) - \mu_\infty)/\mu_\infty$, in stenosed channel

(a) $Q/Q_0 = 16$

(b) $Q/Q_0 = 8$

(c) $Q/Q_0 = 4$

(d) $Q/Q_0 = 2$

(e) $Q/Q_0 = 1$

(f) $Q/Q_0 = 1/2$

(g) $Q/Q_0 = 1/4$

(h) $Q/Q_0 = 1/8$

(i) $Q/Q_0 = 1/16$

(j) $Q/Q_0 = 1/32$

(k) $Q/Q_0 = 1/64$

(l) $Q/Q_0 = 1/128$

Figure 10.14: Relative viscosity magnitude for various flow rates, $\bar{\mu} = (\mu(\dot{\gamma}) - \mu_\infty)/\mu_\infty$, in aneurism channel

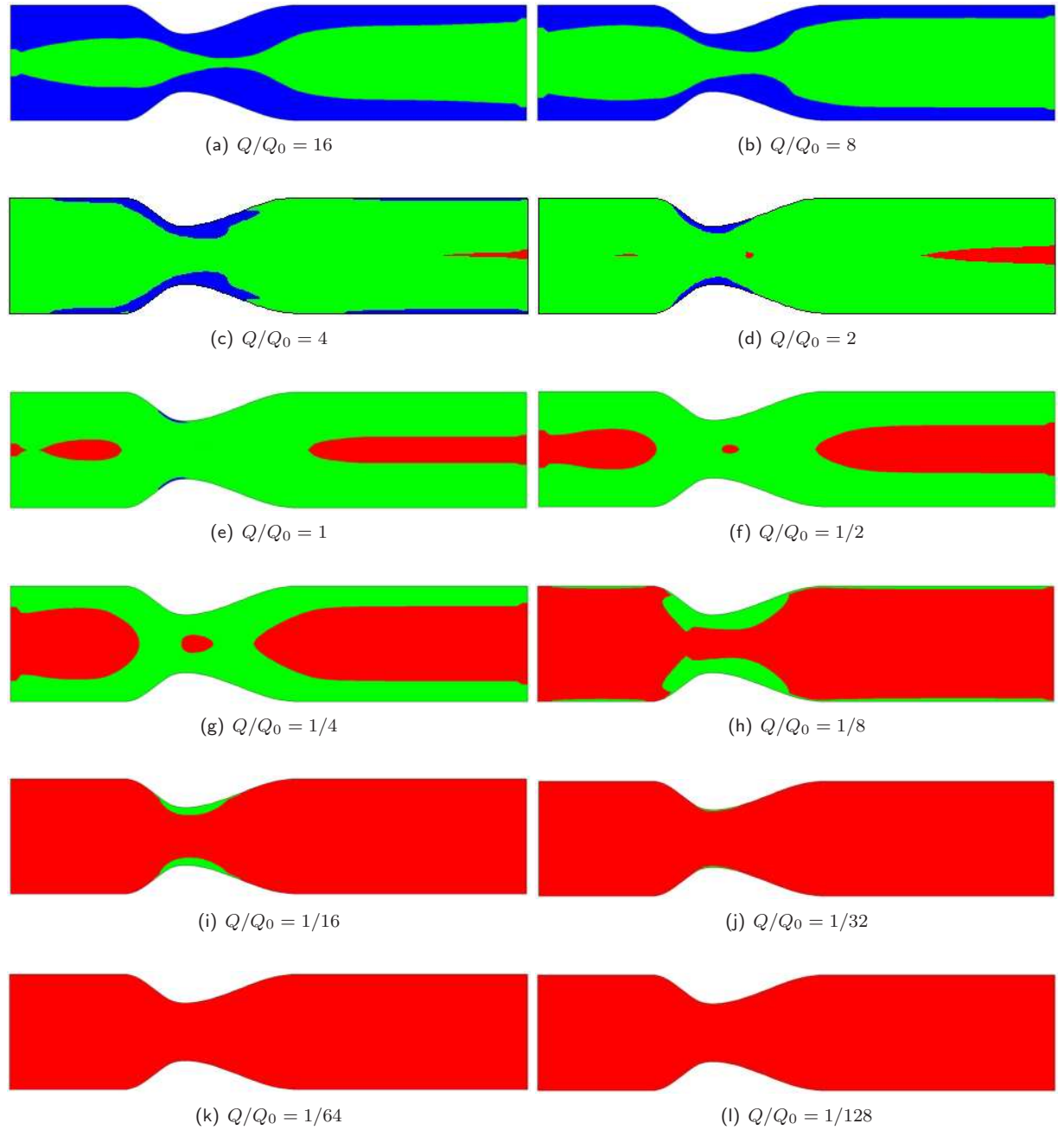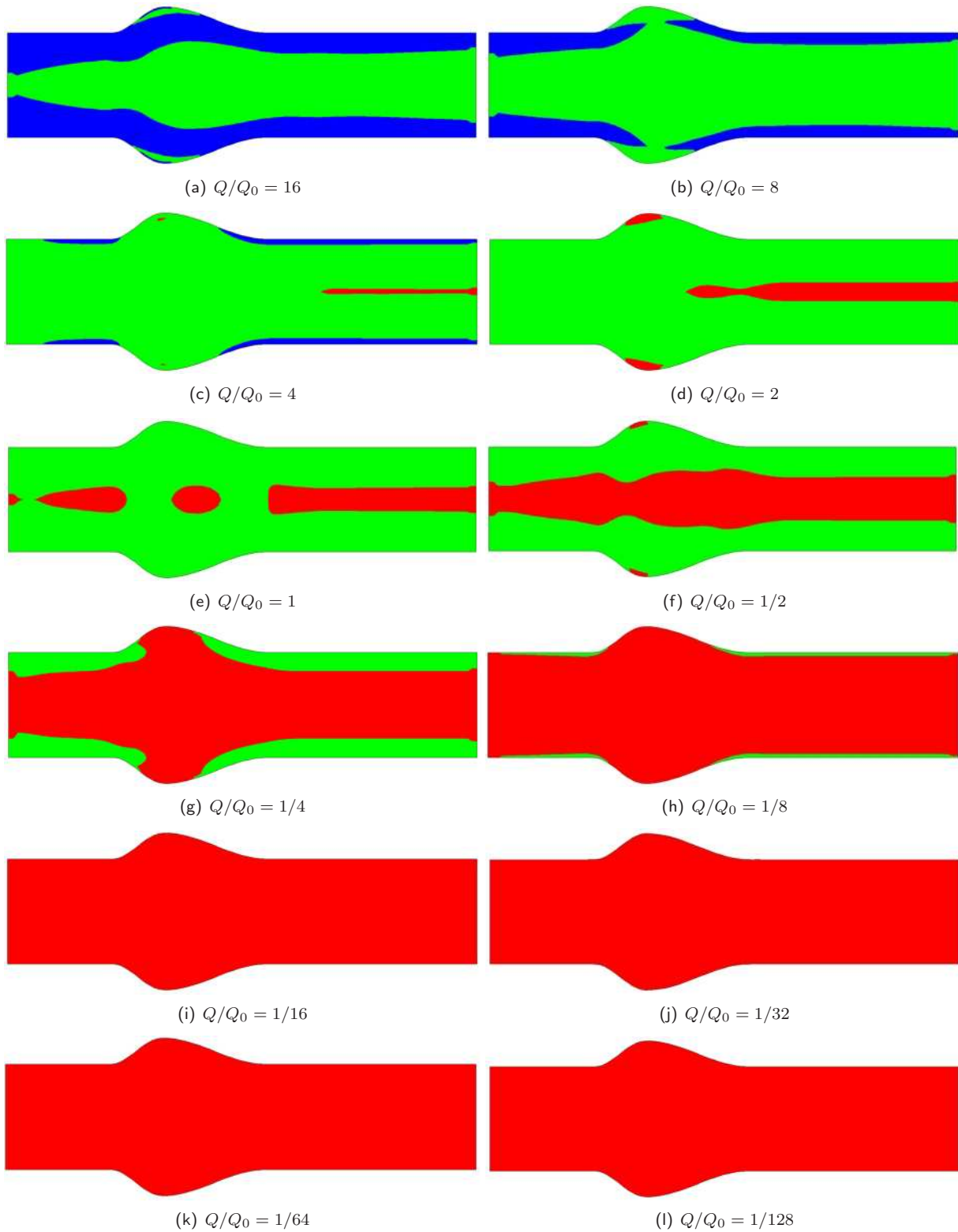# Chapter 11

Tests of Viscoelastic Models

Contents

11.1 $\mathfrak{C}_8$: Differences between Viscoelastic, Newtonian and Generalized Newtonian Fluid Flows

11.1.1   The aim of the test case

The aim of the following test case is to point out the differences between four different types of fluid flows. We compare four types of fluids: Newtonian, generalized Newtonian, viscoelastic and generalized viscoelastic. This test case is simplified to two dimensions. All together there were performed four computations[1] with different models.

11.1.2   Test case set up

The computational domain is contracting channel introduced in test case $\mathfrak{C}_3$. The diameter of the channel is $D = 2R = 6.2 \ mm$. The inlet velocity is $U = 6.15 \ cm.s^{-1}$ of parabolic profile derived in the test case $\mathfrak{C}_1$. The fluid density is $\rho = 1050 \ kg/m^3$. Solvent viscosity $\mu_s = 0.0056 \ Pa \cdot s$. Reynolds number is $Re = 100$. The test case is assumed to be laminar. The flow rate is $Q = 4 \ cm^2/s$ according to [58]. For viscoelastic fluid flows the Oldroyd B model is used. Retardation time is $\lambda = 0.06 \ s$. The Weissenberg number is $We = 0.6$. Pressure at the outlet of the domain is fixed to a constant. At the walls no-slip conditions are used for velocity and homogeneous Neumann condition for the pressure. For Oldroyd-B model variables ($\mathbf{T}_e$) the homogeneous Neumann condition is used for all boundaries. The computational mesh is of 100 x 40 x 1 cells. The table 11.1 shows four different set up variants. The first one is pure Newtonian fluid flow. The second model is generalized Newtonian shear-thinning flow, with shear-thinning viscosity model[2]. The third model is Oldroyd B with constant solvent viscosity (Newtonian fluid). The fourth model is

---

[1]solver: krysa+

[2]Modified Cross viscosity model used

(b) Newtonian model

(c) Oldroyd-B model

(d) Generalized Newtonian model

(e) Generalized Oldroyd-B model
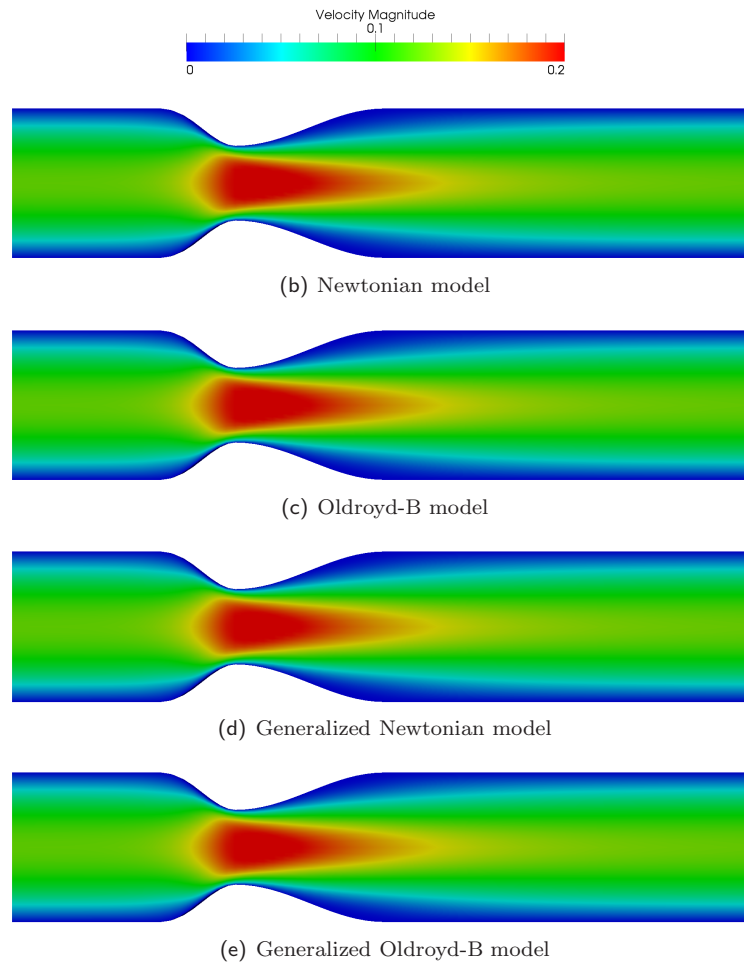
Figure 11.1: Comparison of axial velocity distribution

generalized Oldroyd-B (shear-thinning), which is Oldroyd B model with variable solvent viscosity using same model as generalized Newtonian shear-thinning fluid flow.

Model name	Shear-Thinning	Viscoelasticity	μ_s	$\mathbf{T}_e$
Newtonian	no	no	μ_∞	**0**
Generalized Newtonian	yes	no	$\mu(\dot{\gamma})$	**0**
Oldroyd-B	no	yes	μ_∞	$\mathbf{T}_e$
Generalized Oldroyd-B	yes	yes	$\mu(\dot{\gamma})$	$\mathbf{T}_e$

Table 11.1: An overview of four different models' set up

11.1.3   Test case conclusion

Set of figures 11.1 shows velocity magnitude for all described types of fluids. Set of figures 11.2 shows pressure distribution and axial velocity distribution along the central axis of the channel. The models' differences are larger in pressure distribution than in velocity distribution. For the case set up we have
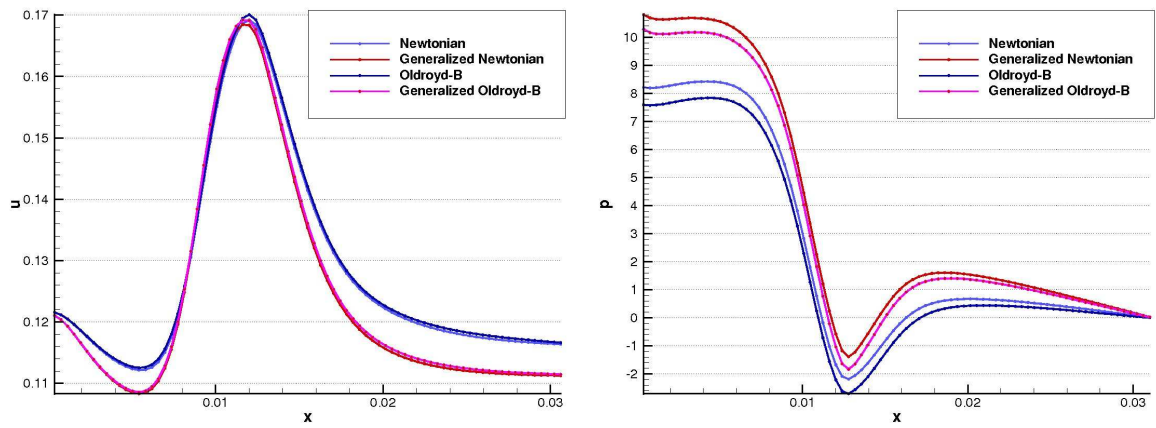
Figure 11.2: Pressure and axial velocity distribution along the centerline of the channel

used, the contribution[3] coming from shear-thinning viscosity model is much higher than contribution coming prom viscoelastic effects. One should keep in mind that the shear-thinning viscosity strongly depends on shear rate and flow rate. On the other hand viscoelasticity (generation of extra stress) depends mainly on geometry of the domain and the flow-rate. Such a comparison, that we made in this test case thus depends on the selected geometry.

---

[3]in sense of influence to fluid flow

11.2 $\mathfrak{C}_9$: Flow of Viscoelastic fluid in Periodically Contracted Channels

11.2.1 The aim of the test case

Viscoelastic fluid flow is very complicated phenomenon. An extremely important dimensionless number for viscoelastic fluid flow is *Weissenberg number*, introduced in subsection 5.2. In the following test case we have focused on computation of viscoelastic fluid flows at moderate Weissenberg number. The introduced viscoelasticity model[4] has some limitations, it works well only up to certain Weissenberg number. The aim of this test case is to explore the solution dependence on the Weissenberg number. This test case is simplified to two dimensions. We have solved this test case using Finite Volume Method.

This test case was also solved by the other independent group at the Charles University in Prague. The physical model was exactly the same, but the numerical method was completely different[5]. Both groups made their data available each other, which allowed to make a results comparison of both methods.

11.2.2 Test case set up

The following test case is assumed to be laminar. The fluid is Newtonian. There were performed lots of computations[6] finding maximal possible Weissenberg number for each geometry. The computational domain is a channel with a certain number of contractions and special slope of those contractions. The geometry of the computational domain is sketched in figure 11.3.

Figure 11.3: Computational domain geometry (image reprinted from [17])

For this test case we have selected six variants of possible geometries according to figure 11.3. The selected geometries are sketched in figure 11.4.
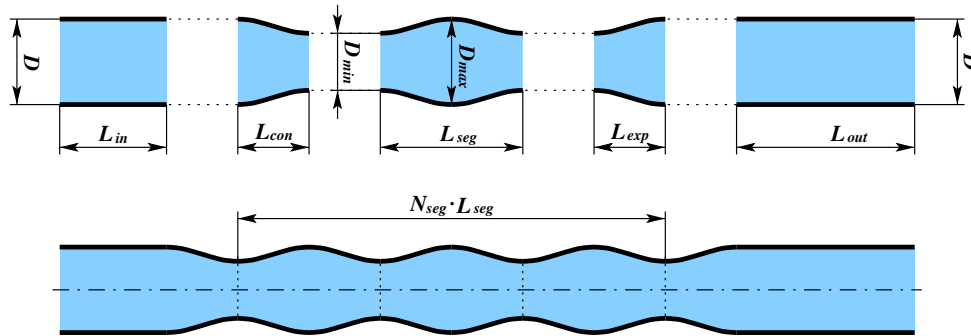
---

[4]Oldroyd B
[5]Finite Element Method
[6]solver: krysaFOAM

(a) Geometry 1, $N_{seg} = 2$, $D = 1$ cm, $L_{seg} = 2$ cm, $L_{in} = 2$ cm, $L_{out} = 5$ cm,

(b) Geometry 2, $N_{seg} = 2$, $D = 1$ cm, $L_{seg} = 4$ cm, $L_{in} = 2$ cm, $L_{out} = 5$ cm,

(c) Geometry 3, $N_{seg} = 3$, $D = 1$ cm, $L_{seg} = 2$ cm, $L_{in} = 2$ cm, $L_{out} = 5$ cm,

(d) Geometry 4, $N_{seg} = 3$, $D = 1$ cm, $L_{seg} = 4$ cm, $L_{in} = 2$ cm, $L_{out} = 5$ cm,

(e) Geometry 5, $N_{seg} = 4$, $D = 1$ cm, $L_{seg} = 2$ cm, $L_{in} = 2$ cm, $L_{out} = 5$ cm,

(f) Geometry 6, $N_{seg} = 4$, $D = 1$ cm, $L_{seg} = 4$ cm, $L_{in} = 2$ cm, $L_{out} = 5$ cm,
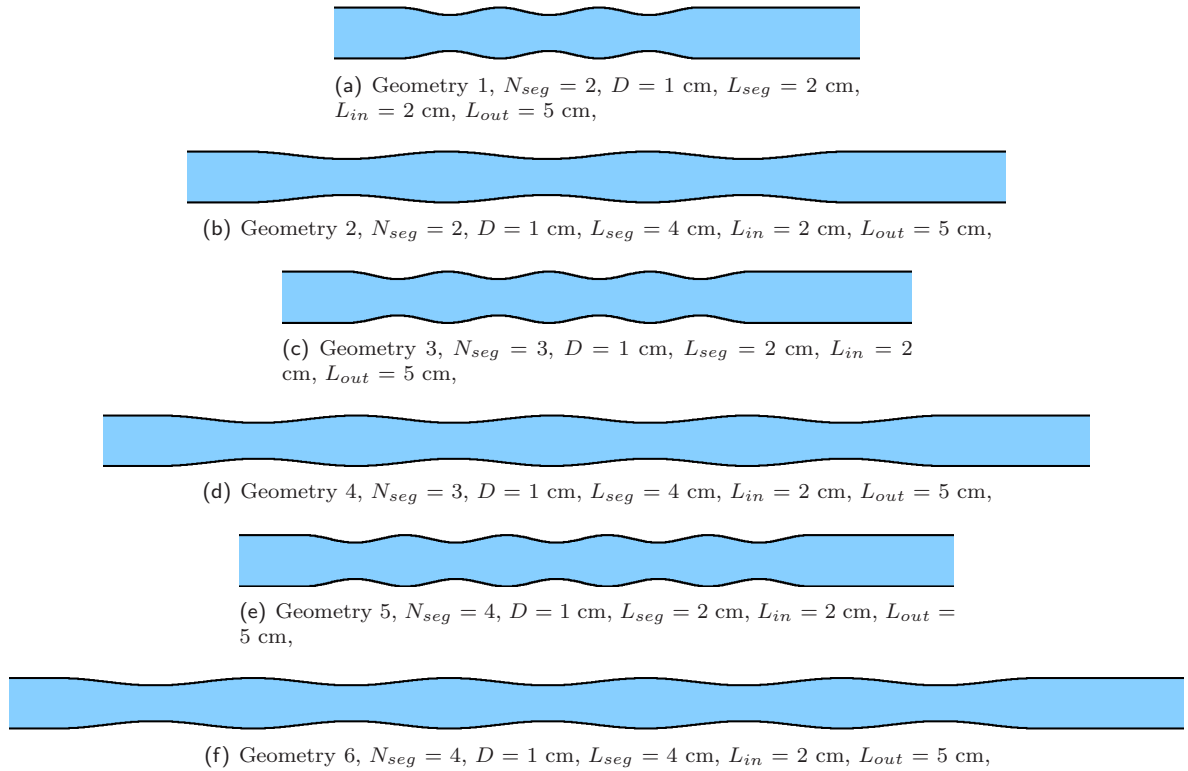
Figure 11.4: Six selected geometries

The diameter of the channel is $D = 1.0$ cm. The mean inlet velocity is $U = 10.0$ $cm.s^{-1}$ of parabolic profile derived in the test case $\mathfrak{C}_1$. The fluid density is $\rho = 1000$ kg/m^3. Solvent viscosity $\mu_s = 0.009$ $Pa \cdot s$. Extra stress viscosity $\mu_e = 0.001$ $Pa \cdot s$. The diameter of the channel and the inlet velocity always remain the same for all the test geometries. The Reynolds number is constant for all case $Re = 100$. The only variable parameter in Weissenberg number is retardation time λ. Retardation time can be interpreted as an ability of the fluid to remember the extra stress in the fluid. In other words, retardation time is a parameter that tells us, how long extra stress survives in the fluid. The computational meshes[7] are 506x36x1, 722x36x1, 578x36x1, 867x36x1, 650x36x1 and 1011x36x1 cells respectively. Both solvers have used exactly same meshes.

11.2.3   Results

Comparison of Finite Volume Method with Finite Element Method

Set of figures 11.5 shows velocity magnitude for both computational methods.

Set of figures 11.6 shows comparison of velocity magnitude along the centerline of the channel for both computational methods.

Set of figures 11.7 shows comparison of velocity magnitude along the centerline of the channel for both computational methods.

---

[7]co-author Karel Tůma

(b) Geometry 1, Velocity magnitude, Finite Volume Method

(c) Geometry 1, Velocity magnitude, Finite Element Method
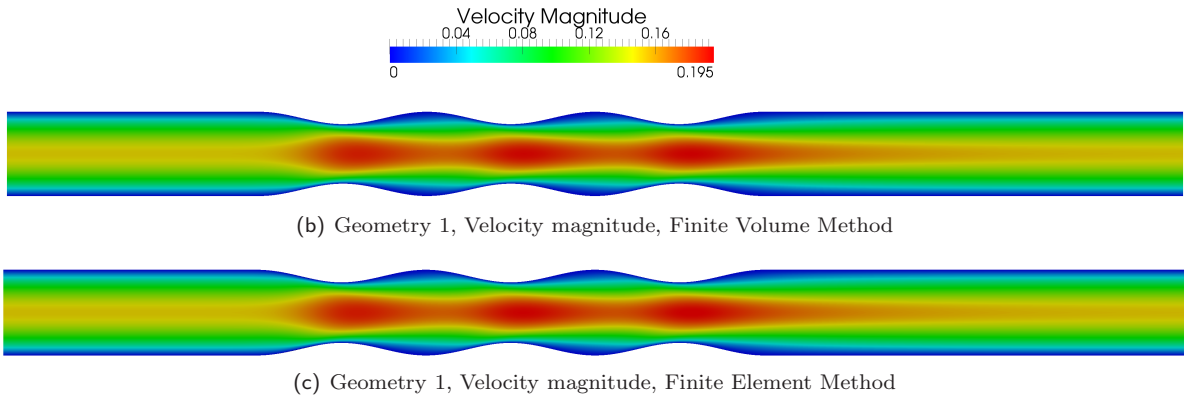
Figure 11.5: Comparison of Finite Volume Method with Finite Element Method, Geometry 1, Velocity distribution, Newtonian fluid flow ($We = 0.0$)

(a)

(b) Velocity magnitude, $We = 0.5$, Finite Volume Method

(c) Velocity magnitude, $We = 0.5$, Finite Element Method

(d) Centerline velocity comparison, $We = 0.5$
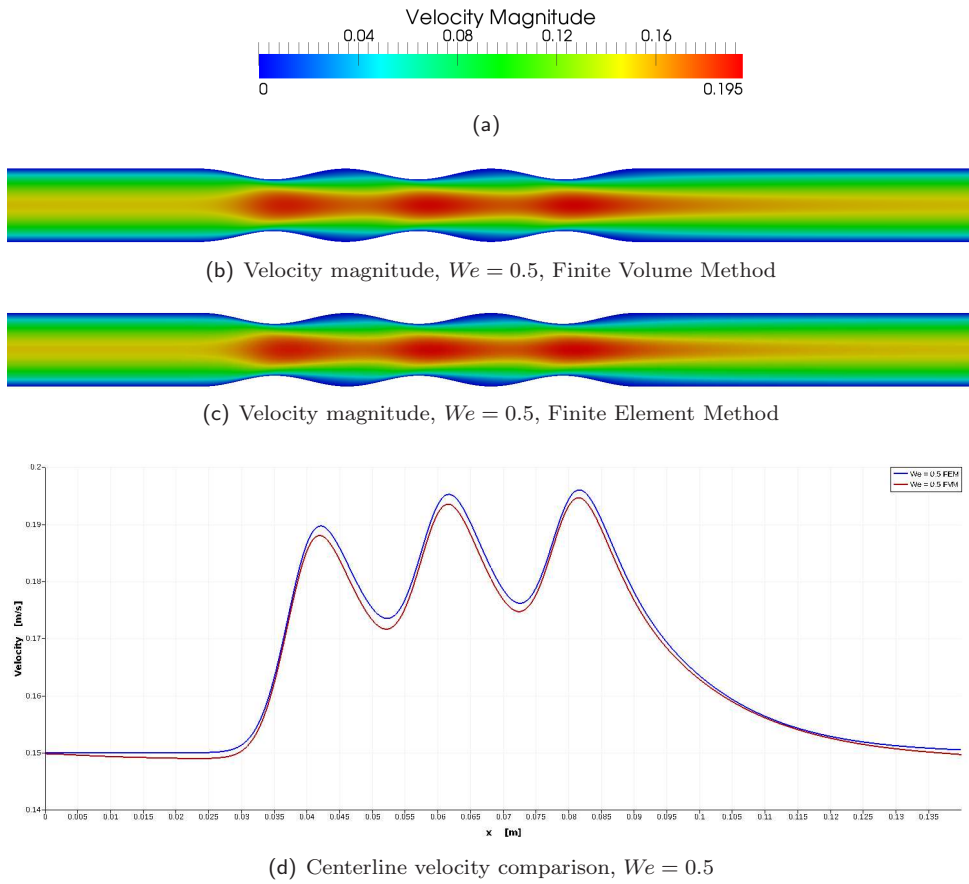
Figure 11.7: Comparison of Finite Volume Method and Finite Element Method, $We = 0.5$
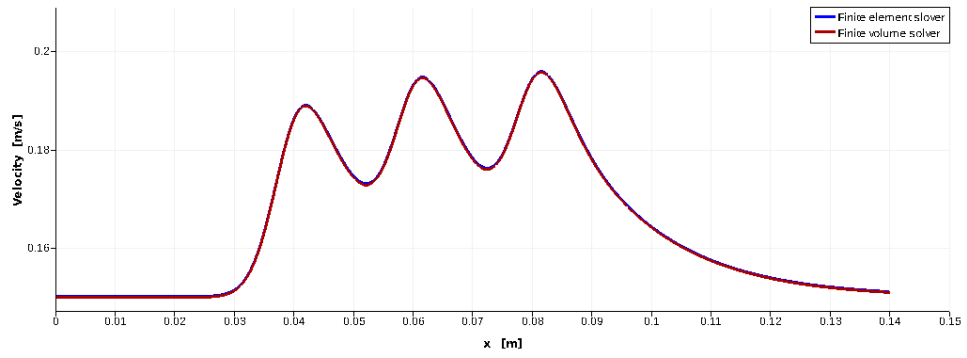
(a) Geometry 1, Centerline velocity
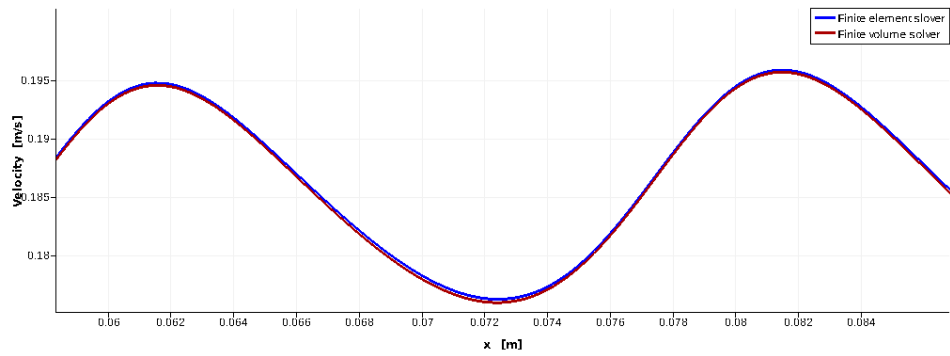
(b) Geometry 1, Centerline velocity, detail
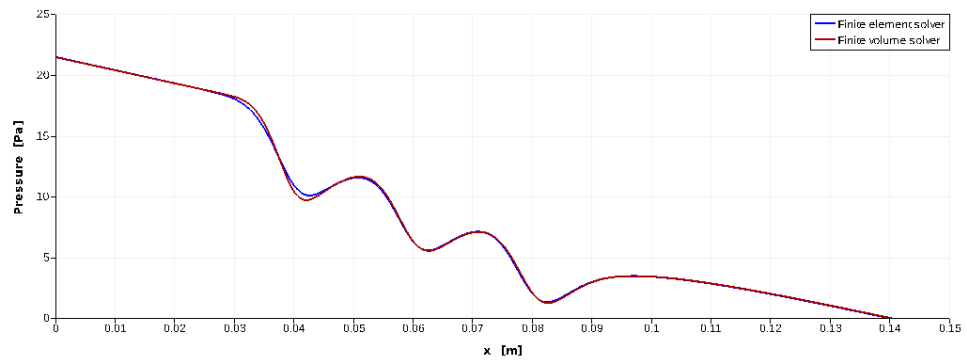
(c) Geometry 1, Centerline pressure
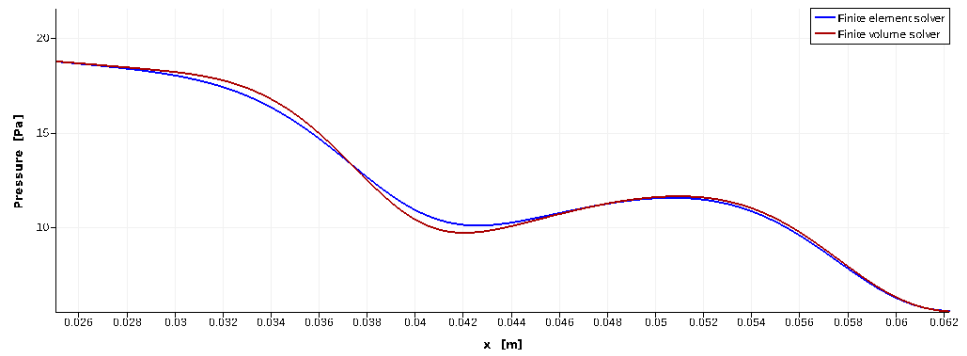
(d) Geometry 1, Centerline pressure, detail

Figure 11.6: Comparison of Finite Volume Method with Finite Element Method, pressure and velocity distribution along centerline of the channel

(b) Geometry 1, axial velocity, $We = 1.0$

(c) Geometry 2, axial velocity, $We = 1.0$

(d) Geometry 3, axial velocity, $We = 1.0$

(e) Geometry 4, axial velocity, $We = 1.0$

(f) Geometry 5, axial velocity, $We = 1.0$

(g) Geometry 6, axial velocity, $We = 1.0$
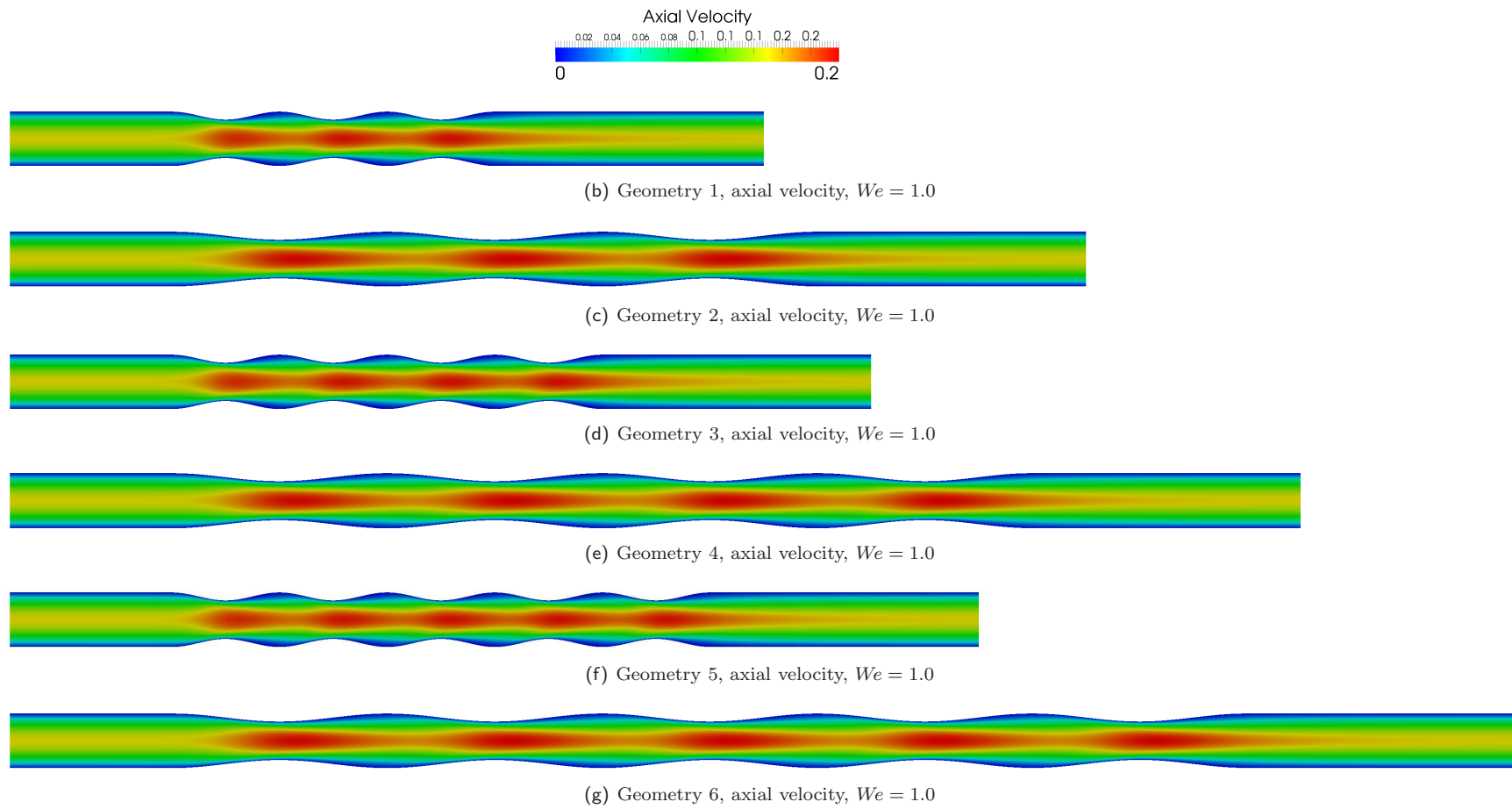
Figure 11.8: Axial velocity for all six geometries, $We = 1.0$

(b) Geometry 1, radial velocity, $We = 1.0$

(c) Geometry 2, radial velocity, $We = 1.0$

(d) Geometry 3, radial velocity, $We = 1.0$

(e) Geometry 4, radial velocity, $We = 1.0$

(f) Geometry 5, radial velocity, $We = 1.0$

(g) Geometry 6, radial velocity, $We = 1.0$
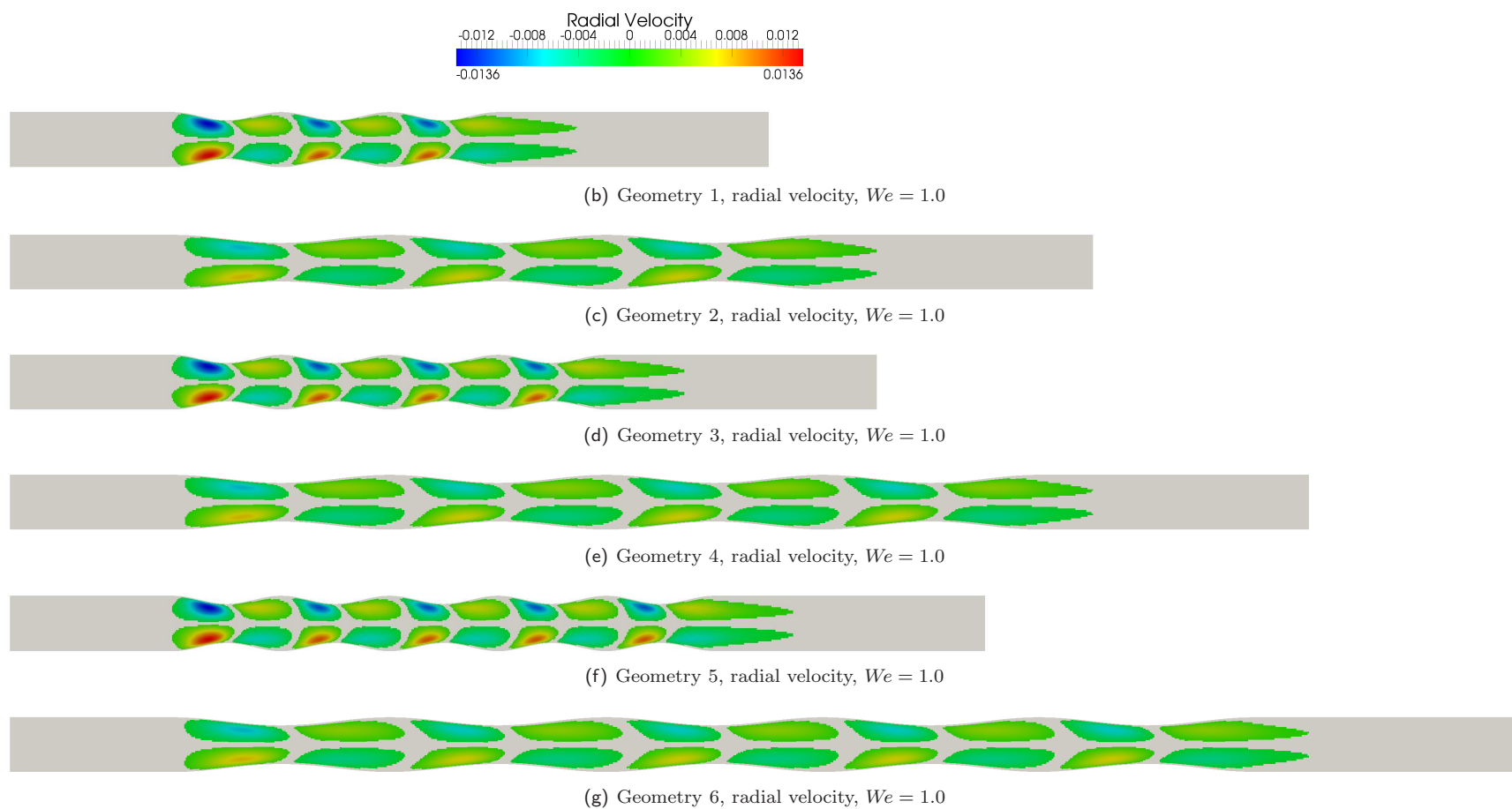
Figure 11.9: Radial velocity for all six geometries, $We = 1.0$

(b) Geometry 1, Extra stress tensor magnitude, $We = 0.1$

(c) Geometry 1, Extra stress tensor magnitude, $We = 0.5$

(d) Geometry 1, Extra stress tensor magnitude, $We = 1.0$

(e) Geometry 1, Extra stress tensor magnitude, $We = 2.0$

Figure 11.10: Comparison of extra stress tensor magnitude for increasing Weissenberg number

Extra Stress Accumulation Phenomena

The previous experiences showed that for each geometry there exists a certain maximal Weissenberg number for which the simulation crashes due to the blow-up of extra stress tensor. To find possible dependence between maximal Weissenberg number and the geometry shape there were performed a number of computations for each geometry. For each geometry the Weissenberg number was gradually increased until the computation crashed. For example geometry number one was able to handle maximal Weissenberg $We = 2.0$. The complete list of maximal Weissenberg numbers and its comparison can be found in table 11.2. These investigations showed up, that until reaching certain Weissenberg number value, the extra stress magnitude periodically the same with each contraction of the channel. After reac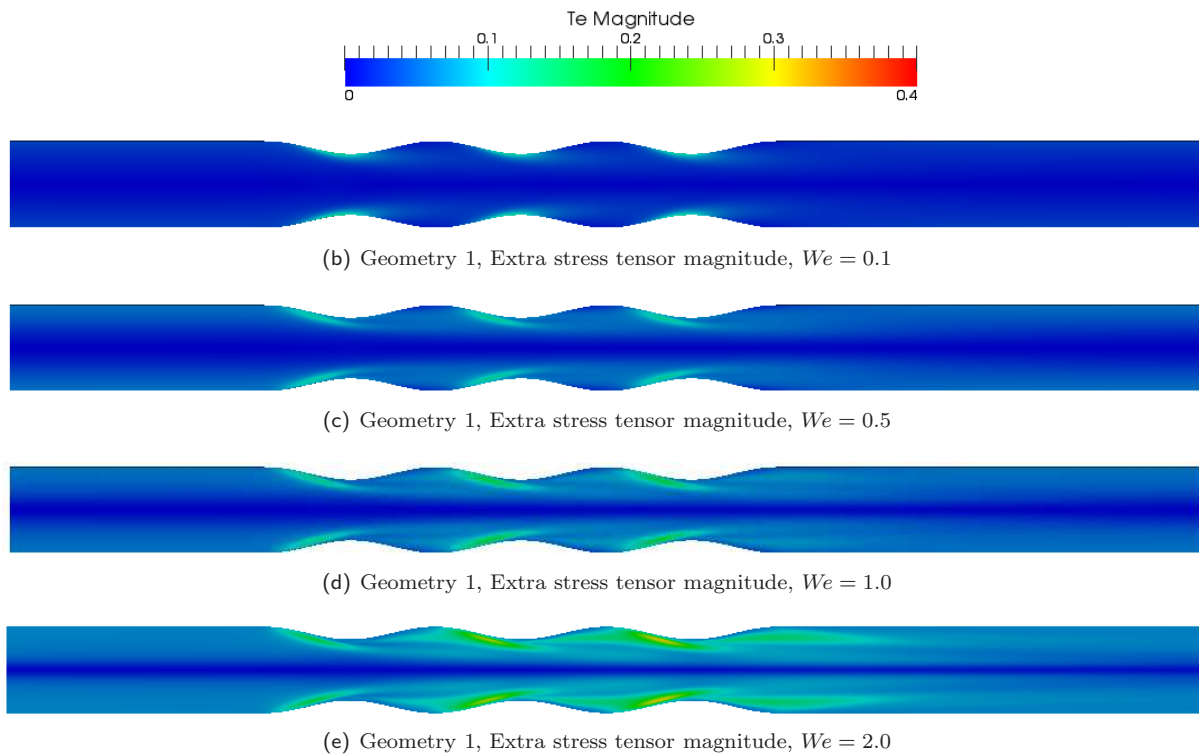hing this value the extra stress starts to accumulate with each contraction of the channel. It can be interpreted, the fluid is not able to forget the extra stress, in time that runs up while the fluid particles get from one contraction to another. This extra stress accumulation phenomena probably leads to the computation crash. The set of figures 11.10 shows extra stress tensor magnitude for moderate Weissenberg numbers. For the geometry number one the extra stress tensor is perfectly periodic up to Weissenberg number $We = 0.5$.

The set of figures 11.11 shows axial velocity, radial velocity and extra stress tensor magnitude for Weissenberg number $We = 1.0$ on the geometry number five. One can observe extra stress accumulation phenomena (maximal extra stress magnitude grows from one contraction to another).

Growth of the Maximum Velocity Phenomena

Above mentioned extra stress accumulation phenomena also causes the local increase of axial velocity. The set of figures 11.13 shows axial velocity for different Weissenberg numbers. Increasing the Weissenberg number, at certain level, suddenly the extra stress magnitude stops to be periodic and extra stress starts to accumulate. As a result of such effect, the maximal velocity slightly increases. In the set of figures 11.13 one can see the detail of this phenomena.

(a) Geometry 5, Axial velocity, $We = 1.0$

(b) Geometry 5, Radial velocity, $We = 1.0$

(c) Geometry 5, Extra stress tensor magnitude, $We = 1.0$
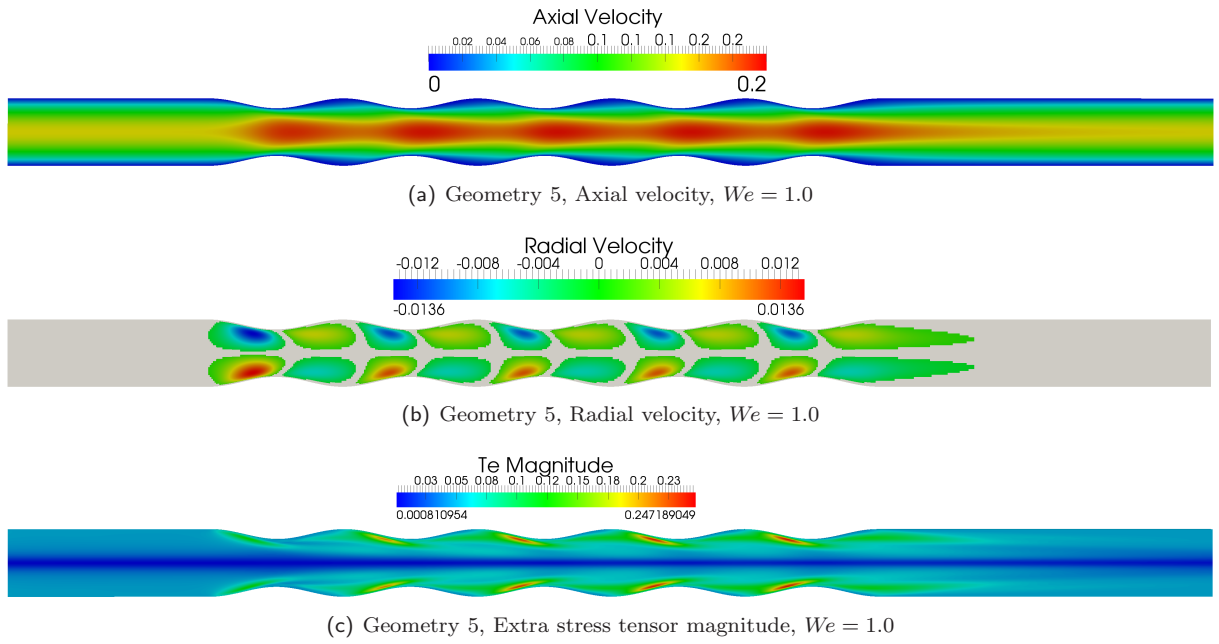
Figure 11.11: Geometry 5, $We = 1.0$

(a) Centerline velocity magnitude for different Weissenberg numbers

(b) Centerline velocity magnitude for different Weissenberg numbers, detail
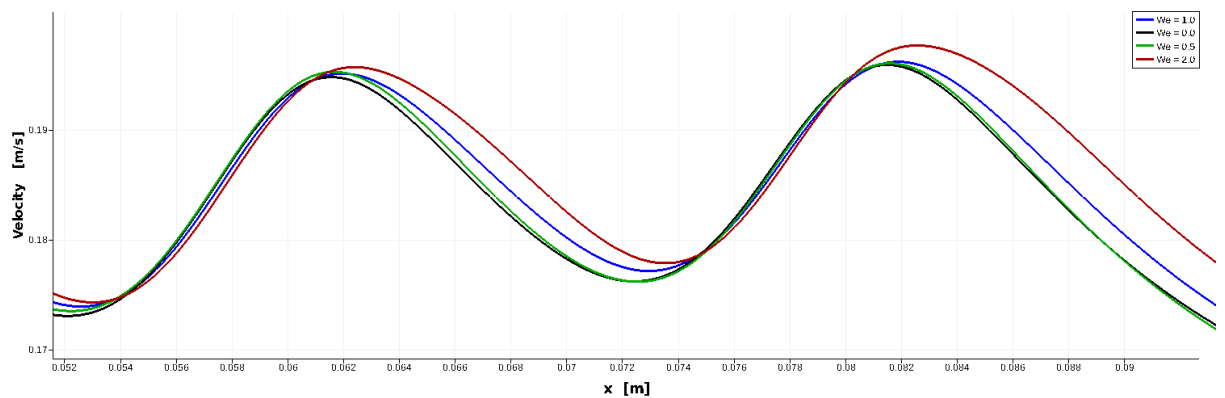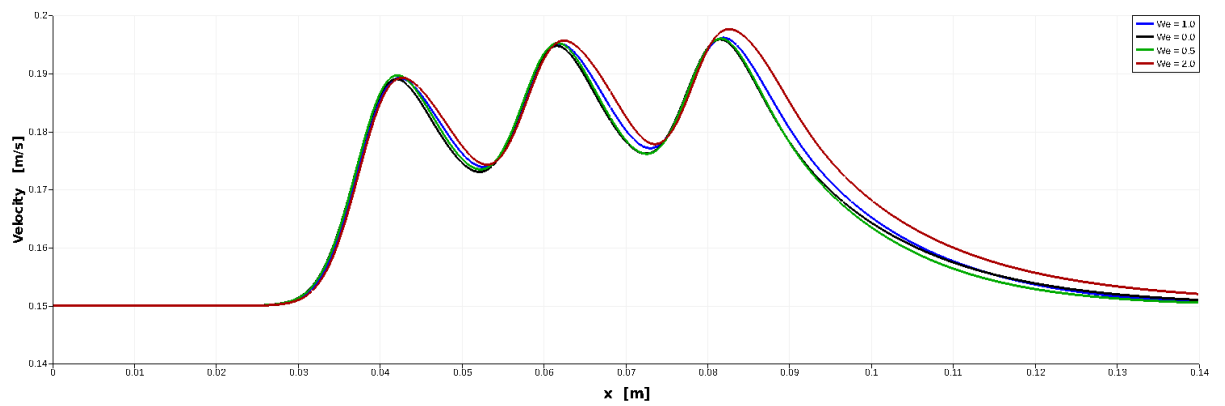
Figure 11.12: Comparison of centerline velocity magnitude for different Weissenberg numbers
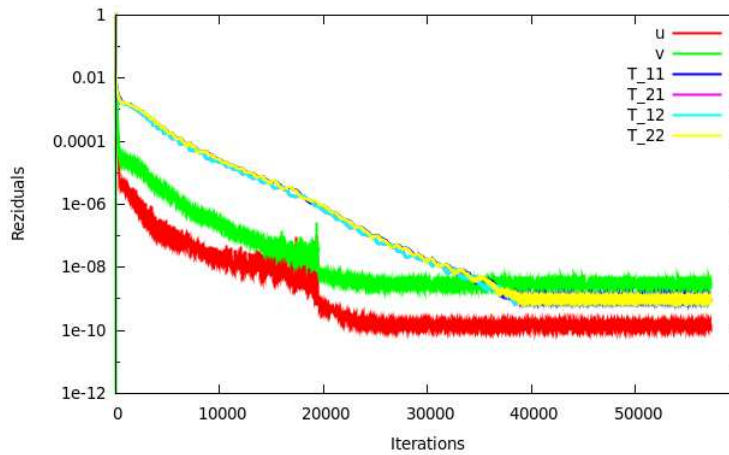
Figure 11.13: Residual history for geometry number one, $We = 0.5$, u and v are velocity components, T_11, T_21, T_12 and T_22 are components of extra stress tensor

11.2.4   Test case conclusion

The conclusion number one is following: The geometries with longer segments can handle higher maximal Weissenberg number, which was confirmed by both solvers[8]. The reason is the fluid has more physical time to relax until it reaches another contraction.

The conclusion number two is following: With increasing number of segments the maximal Weissenberg number decreases due to the extra stress accumulation phenomena, which was also confirmed by both solvers.

The table 11.2 shows maximal Weissenberg numbers for each geometry for both solvers (krysaFOAM and FEM).

Geometry #	N_{seg}	L_{seg} [cm]	We_{max} (FEM)	We_{max} (FVM - krysaFOAM)
1	2	2	4.0	2.0
2	2	4	5.5	4.0
3	3	2	3.5	1.5
4	3	4	5.5	3.0
5	4	2	3.0	1.0
6	4	4	5.5	2.0

Table 11.2: Comparison of maximal Weissenberg numbers for both solvers for all test geometries

The FEM solver can reach higher Weissenberg numbers than solver krysaFOAM in all tested cases. The reason is the use of different numerical stabilization (the FEM solver has ability of strong numerical stabilization).

---

[8]krysaFOAM (Finite Volume method solver) and FEM (Finite Element Method solver, Charles University)

Chapter 12

Application to Blood Coagulation Model

Contents

12.1 $\mathfrak{C}_{10}$: Blood Coagulation Test Case

12.1.1   The aim of the test case

The aim of th following test case is to test the state-of-art blood coagulation model introduced in chapter 6. The model was designed by prof. K. Rajakopal and is still in an experimental phase of development.

12.1.2   Test case set up

The test case is three dimensional. This is pure unsteady test case[1]. The physical time is set $T = 5000\ s$. The computational domain of the test case is a tube, to imitate an idealized blood vessel. The test case is three dimensional. Figure 12.1.2 shows a sketch of the computational domain (a cut along tube axis).
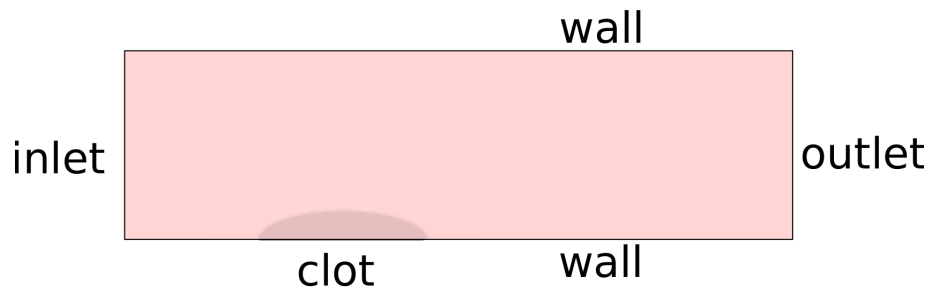
Figure 12.1: Test case geometry, axis cut

---

[1]solver: krysaFOAM

The computational geometry in three dimensions is shown in figure 12.2. The computational mesh is unstructured[2]. It is made of hexahedrals in blocks and is of 25 000 cells.

(a)   inlet/outlet view   (b) side view

(c) 3d channel
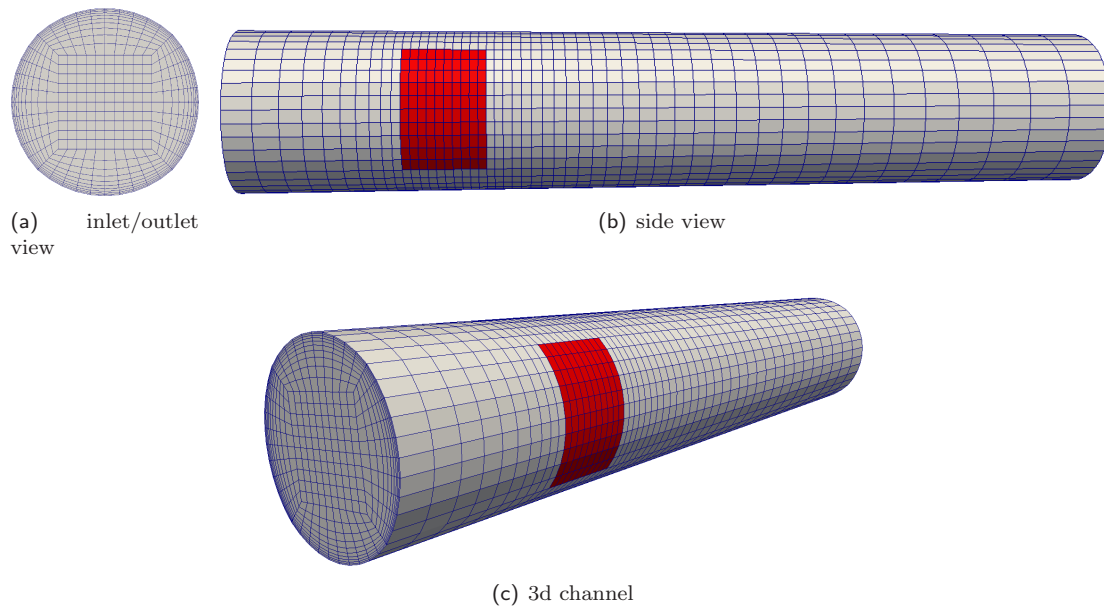
Figure 12.2: 3d tube, rectangular zone at the wall indicates the clot surface

The clot surface at the tube boundary is indicated in the figure 12.2. It is a rectangular part of the tube wall, asymmetrically placed closer to the inlet of the domain. Boundary conditions are following: Five of twenty eight chemical constituents C_i have a special treatment, at the clot surface, the time dependent non-homogenous Neumann boundary conditions are applied: $\partial C_i / \partial n = f(C_i, t)$. For the rest of constituents homogeneous Neumann ($\partial C_i / \partial n = 0$) is applied everywhere on the wall. Velocity U is zero at the walls and constant at the inlet. Pressure p is kept constant at the outlet of the domain. The diameter of the tube is one centimeter, the length of the tube is 5.5 cm. The mean inlet velocity is 10 cm/s. The density of flowing blood is 1060 $kg/m3$. Dynamic viscosity is $\mu = 0.0056 \ Pa \cdot s$. Reynolds number of the case is $Re = 190$. The test case is assumed to be laminar.
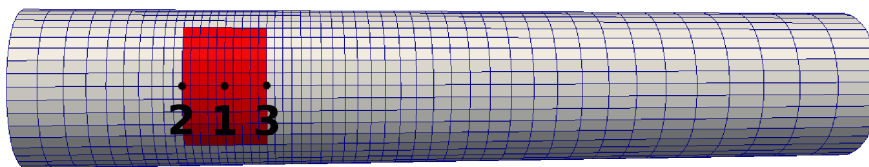
Figure 12.3: indication of three selected points

12.1.3   Test case conclusion

Set of figures 12.4 shows time development of selected concentrations in three selected points of the geometry. All three points are placed on the clotting surface according to figure 12.3. The growth and lysis of the clot were clearly observed. Set of figures 12.6 shows time development of velocity magnitude.

---

[2]created in blockMesh, part of OpenFOAM, co-author Daniel LaCroix
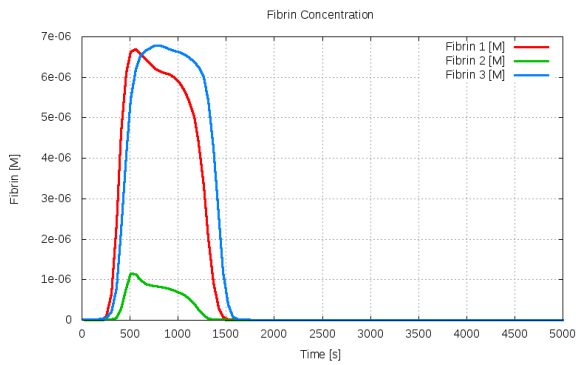
(a) Fibrin concentration time development
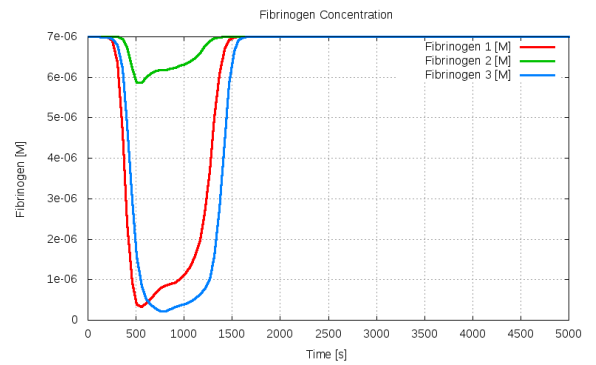
(b) Fibrinogen concentration time development
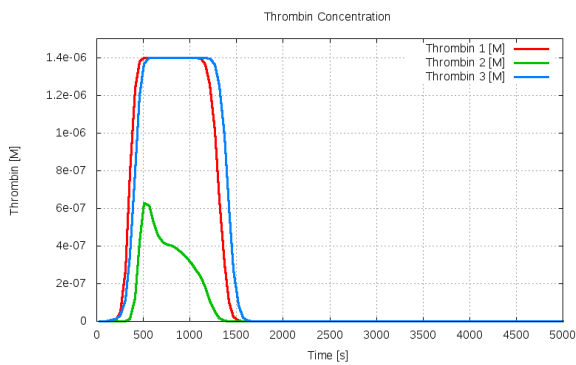
(c) Thrombin concentration time development
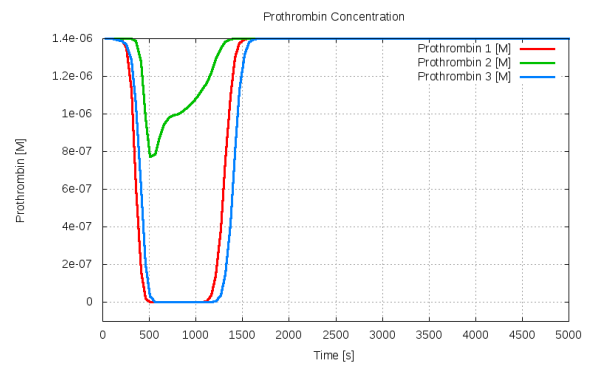
(d) Prothrombin concentration time development

Figure 12.4: Selected concentrations at three selected points, 1 - geometrical center of the clot, 2 - point in the middle of leading edge of the clot, 3 - point at the end of the clot, all three points are in one single line
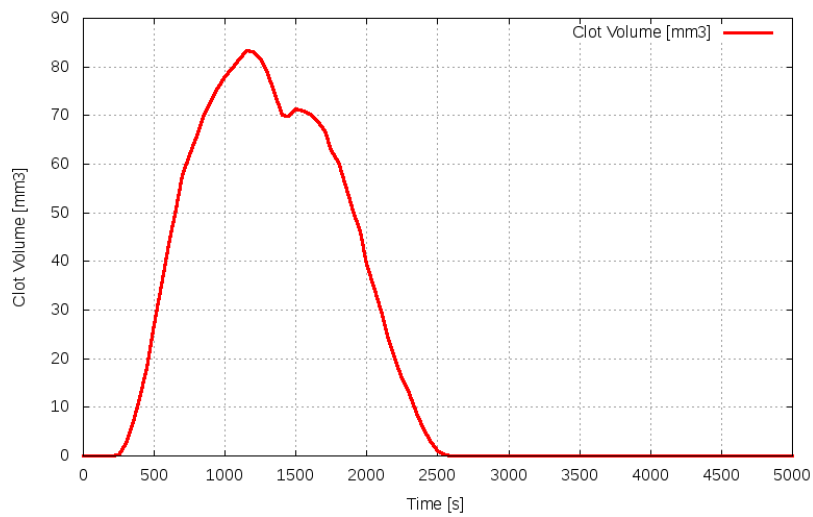
Figure 12.5: Time evolution of the clot volume in mm^3
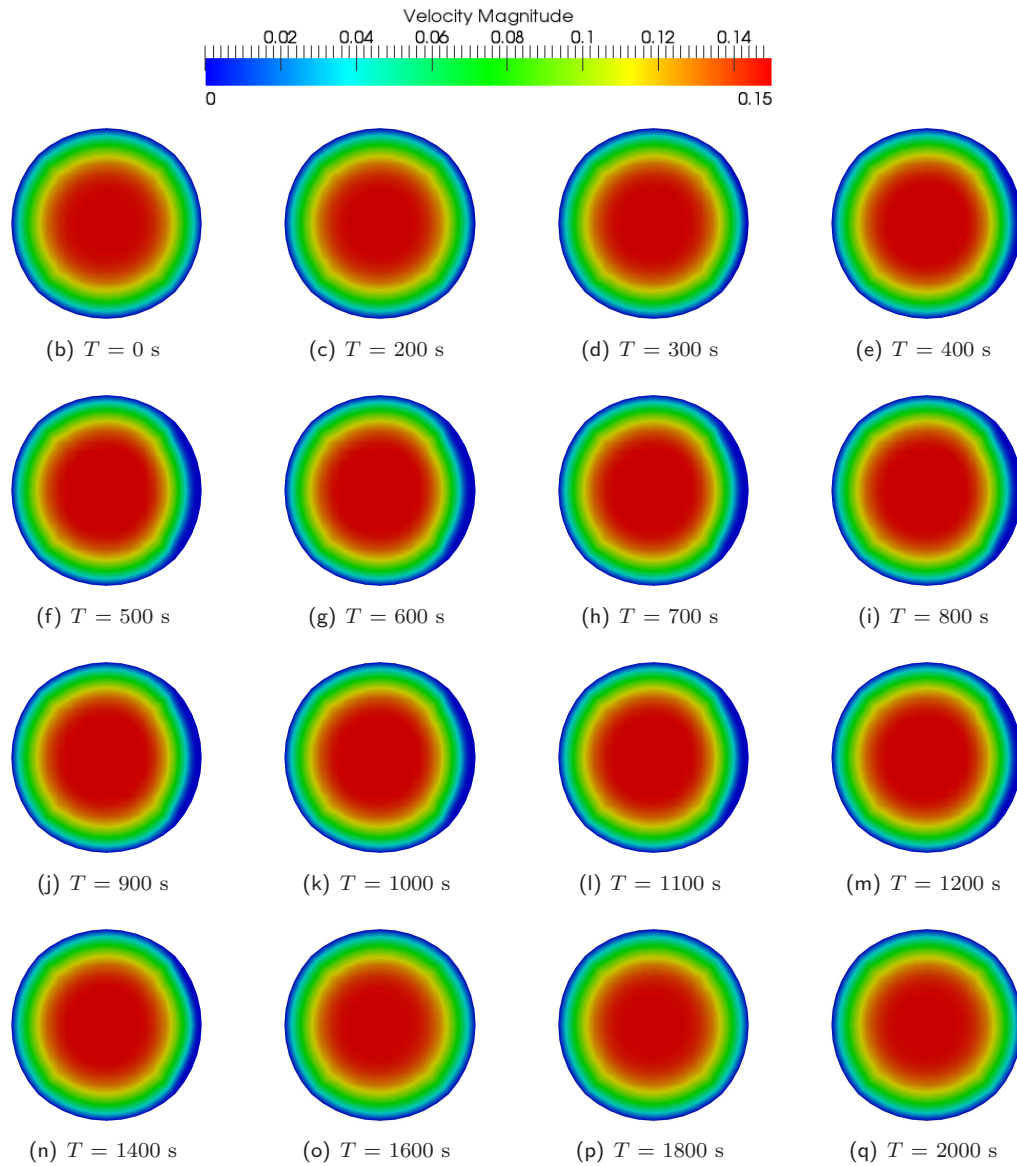
Figure 12.6: Time development of velocity magnitude in cross-section at point 1

On the right hand side of intersections one can observe the velocity decreases, which clearly indicates the existence of the clot. Figure 12.5 shows the time development of the size of the clot. The maximal clot size is at time $t = 1200\ s$ and disappears at time $t = 2600\ s$, both times have good agreement with [4]. The model is still in experimental stage of development.

Chapter 13

Conclusion & Remarks

This work is final result of nearly seven years of the studies of applied mathematics at The Faculty of Mechanical Engineering (Department of Technical Mathematics) at The Czech Technical University. The work was written with afford to be understandable, even if a numerical solution of fluid flow is relatively complicated phenomenon. Particular conclusions are mentioned in special section in each of ten test cases. We have showed, that over a number of simplifications, the introduced models can be used. The presented work has demonstrated:

1. The way of numerical solution of Navier-Stokes equations using Finite Volume Method.

2. Physical and mathematical basics of solving problems of incompressible, viscous, Newtonian, generalized Newtonian and viscoelastic fluid flow.

3. The state-of-art blood coagulation model was described and tested (test case $\mathfrak{C}_{10}$).

4. The original Finite Volume Method solver (in-house code) was created. The in-house code can solve incompressible, viscous, Newtonian, generalized Newtonian and viscoelastic fluid flow. In addition an open-source code was modified to solve all the described models, including state-of-art blood coagulat ion model.

5. Numerical results' agreement with analytical solution and another solver using different numerical approach (test cases $\mathfrak{C}_1, \mathfrak{C}_2, \mathfrak{C}_3$ and $\mathfrak{C}_9$).

6. The comparison of generalized Newtonian viscosity models (test case $\mathfrak{C}_5$). All the implemented generalized Newtonian viscosity models give approximately identical results and show good applicability. In another case was shown the possible way to find reference Newtonian viscosity for generalized Newtonian fluid (test case $\mathfrak{C}_6$) and the generalized Newtonian viscosity dependence on flow-rate (test case $\mathfrak{C}_7$). In another case was investigated the difference between Newtonian and generalized Newtonian type of flow (test case $\mathfrak{C}_4$). We have shown the differences in velocity distribution in both cases. These comparisons prove that generalized Newtonian behavior of fluid shouldn't be left out if apparently exists. In another case were shown differences among Newtonian, generalized Newtonian and viscoelastic fluid flow (test case $\mathfrak{C}_8$).

Future plans

- To compare introduced models with relevant experimental data

- To test the time dependent behavior of viscoelastic models

- To incorporate and test another non-Newtonian fluid models

- To find a robust model best describing blood flow

Technical details

All the presented results are displayed in *Tecplot 10.0*, *ParaView* and *Gnuplot*. All the meshes were generated using home made *C++* code, *Tecplot 10.0*, *blockMesh*(part of OpenFOAM). The pictures are made in *Adobe Illustrator CE 10.0* and in *Inkscape*. The work itself was typeset by LATEX in application *Kile*.

After defending of this work author is ready to release to anyone the source code of the solver or any part of this project on request. Eventual questions or reminders please send to: *Lubos.Pirkl@seznam.cz.*

References

A

[1] Acheson D.J., *Elementary Fluid Dynamics,* Oxford Applied Matematics and Computing Science Series, (1990).

[2] Almeida, G.P., Durao, D.F.G. ,Heitor, M.V., *Wake flows behind two dimensional model hills.* Exp. Thermal and Fluid Science, 7, p.87, (1992).

[3] Anand M., Rajagopal K., Rajagopal K.R. *A model incorporating some of the mechanical and bio-chemical factors underlying clot formation and dissolution in flowing blood.* J. of Theoretical Medicine, 5 (3-4):183-218, (2003).

[4] Anand M., Rajagopal K., Rajagopal K.R. *A model for the formation, growth, and lysis of clots in quiescent plasma, a comparison between the effects of antithrombin III deficiency and protein C deficiency.* J. of Theoretical Biology, 253:725-738, (2008).

[5] Anand M., Rajagopal K. R., *A shear-thinning viscoelastic fluid model for describing the flow of blood,* International Journal of Cardiovascular Medicine and Science, 4 (2) 59-68, (2004)

[6] Armaly B.F., Durst F., Pereira J. C. F., Schonung B., *Experimental and theoretical investigation of backward-facing step flow.* J. Fluid Mech., Sv. 127: (1983)

[7] Arsac A., Carrot C., Guillet J., Revenu P., *Problems originating from the use of the Gordon-Schowalter derivative in the Johnson-Segalman and related models in various shear flow situations* Journal of non-newtonian fluid mechanics, ISSN 0377-0257 (1994)

[8] Ataullakhanov F., Zarnitsina V., Pokhilko A., Lobanov A., Morozova O. *Spatio-temporal dynamics of blood coagulation and pattern formation. A theoretical approach.* Int. J. Bifur. Chaos 12(9) (2002)

B

[9] Bailyk P. D., Steinman D. A., Ethier C. R. *Simulation of non-Newtonian blood flow in an end-to-side anastomosis* , Biorheology 31 (5) (1994) 565-586.

[10] Berger S. A., Jou L. D.: *Flows in stenotic vessels* Ann. Rev. Fluid Mech., 347-382, 2000

[11] Bird R. B., Armstrong R. C., Hassager O. *Dynamics of Polymeric Liquids, 2nd Edition*, Vol. 1, John Willey & Sons, 1987.

[12] Bodnár T., *Numerical Simulation of Flows and Pollution Dispersion in Atmospheric Boundary Layer* CTU Thesis, 2003

[13] Bodnár T., Sequeira A., Pirkl, L. *Numerical Simulations of Blood Flow in a Stenosed Vessel under Different Flow Rates using a Generalized Oldroyd - B Model* In: Numerical Analysis and Applied Mathematics, Vols 1 and 2. Melville, New York: American Institute of Physics, 2009, vol. 2, p. 645-648. ISBN 978-0-7354-0709-1.

[14] Bodnár T., A. Sequeira *Shear-thinning effects of blood flow past a formed clot*, WSEAS Transactions on Fluid Mechanics 1 (3) (2006) 207-214.

[15] Bodnár T., A. Sequeira *Numerical simulation of the coagulation dynamics of blood*, Computational and Mathematical Methods in Medicine 9 (2) (2008) 83-104.

[16] Bodnár T., A. Sequeira *Numerical study of the significance of the non-newtonian nature of blood in steady flow through a stenosed vessel*, In: Advances in Mathematical Fluid Mechanics, Springer - Verlag, 2009, in press.

[17] Bodnár T , *High-Weisenberg Number Simulations*, unpublished paper, 2011.

[18] Bodnár T., A. Sequeira, *WSEAS Transactions on Fluid Mechanics 1*, 207-214 (2006).

[19] Bodnár T., A. Sequeira *Numerical Study of the Significance of the Non-Newtonian Nature of Blood in Steady Flow Through a Stenosed Vessel* In: Advances in Mathematical Fluid Mechanics (edited by R. RANNACHER & A. SEQUEIRA), (pp. 83-104). Springer Verlag (2010)

[20] Butcher J. C. *Numerical Methods for Ordinary Differential Equations*, John Wiley & Sons, ISBN 0-471-96758-0, 2003

[21] Butenas S., Mann K. G. *Blood coagulation*, Biochemistry (Moscow) 67(1) (2002)

C

[22] Caro C. G., T. J. Pedley, R. C. Schroter, W. A. Seed, *The Mechanics of the Circulation*, Oxford University Press, 1978.

[23] Chen J., and X.-Y. Lu, *Journal of Biomechanics 37*, 1899-1911 (2004).

[24] Chen J., and X.-Y. Lu, *Journal of Biomechanics 39*, 818-832 (2006).

[25] Chen J., X. Lu, *Numerical investigation of the non-Newtonian pulsatile blood flow in a bifurcation model with a non-planar branch*, Journal of Biomechanics 39 (2006) 818-832.

[26] Cheng D. C-H., Heywood N.I., *Flow in Pipes, Physical Technology,* Northern Ireland, 1984.

[27] Chien S., S. Usami, R. J. Dellenback, M. I. Gregersen, *Blood viscosity: Influence of erythrocyte aggregation*, Science 157(3790) (1967) 829-831.

[28] Chien S., King R. G., Skalak R., Usami S., Copley A. L. *Viscoelastic properties of human blood and red cell suspensions*, Biorheology, 12:341-346, 1975.

[29] Chmiel H., Anadere I., Walitza E. *The determination of blood viscoelasticity in clinical hemorheology*, Biorheology, 27:883-894, 1990.

[30] Cho Y.I., Kensey K.R., *Effects of Non-Newtonian Viscosity of Blood on Flows in Diseased Arterial Vessel*, Part 1: Steady Flows, vol.28 (1991), pp. 41-262.

D

[31] Davis T. A. *Algorithm 832: UMFPACK V4.3—an unsymmetric-pattern multifrontal method,* J. ACM Trans. Math. Softw., 2004

[32] Dintenfass L., *Blood Viscosity,* MTP Press Limited, 1985 , ISBN 0-85200-413-3

[33] Dormand J. C., *Numerical Methods for Differential Equations - A Computational Approach*, JRC Press, 1996.

F

[34] Fahraeus R., Lindqvist T. *The viscosity of the blood in narrow capillary tubes*, Am. J. Physiol., 96:562-568, 1931.

[35] Feistauer M. , J. Felcman, I. Strasškraba *Mathematical and Computational Methods for Compressible Flow*, Oxford University Press, USA (September 11, 2003).

[36] Fürst J., *Numerické řešení transonického proudění užitím TVD a ENO schḿat* , Disertační práce, 2000

[37] Fogelson A. L. *Continuum models of platelet aggregation: Formulation and mechanical properties* SIAM J. Appl. Math. 52, 1992

[38] Fořt J., Fürst J., Kozel K., Louda P., *Numerické metody řešení problému proudení I., II., III.* Vydavatelství CVUT, 2001 - 2004.

G

[39] Galdi G. P., - Rannacher R. , A. M. Robertson, S. Turek, *Hemodynamical Flows - Modeling, Analysis and Simulation*, vol. 37 of Oberwolfach Seminars, Birkäuser, 2008.

[40] Gijsen F. , F. van de Vosse, J. Janssen, *The influence of the non-Newtonian properties of blood on the flow in large arteries: steady flow in a carotid bifurcation model*, Journal of Biomechanics 32 (1999) 601-608.

H

[41] Hirsh C., *Numerical Computation of INTERNAL and EXTERNAL FLOWS Volume 2 Computational Methods for Inviscit and Viscous Flows* WILEY, 1990

[42] Hron J. *Fluid structure interaction with applications in biomechanics*, Charles University, Prague, 2001

[43] Hron J., Kratochvíl J., Málek J., Rajagopal K.R., Tůma K., *A thermodynamically compatible rate type fluid to describe the response of asphalt*, Mathematics and Computers in Simulation, Elsevier, 2011

[44] Hughes W.F., Brighton J.A., *Fluid Dynamics*, Schaum 1991

[45] Huilgol R.R., Phan-Thien N., *Fluid Mechanics of Viscoelasticity*, ELSEVIER SCIENCE B.V., 1997 , ISBN 0-444-82661-0

J

[46] Jameson A. , W. Schmidt, E. Turkel, *Numerical solutions of the Euler equations by finite volume methods using Runge-Kutta time-stepping schemes*, in: AIAA 14th Fluid and Plasma Dynamic Conference, Palo Alto, 1981, aIAA paper 81-1259.

[47] Jameson A. , *Time dependent calculations using multigrid, with applications to unsteady flows past airfoils and wings*, in: AIAA 10th Computational Fluid Dynamics Conference, Honolulu, 1991, aIAA Paper 91-1596.

[48] Janzen J., T. G. Elliott, C. J. Carter, and D. E. Brooks, *Biorheology 37*, 225-237 (2000).

[49] Joseph D., *Fluid Dynamics of Viscoelasic Liquids*, vol. 84 of Applied Mathematical Sciences, Springer-Verlag, 1990.

K

[50] Karner G. , K. Perktold, M. Hofer, D. Liepsch, *Flow characteristic in anatomically realistic complian carotid artery bifurcation model*, Computer Methods in Biomechanics and Biomechanical Engineering 2 (1999) 171-185.

[51] Kim H. G., Lee C. M., Lim H. C., Kyong N. H., *An experimental and numerical study on the flow over two-dimensional hills.* Journal of Wind Engineering and Industrial Aerodynamics, vol. 66, no. 1:(1997) pp. 17-33.

[52] Kozel K., Louda P., Bodnár T., Beneš L., Sládek I., *Numerická simulace proudění II*

[53] Kozel K., Dvořák R., *Matematické modelovaní v aerodynamice* Vydavatelství ČVUT, 1996.

[54] Kuharsky A. L., Fogelson A. L., *Surface-mediated control of blood coagulation: The role of binding site densities and platelet deposition* Biophys. J. 80, 2001

L

[55] LaCroix, E.D. *A Model For Blood Coagulation And Lysis Utilizing The Intristic And Extristic Pathways* , 2011.

[56] Lakes R., *Viscoelastic Materials,* Cambridge University Press, 2009 , ISBN 978-0-521-88568-3

[57] Latif M. Jiji : *Heat Convection,* Springer, Berlin, Heidelberg, NewYork, 2006.

[58] Leuprecht A. , K. Perktold *Computer methods in Biomechanics and Biomechanical Engineering 4*, 149 - 163 (2001).

[59] LeVeque R. J., *Numerical Methods for Conservation Laws* Birkhauser Verlag, 1990

[60] Lowe D.: *Clinical blood rheology.* , Vol I. II., CRC Press, Boca Raton, Florida 1998

M

[61] Mann K., Brummel-Ziedins K., Orfeo T., Butenas S., *Models of blood coagulation,* Blood cells, Mol. Dis. 36 (2006).

[62] Meyers, Chawla, *Mechanical Behavior of Materials, 98-103,* 1999.

[63] Michaelis L. , M.L. Menten., *Die kinetik der invertinwirkung.* Biochem Z., 49:333-369, 1913.

O

[64] Oldroyd J. G., *Non-Newtonian Effects in Steady Motion of Some Idealized Elastico-Viscous Liquids* Proc. R. Soc. Lond. A June 3, 1958 245:278-297; doi:10.1098/rspa.1958.0083, (1958)

[65] OpenFOAM User Guide, OpenCFD ltd. 2004-2011.

[66] OpenFOAM Programmers Guide, OpenCFD ltd. 2004-2011.

P

[67] Pedrizzetti G., Perktold K., *Cardiovascular Fluid Mechanics,* Courses and Lectures - No.446

[68] Petkova S., Hossain A., Naser J., Palombo E., *CFD Modelling of blood in portal Vein Hypertension with and Without Thrombosis,* CSIRO, Melbourne, Australia,2003.

[69] Phan-Thien N., *Understanding Viscoelasticity,* Springer-Verlag Berlin, 2002 , ISBN 3-540-43395-3

Q

[70] Quarteroni A. , F. Saleri, A. Veneziani, *Factorization methods for the numerical approximation of the Navier-Stokes equations* , Computer Methods in Applied Mechanics and Engineering 188 (2000) 505-526.

R

[71] Rajagopal K., A. Srinivasa, *A thermodynamic frame work for rate type fluid models*, Journal of Non-Newtonian Fluid Mechanics 80 (2000) 207-227.

[72] Renardy Y.Y., *Spurt and Instability in a Two-Layer Johnson-Segalman Liquid* , Theoret. Comput. Fluid Dynamics, 7:463-475, (1995)

[73] Robertson A. M., A. Sequeira, M. V. Kameneva, *Hemorheology*, in: G. Galdi, R. Rannacher, A. M. Robertson, S. Turek (Eds.), Hemodynamical Flows: Modeling, Analysis and Simulation (Oberwolfach Seminars), Vol. 37, Birkhuser Verlag, 2008, pp. 63-120.

[74] Robertson A. M., A. Sequeira, R. G. Owens, *Rheological models for blood*, in: L. Formaggia, A. Quarteroni, A. Veneziani (Eds.), Cardiovascular Mathematics. Modeling and simulation of the circulatory system (Modeling, Simulations & Applications, Vol. 1, Springer - Verlag, 2009, pp. 211-241.

S

[75] Schlichting H., Gersten K.: *Boundary Layer Theory,* 2007, ISBN 978-128-121-0.

[76] Schramm G., *A Practical Approach to Rheology and Rheometry,* Gebrueder HAAKE Gmbh, Karlsruhe,1998

[77] Šesták J., Rieger F., *Přenos hybnosti, tepla a hmoty* , Vydavatelství ČVUT, 1998

T

[78] Thurston G. B., *Viscoelasticity of human blood*, Biophysical Journal 12 (1972) 1205-1217.

[79] Thurston G. B., *Non-Newtonian viscosity of human blood: Flow induced changes in microstructure*, Biorheology 31(2) (1994) 179-192.

V

[80] Verdier C., *Rheological properties of living materials. from cells to tissues*, Journal of Theoretical Medicine 5 (2) (2003) 67-91.

[81] Versteeg H. K. , W. Malalasekera *An Introduction to Computational Fluid Dynamics - The Finite Volume Method*, Longman Scientific & Technical, Harlow 1995

[82] Vierendeels J. , K. Riemslagh, E. Dick *A multigrid semi-implicit line method for viscous incompressible and low-mach-number flows on high aspect ratio grids*, Journal of Computational Physics 154 (1999) 310-344.

[83] Vlastos G. , D. Lerche, B. Koch, *The superposition of steady on oscillatory shear and its effect on the viscoelasticity of human blood and a blood-like model fluid*, Biorheology 34 (1997) 19-36.

W

[84] Walburn F. J., D. J. Schneck, *A constitutive equation for whole human blood*, Biorheology 13 (1976) 201-210.

[85] Wang N., Fogelson A. L., *Computational methods for continuum models of platelet aggregation*, J. Comput. Phys. 151 (1999)

Y

[86] Yeleswarapu K. K., M. V. Kameneva, K. R. Rajagopal, J. F. Antaki *The flow of blood in tubes: Theory and experiment*, Mech. Res. Comm. 25 (1998) 257-262.

[87] Yeleswarapu Krishna Kumar , *Evaluation of Continuum Models for Characterizing the Constitutive Behavior of Blood* , University of Pittsburgh, 1996.

Z

[88] Zarnitsina V. I., Pokhilko A. V., Ataullakhanov F. I., *A mathematical model for the spatio-temporal dynamics of intrinsic pathway of blood coagulation - I. The models description*, Thromb. Res. 84(4) 1996

[89] Zarnitsina V. I., Pokhilko A. V., Ataullakhanov F. I., *A mathematical model for the spatio-temporal dynamics of intrinsic pathway of blood coagulation - II. Results*, Thromb. Res. 84(5) 1996

Author's work

[90] Pirkl, L. - Bodnár, T. - Tůma, K. *Viscoelastic Fluid Flows at Moderate Weissenberg Numbers Using Oldroyd Type Model* In: 9th International Conference of Numerical Analysis and Applied Mathematics (ICNAAM 2011), Halkidiki, Greece

[91] Pirkl, L. - Bodnár, T. *On the Numerical Simulation of Blood Coagulation in Flowing Blood* In: Topical Problems of Fluid Mechanics 2011. Prague: Institute of Thermomechanics, AS CR, v.v.i., 2011, p. 89-92. ISBN 978-80-87012-32-1.

[92] Pirkl, L. - Bodnár, T. *Numerical Simulation of Blood Flow Using Generalized Oldroyd - B Model* In: Proceedings of the Fifth Conference on Computation Fluid Dynamics ECCOMAS CFD 2010 [CD-ROM]. Lisbon: Instituto Superior Técnico, Technical University of Lisbon, National Civil Engineering Laboratory, 2010, ISBN 978-989-96778-1-4.

[93] Pirkl, L. - Bodnár, T. *The Blood Flow Simulations Using Shear - Thinning Oldroyd - B Models* In: Topical Problems of Fluid Mechanics 2010 Proceedings. Prague: Institute of Thermomechanics, AS CR, v.v.i., 2010, p. 115-118. ISBN 978-80-87012-25-3.

[94] Pirkl, L. *Development and Validation of a Stabilized Finite Element Solver for Variable Density Flows* In: Von Karman Institute For Fluid Dynamics, B-1640 Rhode-St-Genese, Belgium

[95] Bodnár, T. - Sequeira, A. - Pirkl, L. *Numerical Simulations of Blood Flow in a Stenosed Vessel under Different Flow Rates using a Generalized Oldroyd - B Model* In: Numerical Analysis and Applied Mathematics, Vols 1 and 2. Melville, New York: American Institute of Physics, 2009, vol. 2, p. 645-648. ISBN 978-0-7354-0709-1.

[96] Pirkl, L. - Bodnár, T. *The Blood Flow Simulations Using Generalized Newtonian Models* In: Colloquium Fluid Dynamics 2009 Proceedings [CD-ROM]. Prague: Institute of Thermomechanics, AS CR, v.v.i., 2009, ISBN 978-80-87012-21-5.

[97] Pirkl, L. - Bodnár, T. *Numerical Simulation of Newtonian and Generalized Newtonian Flows of Human Blood* In: Topical Problems of Fluid Mechanics 2008. Praha: Ústav termomechaniky AV ČR, 2008, p. 81-84. ISBN 978-80-87012-09-3.

[98] Pirkl L., *Numerical Simulation of Incompressible Flows with Variable Viscosity, Diploma Thesis, Czech Technical University of Prague*, Faculty of Mechanical Engineering, Department of Technical Mathematics , Prague, 2007.

[99] Pirkl, L. - Bodnár, T. *Numerical Simulation of Turbulent Flows around Sinusoidal Hills* In: Colloquium Fluid Dynamics 2007 [CD-ROM]. Praha: Ústav termomechaniky AV ČR, 2007, ISBN 978-80-87012-07-9.

[100] Bodnár, T. - Pirkl, L. *Numerical Simulation of Non - Newtonian Fluid Flow Using Generalized Navier - Stokes Models* In: Colloquium Fluid Dynamics 2006 Proceedings. Praha: Ústav termo-mechaniky AV ČR, 2006, p. 95-98. ISBN 80-87012-01-1.

Internet pages

[101] http://en.wikipedia.org/ , internet pages.

[102] http://www.cfd-online.com/ , internet pages.

[103] http://www.ercoftac.org/ , European Research Community On Flow, Turbulence And Combustion, internet pages.

[104] http://www.britannica.com/ , Encyclopedia Britannica, Inc., internet pages.

[105] http://www.openfoam.com/docs/ , On-line documentation, internet pages.

[106] http://en.wikipedia.org/wiki/Coagulation , internet pages.

[107] http://www.daviddarling.info/encyclopedia/B/blood_clotting.html, internet pages.

[108] http://www.healthjockey.com/2007/11/24/blood-clot-doubles-the-risk-of-stroke, internet pages.

Appendix A

Finite element method

We show how the Finite element method works on a steady incompressible Navier-Stokes equations in two dimensions. Finite element method is based on the weak formulation of the problem. We will use a less standard definition of a weak solution, which is similar to the Galerkin system used for the Finite element method.

Definition 1. *Let $\Omega \subset \mathbb{R}^2$ is a bounded domain with Lipschitz boundary $\partial\Omega$ consisting of two parts Γ_D and Γ_N such that $\partial\Omega = \Gamma_D \cup \Gamma_N$. We say that $(\vec{v}, p)$ is the weak solution of the incompressible Navier-Stokes equations if*

$$p \in L^2(\Omega),$$
$$\vec{v} - \vec{\tilde{v}} \in V := \left\{ \vec{w} \in (W^{1,2}(\Omega))^2, \vec{w}|_{\Gamma_D} = 0 \right\} \text{ and } \vec{\tilde{v}} = \vec{v_D} \text{ on } \Gamma_D$$

satisfying

$$\int_{\Omega} (\operatorname{div} \vec{v}) \psi \, \mathrm{d}x = 0, \quad \forall \psi \in L^2(\Omega),$$
$$\int_{\Omega} \rho(\vec{v} \cdot \nabla \vec{v}) \cdot \vec{\varphi} \, \mathrm{d}x = -\int_{\Omega} \mathbf{T} \cdot \nabla \vec{\varphi} \, \mathrm{d}x + \int_{\Gamma_N} \mathbf{T}\vec{n} \cdot \vec{\varphi} \, \mathrm{d}S, \quad \forall \vec{\varphi} \in V,$$

where $\mathbf{T}$ is the Newtonian stress tensor

$$\mathbf{T} = -p\mathbf{I} + \eta \left(\nabla \vec{v} + (\nabla \vec{v})^{\mathrm{T}} \right).$$

Then the Galerkin system for the Finite element method is in the same form. The problem is to find $(\vec{v}_h, p_h)$ such that

$$p_h \in P_h,$$
$$\vec{v}_h - \vec{\tilde{v}}_h \in V_h, \text{ where } \vec{\tilde{v}}_h = \vec{v_D} \text{ on } \Gamma_D$$

satisfying

$$\int_{\Omega_h} (\operatorname{div} \vec{v}_h) \psi_h \, \mathrm{d}x = 0, \quad \forall \psi_h \in P_h,$$
$$\int_{\Omega_h} \rho(\vec{v}_h \cdot \nabla \vec{v}_h) \cdot \vec{\varphi}_h \, \mathrm{d}x = -\int_{\Omega_h} \mathbf{T}_h \cdot \nabla \vec{\varphi}_h \, \mathrm{d}x + \int_{\Gamma_N} \mathbf{T}_h \vec{n} \cdot \vec{\varphi}_h \, \mathrm{d}S, \quad \forall \vec{\varphi}_h \in V_h,$$

where

$$\mathbf{T}_h = -p_h \mathbf{I} + \eta \left(\nabla \vec{v}_h + (\nabla \vec{v}_h)^{\mathrm{T}} \right)$$

and the finite dimensional spaces are following

$$P_h = \left\{ q_h \in L^2(\Omega_h), q_h|_T \in P_1^{\mathrm{disc}}(T) \; \forall T \in \mathcal{T}_h \right\},$$
$$V_h = \left\{ \vec{w}_h \in (C(\Omega_h))^2, \vec{w}_h|_T \in Q_2(T) \; \forall T \in \mathcal{T}_h \right\}.$$

The domain Ω_h has a polygonal boundary and it is an approximation of the domain Ω. By $\mathcal{T}_h$ we denote a set of quadrilateral elements T covering the domain Ω_h. We assume that $\mathcal{T}_h$ is regular which means that any two quadrilaterals are disjoint or have one common edge or a common vertex.

This combination of Q_2 (standard continuous biquadratic with nine degrees of freedom per quadrilateral) for the velocity and P_1^{disc} (discontinuous linear with three degrees of freedom per quadrilateral) for the pressure is a stable pair for the incompressible problem.

Now, let us denote $\{\vec{w}_i\}_{i=1}^l$ a usual Finite element basis of the finite dimensional space V_h and $\{q_i\}_{i=1}^m$ a basis of the finite dimensional space P_h. Then we can express the approximate solution in the form

$$\vec{v}_h = \vec{\tilde{v}}_h + \sum_{i=1}^l V_i \vec{w}_i,$$

$$p_h = \sum_{i=1}^m P_i q_i,$$

where l is equal to the number of all vertices + number of all edges + number of all quadrilaterals, m is equal to three times number of all quadrilaterals. We use the following test functions in the Galerkin system

$$\vec{\varphi}_h = \vec{w}_i, i = 1, \ldots, l,$$

$$\psi_h = q_i, i = 1, \ldots, m,$$

after substitution we get[1]

$$\varrho \underbrace{\int_{\Omega_h} \sum_{i,k=1}^l \left((\vec{\tilde{v}}_h + V_i \vec{w}_i) \cdot (\nabla \vec{\tilde{v}}_h + V_k \nabla \vec{w}_k) \right) \nabla \vec{w}_j}_{N(\vec{V})_j} + \underbrace{\eta \int_{\Omega_h} \nabla \vec{\tilde{v}}_h \cdot \nabla \vec{w}_j +}_{F_j}$$

$$+ \sum_{i=1}^l V_i \, \eta \underbrace{\int_{\Omega_h} \nabla \vec{w}_i \cdot \nabla \vec{w}_j}_{A_{ji}} - \sum_{i=1}^m P_i \underbrace{\int_{\Omega_h} q_i \, \text{div} \, \vec{w}_j}_{-B_{ji}} = 0, \quad j = 1, \ldots, l$$

$$\sum_{i=1}^l V_i \underbrace{\int_{\Omega_h} (\text{div} \, \vec{w}_i) \vec{w}_j \, \mathrm{d}x}_{-B_{ij}} + \underbrace{\int_{\Omega_h} (\text{div} \, \vec{\tilde{v}}_h) \vec{w}_j}_{G_j} = 0, \quad j = 1, \ldots, m$$

which can be rewritten into the set of $(l + m)$ nonlinear algebraic equations

$$\Phi \begin{pmatrix} \vec{V} \\ \vec{P} \end{pmatrix} := \begin{pmatrix} \mathbf{A}\vec{V} + \vec{N}(\vec{V}) + \mathbf{B}\vec{P} + \vec{F} \\ -\mathbf{B}^{\mathrm{T}}\vec{V} + \vec{G} \end{pmatrix} = \vec{0}.$$

We solve it by the Newton method

$$\mathbf{J}\vec{\delta} = \vec{R},$$

where the Jacobian $\mathbf{J}$ is computed by finite differences

$$\mathbf{J} = \frac{D\Phi \begin{pmatrix} \vec{V}^k \\ \vec{P}^k \end{pmatrix}}{D \begin{pmatrix} \vec{V} \\ \vec{P} \end{pmatrix}}$$

and

$$\vec{\delta} = \begin{pmatrix} \vec{V}^{k+1} \\ \vec{P}^{k+1} \end{pmatrix} - \begin{pmatrix} \vec{V}^k \\ \vec{P}^k \end{pmatrix}, \quad \vec{R} = -\Phi \begin{pmatrix} \vec{V}^k \\ \vec{P}^k \end{pmatrix}.$$

---

[1]The boundary term is now missing because we prescribe $\mathbf{T}\vec{n} = \vec{0}$ on Γ_N.

We iterate in the Newton method in this sense

$$\begin{pmatrix} \vec{V}^{k+1} \\ \vec{P}^{k+1} \end{pmatrix} = \begin{pmatrix} \vec{V}^{k} \\ \vec{P}^{k} \end{pmatrix} + \omega\vec{\delta}, \quad \omega \in (0, 1],$$

where ω is adaptively chosen to improve the convergence. Stopping criterion is the L^2 norm and energetic norm of the residuum. The set of linear algebraic equations (13.1) for the unknown $\vec{\delta}$ is computed by the direct solver UMFPACK (see [31]).

The implementation is based on the code developed in [42].

Appendix B

Blood Coagulation Model Constants

Constant name	Symbol	SI Unit	Value
h11L1	h11L1	[0 0 -1 0 -1 0 0]	216.6667;
h11A3	h11A3	[0 0 -1 0 -1 0 0]	26666.6667;
h9	h9	[0 0 -1 0 -1 0 0]	270000;
h10	h10	[0 0 -1 0 -1 0 0]	5783333.33;
hTFPI	hTFPI	[0 0 -1 0 -1 0 0]	8000000;
h2	h2	[0 0 -1 0 -1 0 0]	11900000;
hPC	hPC	[0 0 -1 0 -1 0 0]	11;
hPLA	hPLA	[0 0 -1 0 -1 0 0]	1600000;
hPCI12a	hPCI12a	[0 0 -1 0 -1 0 0]	3666.6667;
halphaAP	halphaAP	[0 0 -1 0 -1 0 0]	183.3333;
h12A3	h12A3	[0 0 -1 0 -1 0 0]	0.0216667;
hPCI11a	hPCI11a	[0 0 -1 0 -1 0 0]	2300;
h8	h8	[0 0 -1 0 0 0 0]	0.0037;
hC8	hC8	[0 0 -1 0 0 0 0]	0.17;
h5	h5	[0 0 -1 0 0 0 0]	0.002833333;
hC5	hC5	[0 0 -1 0 0 0 0]	0.17;
h1	h1	[0 0 -1 0 0 0 0]	25;
h12	h12	[0 0 -1 0 0 0 0]	0.014166667;
hkalli	hkalli	[0 0 -1 0 0 0 0]	0.01133333;
H1M	H1M	[0 0 0 0 1 0 0]	250000e-9;
HC8M	HC8M	[0 0 0 0 1 0 0]	14.6e-9;
HC5M	HC5M	[0 0 0 0 1 0 0]	14.6e-9;

Table 13.1: Summary of constituents, model parameters, part 2

Constituent name	Symbol	Diffusion coefficients d_i	Initial value [M]
Fibrinogen	I	3.10e-11	7.00e-6
Fibrin	Ia	2.47e-11	7.00e-9
Prothrombin	II	5.21e-11	1.40e-6
Thrombin	IIa	6.47e-11	1.40e-9
Factor V	V	3.12e-11	2.00e-8
Factor Va	Va	3.82e-11	2.0e-11
Factor VIII	VIII	3.12e-11	0.70e-9
Factor VIIIa	VIIIa	3.92e-11	0.7e-12
Factor IX	IX	5.63e-11	9.00e-8
Factor IXa	IXa	6.25e-11	9.0e-11
Factor X	X	5.63e-11	1.70e-7
Factor Xa	Xa	7.37e-11	1.7e-10
Factor XI	XI	3.97e-11	3.00e-8
Factor XIa	XIa	5.00e-11	3.0e-11
Factor XII	XII	5.00e-11	5.00e-7
Factor XIIa	XIIa	2.93e-11	5.00e-9
Prekallikrein	PreK	4.92e-11	4.85e-7
Kallikrein	Kalli	4.92e-11	4.85e-9
Tissue Pathway Inhibitor	TFPI	6.30e-11	2.50e-9
Protein C	PC	5.44e-11	6.00e-8
Activated Protein C	APC	5.50e-11	6.0e-11
α_1 Antitrypsin	α_1AT	5.82e-11	4.50e-5
α_2 Antiplasmin	α_2AP	5.25e-11	1.05e-7
Plasminogen	PLA	4.93e-11	2.18e-9
Plasmin	PLS	4.81e-11	2.18e-6
Protein C1 Inhibitor	C1-INH	4.61e-11	2.41e-6
Antithrombin III	ATIII	5.57e-11	2.41e-6
tissue pathway Activator	tPA	5.28e-11	0.08e-9

Table 13.2: Summary of constituents, diffusion terms, initial values

Constituent name	Symbol	Chemical reaction source terms s_i
Fibrinogen	I	$\frac{k_1 \cdot IIa \cdot I}{K_{1M}+I}$
Fibrin	Ia	$\frac{k_1 \cdot IIa \cdot I}{K_{1M}+I} - \frac{h_1 \cdot PLA \cdot Ia}{H_{1M}+Ia}$
Prothrombin	II	$\frac{-k_2 \cdot Va \cdot Xa \cdot II}{K_{dW} \cdot (K_{2M}+II)}$
Thrombin	IIa	$\frac{k_2 \cdot Va \cdot Xa \cdot II}{K_{dW} \cdot (K_{2M}+II)} - h_2 \cdot IIa \cdot ATIII$
Factor V	V	$\frac{-k_5 \cdot IIa \cdot V}{K_{5M}+V} - \frac{h_{C5} \cdot APC \cdot Va}{H_{C5M}+Va}$
Factor Va	Va	$\frac{k_5 \cdot IIa \cdot V}{K_{5M}+V} - \frac{h_{C5} \cdot APC \cdot Va}{H_{C5M}+Va} - h_5 \cdot Va$
Factor VIII	VIII	$\frac{-k_8 \cdot IIa \cdot VIII}{K_{8M}+VIII}$
Factor VIIIa	VIIIa	$\frac{k_8 \cdot IIa \cdot VIII}{K_{8M}+VIII} - \frac{h_{C8} \cdot APC \cdot VIIIa}{H_{C8M}+VIIIa} - h_8 \cdot VIIIa$
Factor IX	IX	$\frac{-k_9 \cdot XIa \cdot IX}{K_{9M}+IX}$
Factor IXa	IXa	$\frac{k_9 \cdot XIa \cdot IX}{K_{9M}+IX} - h_9 \cdot IXa \cdot ATIII$
Factor X	X	$\frac{-k_{10} \cdot VIIIa \cdot IXa \cdot X}{K_{dZ} \cdot (K_{10M}+IX)}$
Factor Xa	Xa	$\frac{k_{10} \cdot VIIIa \cdot IXa \cdot X}{K_{dZ} \cdot (K_{10M}+IX)} - h_{10} \cdot Xa \cdot ATIII - h_{TFPI} \cdot TFPI \cdot Xa$
Factor XI	XI	$\frac{-k_{11} \cdot IIa \cdot XI}{K_{11M}+XI} + \frac{-k_{12a} \cdot XIIa \cdot XI}{K_{12aM}+XI}$
Factor XIa	XIa	$\frac{k_{11} \cdot IIa \cdot XI}{K_{11M}+XI} + \frac{k_{12a} \cdot XIIa \cdot XI}{K_{12aM}+XI} + \left(\begin{matrix} -h_{11A3} \cdot XIa \cdot ATIII - h_{11L1} \cdot XIa \cdot \alpha 1AT \\ -h_{C1Inh-11a} \cdot XIa \cdot C1INH \end{matrix} \right)$
Factor XII	XII	$\frac{-k_{12} \cdot XIIa \cdot XI}{K_{12M}+XII} + \frac{-k_{kalli} \cdot Kalli \cdot XII}{K_{kalliM}+XII}$
Factor XIIa	XIIa	$\frac{k_{12} \cdot XII}{K_{12M}+XII} + \frac{k_{kalli} \cdot Kalli \cdot XII}{K_{kalli}+XII} + \left(\begin{matrix} -h_{12} \cdot XIIa - h_{C1Inh-12a} \cdot XIIa \cdot C1INH \\ -h_{\alpha AP} \cdot XIIa \cdot \alpha 2AP - h_{AT3} \cdot XIIa \cdot ATIII \end{matrix} \right)$
Prekallikrein	PreK	$\frac{-k_{PreKA} \cdot XIIa \cdot PreK}{K_{PreKAM}+PreK} + \frac{-k_{PreKB} \cdot XIIa \cdot PreK}{K_{PreKBM}+PreK} - h_{kalli} \cdot Kalli$
Kallikrein	Kalli	$\frac{k_{PreKA} \cdot XIIa \cdot PreK}{K_{PreKAM}+PreK} + \frac{k_{PreKB} \cdot XIIa \cdot PreK}{K_{PreKBM}+PreK}$
Tissue Pathway Inhibitor	TFPI	$-h_{TFPI} \cdot TFPI \cdot Xa$
Protein C	PC	$\frac{k_{PC} \cdot IIa \cdot PC}{K_{PCM}+PC}$
Activated Protein C	APC	$\frac{k_{PC} \cdot IIa \cdot PC}{K_{PCM}+PC} - h_{PC} \cdot APC \cdot \alpha_1 AT$
α_1 Antitrypsin	$\alpha_1 AT$	$-h_{PC} \cdot APC \cdot \alpha 1AT - h_{11L1} \cdot XIa \cdot \alpha_1 AT$
α_2 Antiplasmin	$\alpha_2 AP$	$-(h_{PLA} \cdot PLA + h_{\alpha_2 AP} \cdot XIIa) \cdot \alpha_2 AP$
Plasminogen	PLA	$\frac{k_{PLA} \cdot tPA \cdot PLS}{K_{PLAM}+PLS} + \frac{k_{PLA-12a} \cdot XIIa \cdot PLS}{K_{PLA-12aM}+PLS} - h_{PLA} \cdot PLA \cdot \alpha_2 AP$
Plasmin	PLS	$\frac{-k_{PLA} \cdot tPA \cdot PLS}{K_{PLAM}+PLS} + \frac{-k_{PLA-12a} \cdot XIIa \cdot PLS}{K_{PLA-12aM}+PLS}$
Protein C1 Inhibitor	C1-INH	$-(h_{PCI-12a} \cdot XIIa + h_{PCI-11a} \cdot XIa) \cdot C1-INH$
Antithrombin III	ATIII	$-(h_9 \cdot IXa + h_{10} \cdot Xa + h_2 \cdot IIa + h_{11A3} \cdot XIa + h_{AT3} \cdot XIIa) \cdot ATIII$
tissue pathway Activator	tPA	0

Table 13.3: Summary of constituents, reaction terms

Constant name	Symbol	SI Unit	Value
k12a	k12a	[0 0 -1 0 0 0 0]	0.000566667;
k11	k11	[0 0 -1 0 0 0 0]	0.00013;
k8	k8	[0 0 -1 0 0 0 0]	3.24;
k9	k9	[0 0 -1 0 0 0 0]	0.1883;
k5	k5	[0 0 -1 0 0 0 0]	0.45;
k10	k10	[0 0 -1 0 0 0 0]	39.85;
k2	k2	[0 0 -1 0 0 0 0]	22.4;
k1	k1	[0 0 -1 0 0 0 0]	59;
kPLA	kPLA	[0 0 -1 0 0 0 0]	0.2;
k12	k12	[0 0 -1 0 0 0 0]	0.033;
kPreKA	kPreKA	[0 0 -1 0 0 0 0]	3.6;
kPreKB	kPreKB	[0 0 -1 0 0 0 0]	40.0;
kPC	kPC	[0 0 -1 0 0 0 0]	0.65;
kkalli	kkalli	[0 0 -1 0 0 0 0]	7.25;
kPLA12a	kPLA12a	[0 0 -1 0 0 0 0]	0.0013;
K12aM	K12aM	[0 0 0 0 1 0 0]	2000e-9;
K11M	K11M	[0 0 0 0 1 0 0]	50e-9;
K9M	K9M	[0 0 0 0 1 0 0]	160e-9;
K8M	K8M	[0 0 0 0 1 0 0]	112000e-9;
K5M	K5M	[0 0 0 0 1 0 0]	140.5e-9;
KdZ	KdZ	[0 0 0 0 1 0 0]	0.56e-9;
K10M	K10M	[0 0 0 0 1 0 0]	160e-9;
KdW	KdW	[0 0 0 0 1 0 0]	0.1e-9;
K2M	K2M	[0 0 0 0 1 0 0]	1060e-9;
KPLAM	KPLAM	[0 0 0 0 1 0 0]	18e-9;
K1M	K1M	[0 0 0 0 1 0 0]	3160e-9;
KPLA12aM	KPLA12aM	[0 0 0 0 1 0 0]	270e-9;
K12M	K12M	[0 0 0 0 1 0 0]	7500e-9;
KkalliM	KkalliM	[0 0 0 0 1 0 0]	780e-9;
KPreKAM	KPreKAM	[0 0 0 0 1 0 0]	91e-9;
KPreKBM	KPreKBM	[0 0 0 0 1 0 0]	36000e-9;
KPCM	KPCM	[0 0 0 0 1 0 0]	3190e-9;
k79	k79	[0 0 -1 0 0 0 0]	0.54;
k710	k710	[0 0 -1 0 0 0 0]	1.716666667;
K79M	K79M	[0 0 0 0 1 0 0]	24.0e-9;
K710M	K710M	[0 0 0 0 1 0 0]	240.0e-9;
kCtPA	kCtPA	[0 2 -1 0 1 0 0]	1.087e-5;
kIIatPA	kIIatPA	[0 2 -1 0 0 0 0]	1.545e-13;
kIatPA	kIatPA	[0 2 -1 0 0 0 0]	8.4317e-20;
kTF7a	kTF7a	[0 0 0 0 0 0 0]	1.0e4;

Table 13.4: Summary of constituents, model parameters